

¹ Study of the multi-strange resonance $\Xi(1530)^0$ production
² with ALICE at the LHC energies

³ Jihye Song

4 Contents

5	List of Figures	4
6	List of Tables	8
7	1 The physics of relativistic heavy-ion collisions	9
8	1.1 Standard model	9
9	1.2 QCD and Quark-Gluon plasma	10
10	1.3 Heavy Ion Collisions	15
11	2 Theoretical models	17
12	2.1 Thermal statistical model	17
13	2.1.1 Calculations	18
14	2.1.2 Results	18
15	2.1.3 Comparison with data	20
16	2.2 UrQMD	20
17	3 Production of resonance with strangeness	20
18	3.1 Strange quark and hyperons	23
19	3.2 Resonance production	25
20	4 A Large Ion Collider Experiment at the LHC	27
21	4.1 The Large Hadron Collider	27
22	4.2 The ALICE project	30
23	4.2.1 ALICE detector	30
24	4.2.2 Data Acquisition (DAQ) and trigger system	40
25	4.2.3 ALICE offline software frame work	42
26	5 Measurement of $\Xi(1530)^0$ production in p-Pb and Pb-Pb	44
27	5.1 $\Xi(1530)^0$ -reconstruction	44
28	5.1.1 Data sample and event selection	44
29	5.1.2 Track and topological selection	48
30	5.1.3 Particle identification	51
31	5.1.4 Signal extraction	54
32	5.2 Efficiency correction	63
33	5.3 Corrected p_T -spectra	66
34	5.4 Systematic uncertainties	68
35	5.5 $\Xi(1530)^0$ transverse momentum spectra	73

36	6 Further results and discussion	76
37	6.1 Mean transverse momentum	76
38	6.2 Particle yield ratios	80
39	6.2.1 Integrated yield ratios of excited to ground-state hadrons	80
40	6.3 Integrated yield ratios to pion	83
41	References	87

⁴² **List of Figures**

43	1	Standard Model families of leptons and quarks as the gauge bosons	9
44	2	Summary of measurements of η s as a function of the respective energy scale Q. The respective degree of QCD perturbation theory used in the extraction of η s is indicated in brackets (NLO: next-to-leading order; NNLO: next-to-next-to leading order; res. NNLO: NNLO matched with resummed next-to-leading logs; N3LO: next-to-NNLO) [1]	13
45	3	Hydrodynamic evolution of a heavy ion collision with and without the formation of a QGP.	16
46	4	Ratio of baryonic and mesonic resonances over their stable partner as a function of temperature.	19
47	5	Ratio of resonances over their stable partner as a function of $\sqrt(s)$	21
48	6	The $J^P = 1/2^+$ ground state baryon octet	22
49	7	The $J^P = 3/2^+$ baryon decuplet	22
50	8	Enhancements in the rapidity range $ y < 0.5$ as a function of the mean number of participants $\langle N_{part} \rangle$, showing LHC (ALICE, full symbols), RHIC and SPS (open symbols) data. Boxes on the dashed line at unity indicate statistical and systematic uncertainties on the pp or p-Be reference. Error bars on the data points represent the corresponding uncertainties for all the heavy-ion measurements and those for p-Pb at the SPS.	24
51	9	Hadronic phase	25
52	10	The CERN accelerator complex [2]	28
53	11	The ALICE detector	32
54	12	Schematic view of the ITS [3]	33
55	13	Track impact parameter resolution in the transverse plane ($r\phi$) vs p_T for charged particle	34
56	14	Schematic view of the TPC	35
57	15	Specific energy loss (dE/dx) in the TPC vs. particle momentum in Pb-Pb collisions at $\sqrt{s_{NN}} = 2.76$ TeV. The lines show the parametrisations of the expected mean energy loss.	36
58	16	Correlation between the sum and difference of signal times in V0A and V0C. Three classes of events collisions at (8.3 ns, 14.3 ns), background from Beam 1 at (-14.3 ns, -8.3 ns), and background from Beam 2 at (14.3 ns, 8.3 ns) can be clearly distinguished.	38
59	17	Distribution of the V0 amplitude (sum of V0A and V0C in top, V0A in bottom). The inset shows a magnified version of the most peripheral region.	39
60	18	The overall architecture of the ALICE DAQ and the interface to the HLT system.	40
61	19	Schematic view of the AliRoot framework	43

81	20	Vertex-z coordinate distribution of the accepted events in p–Pb collision(Left) and in Pb–Pb collisions(Right). The red dashed line indicates vertex cut	46
82	21	Multiplicity distribution of accepted events in p–Pb collision in percentile. The each color and labels define the four intervals in which the analysis is performed.	46
83	22	Centrality distribution of three different trigger classes.	47
84	23	Sketch of the decay modes for Ξ^{*0} and depiction of the track and topological selection criteria.	49
85	24	TPC dE/dx as function of transverse momentum for total (top) and selected first emitted π in 3σ (bottom)	51
86	25	TPC dE/dx as function of transverse momentum for total (top) and selected second emitted π in 3σ (bottom)	51
87	26	TPC dE/dx as function of transverse momentum for total (top) and selected last emitted π in 3σ (bottom)	52
88	27	TPC dE/dx as function of transverse momentum for total (top) and selected proton in 3σ (bottom)	52
89	28	TPC dE/dx as function of transverse momentum for total (top) and selected first emitted π in 3σ (bottom)	52
90	29	TPC dE/dx as function of transverse momentum for total (top) and selected second emitted π in 3σ (bottom)	53
91	30	TPC dE/dx as function of transverse momentum for total (top) and selected last emitted π in 3σ (bottom)	53
92	31	TPC dE/dx as function of transverse momentum for total (top) and selected proton in 3σ (bottom)	54
93	32	The $\Xi^{\mp}\pi^{\pm}$ invariant mass distribution (Same-event pairs) in $1.8 < p_T < 2.2 \text{ GeV}/c$ and for the multiplicity class 20-40%. The background shape, using pairs from different events (Mixed-event background), is normalised to the counts in $1.49 < M_{\Xi\pi} < 1.51 \text{ GeV}/c^2$ and $1.56 < M_{\Xi\pi} < 1.58 \text{ GeV}/c^2$	55
94	33	The $\Xi^{\mp}\pi^{\pm}$ invariant mass distribution (Same-event pairs) in $3.0 < p_T < 3.5 \text{ GeV}/c$ and for the centrality class 0-10%. The background shape, using pairs from different events (Mixed-event background), is normalised to the counts in $1.49 < M_{\Xi\pi} < 1.51 \text{ GeV}/c^2$ and $1.56 < M_{\Xi\pi} < 1.58 \text{ GeV}/c^2$	56
95	34	The invariant mass distribution after subtraction of the mixed-event background in p–Pb collisions. The solid curve represents the combined fit, while the dashed line describes the residual background.	57
96	35	The invariant mass distribution after subtraction of the mixed-event background in Pb–Pb collisions. The solid curve represents the combined fit, while the dashed line describes the residual background.	58
97	36	σ fit parameters as a function of p_T in MB in p–Pb collisions (top) and in Pb–Pb collisions (bottom).	60

121	37	$\Xi(1530)^0$ -mass obtained from fit of the Voigtian peak as a function of p_{T} in each multiplicity classes in p–Pb collisions (top) and the different centrality classes in Pb–Pb (bottom).	61
122			
123	38	$\Xi(1530)^0$ -raw spectra obtained from fit of the Voigtian peak and a polynomial residual background for different multiplicities in p–Pb collisions (top) and Pb–Pb collisions (bottom). Only the statistical error is reported.	62
124			
125	39	$\Xi(1530)^0$ -raw spectra obtained from fit of the Voigtian peak and a polynomial residual background for different multiplicities. Only the statistical error is reported.	63
126			
127	40	Real corrected $\Xi(1530)^0$ spectrum (black) for the minimum bias with Levy fit (black curve). Also shown are the unweighted generated (blue) and reconstructed (red) $\Xi(1530)^0$ spectra.	64
128			
129	41	Efficiency as a function of p_{T} in minimum bias events in p–Pb collisions.	65
130			
131	42	Efficiency as a function of p_{T} in different centrality classes in Pb–Pb collisions	66
132			
133	43	Corrected p_{T} -spectra of $\Xi(1530)^0$ in NSD and different multiplicity classes in p–Pb collisions.	67
134			
135	44	Corrected p_{T} -spectra of $\Xi(1530)^0$ in different centrality classes in Pb–Pb collisions.	67
136			
137	45	Summary of the contributions to the systematic uncertainty in minimum bias events in p–Pb collisions. The dashed black line is the sum in quadrature of all the contributions.	71
138			
139	46	Systematic uncertainties for each multiplicity classes in p–Pb collisions.	71
140			
141	47	Summary of the contributions to the systematic uncertainty in minimum bias events in Pb–Pb collisions. The dashed black line is the sum in quadrature of all the contributions.	72
142			
143	48	Systematic uncertainties for each multiplicity classes.	72
144			
145	49	Corrected yields as function of p_{T} in NSD events and multiplicity dependent event classes in p–Pb collision system. Statistical uncertainties are presented as bar and systematical uncertainties are plotted as boxes.	74
146			
147	50	Corrected yields as function of p_{T} in different centrality classes in Pb–Pb collision system. Statistical uncertainties are presented as bar and systematical uncertainties are plotted as boxes.	75
148			
149	51	Mean transverse momenta $\langle p_{\text{T}} \rangle$ of Λ , Ξ^- , $\Sigma^{*\pm}$, Ξ^{*0} and Ω^- in p–Pb collisions at $\sqrt{s_{\text{NN}}} = 5.02$ TeV as a function of mean charged-particle multiplicity density $\langle dN_{\text{ch}}/d\eta_{\text{lab}} \rangle$, measured in the pseudorapidity range $ \eta_{\text{lab}} < 0.5$. The results for Λ , Ξ^- and Ω^- are taken from [4, 5, 6]. Statistical and systematic uncertainties are represented as bars and boxes, respectively. The Ω^- and Ξ^- points in the 3rd and 4th lowest multiplicity bins are slightly displaced along the abscissa to avoid superposition with the $\Xi(1530)^0$ points.	77
150			
151			
152			
153			
154			
155			
156			
157			
158			
159			

160	52	Mass dependence of the mean transverse momenta of identified particles for the 0 – 20% V0A multiplicity class and with $-0.5 < y_{\text{CMS}} < 0$ in p– Pb collisions at $\sqrt{s_{\text{NN}}} = 5.02$ TeV [4, 6], and in minimum-bias pp collisions at $\sqrt{s} = 7$ TeV [7] with $ y_{\text{CMS}} < 0.5$. Additionally, D^0 and J/ψ results are plotted. The D^0 and J/ψ were measured in different rapidity ranges: $ y_{\text{CMS}} < 0.5$ [8] ($ y_{\text{CMS}} < 0.9$ [9]) for D^0 (J/ψ) in pp and $-0.96 < y_{\text{CMS}} <$ 0.04 [8] ($-1.37 < y_{\text{CMS}} < 0.43$ [10]) for D^0 (J/ψ) in p–Pb. Note also that the results for D^0 and J/ψ in p–Pb collisions are for the 0–100% multiplicity class.	78
161			
162	53	Ratio of $\Xi(1530)^0$ to Ξ^- measured in pp [7], p–Pb [4, 6] and Pb–Pb collisions as a function of $\langle dN_{\text{ch}}/d\eta_{\text{lab}} \rangle$ measured at midrapidity. Statistical uncer- tainties (bars) are shown as well as total systematic uncertainties (hollow boxes) and systematic uncertainties uncorrelated across multiplicity (shaded boxes). A few model predictions are also shown as lines at their appropriate abscissa.	81
163			
164	54	Ratio of $\rho/\pi(\text{Up})$, K^*/K , $\phi/K(\text{Left bottom})$ and Λ^*/Λ with system size measured at mid-rapidity. Statistical uncertainties (bars) are shown as well as total systematic uncertainties (hollow boxes) and systematic uncertainties uncorrelated across multiplicity (shaded boxes). A few model predictions are also shown as lines at their appropriate abscissa.	82
165			
166	55	Ratio of $\Xi(1530)^0$ to π^\pm , measured in pp [11] and p–Pb [7] collisions, as a function of the average charged particle density ($\langle dN_{\text{ch}}/d\eta_{\text{lab}} \rangle$) measured at mid-rapidity. Statistical uncertainties (bars) are shown as well as total systematic uncertainties (hollow boxes) and systematic uncertainties uncor- related across multiplicity (shaded boxes). A few model predictions are also shown as lines at their appropriate abscissa.	84
167			
168	56	Particle yield ratios to pions of strange and multi-strange hadrons normal- ized to the values measured in pp collisions, both in pp and in p–Pb colli- sions. The common systematic uncertainties cancel in the double-ratio. The empty boxes represent the remaining uncorrelated uncertainties. The lines represent a simultaneous fit of the results with the empirical scaling formula in Equation ???.	85
169			
170	57	p_{T} -integrated yield ratios of strange and multi-strange hadrons to $(\pi^+ + \pi^-)$ as a function of $\langle dN_{\text{ch}}/d\eta_{\text{lab}} \rangle$ measured in the rapidity interval $ \eta < 0.5$. The empty and dark-shaded boxes show the total systematic uncertainty and the contribution uncorrelated across multiplicity bins, respectively. The values are compared to calculations from MC models and to results obtained in Pb–Pb and p–Pb collisions at the LHC.	86
171			
172			
173			
174			
175			
176			
177			
178			
179			
180			
181			
182			
183			
184			
185			
186			
187			
188			
189			
190			
191			
192			
193			
194			
195			
196			
197			

¹⁹⁸ **List of Tables**

199	1	Parameters used in the thermal-model calculations.	18
200	2	Properties of particles used in the ratio calculations.	20
201	3	Difference of mass (ΔM), baryon number (ΔB), strangeness (ΔS) and charge (ΔQ) of the ratios. The values of the slopes needs to be checked!!!! .	20
202	4	Quantum numbers and masses associated to the three lighter quarks: u, d and s	21
205	5	Lifetime of hadronic resonances	23
206	6	Number of accepted and analyzed events per multiplicity/centrality interval	48
207	7	Track selections common to all decay daughters and primary track selections applied to the charged pions from decays of Ξ^{*0}	48
209	8	Topological and track selection criteria.	49
210	9	Summary of the systematic uncertainties on the differential yield, $d^2N/(dp_T dy)$. Minimum and maximum values in all p_T intervals and multiplicity classes in p–Pb, centrality classes in Pb–Pb are shown for each source.	73
211			
212			

213 1 The physics of relativistic heavy-ion collisions

214 1.1 Standard model

215 . Our current understanding concerning the question what the world is made of is collected
 216 in the Standard Model of particle physics (SM) [12], that describes our universe in terms of
 217 matter and forces. In this picture matter is composed of 12 point-like particles, which have a
 218 spin of 1/2 (fermions) and can be classified according to how they interact or equivalently to
 219 what charges they carry. There are six quarks (up, down, charm, strange, top and bottom)
 220 and six leptons (electron, electron neutrino, muon, muon neutrino, tau, tau neutrino) as
 221 reported in Figure reffig:sm. The interactions between elementary particles are described
 222 by the exchange of gauge bosons (usually as virtual particles¹) or equivalently by mean of
 223 a field. Mathematically, the SM is a quantized Yang-Mills theory based on the non-abelian
 224 symmetry group $U(1) \rightarrow SU(2) \rightarrow SU(3)$ and has a total of twelve gauge bosons: the photon,
 225 three weak bosons and eight gluons. The interactions included in such a model are the
 226 electromagnetic force, the weak force and the strong one. Quarks have a property called
 227 color, playing the role of charge in the strong force. Both quarks and leptons are affected
 228 by the weak force and all the charged particles interact electromagnetically. The models
 229 that describe these interactions are listed as follows:

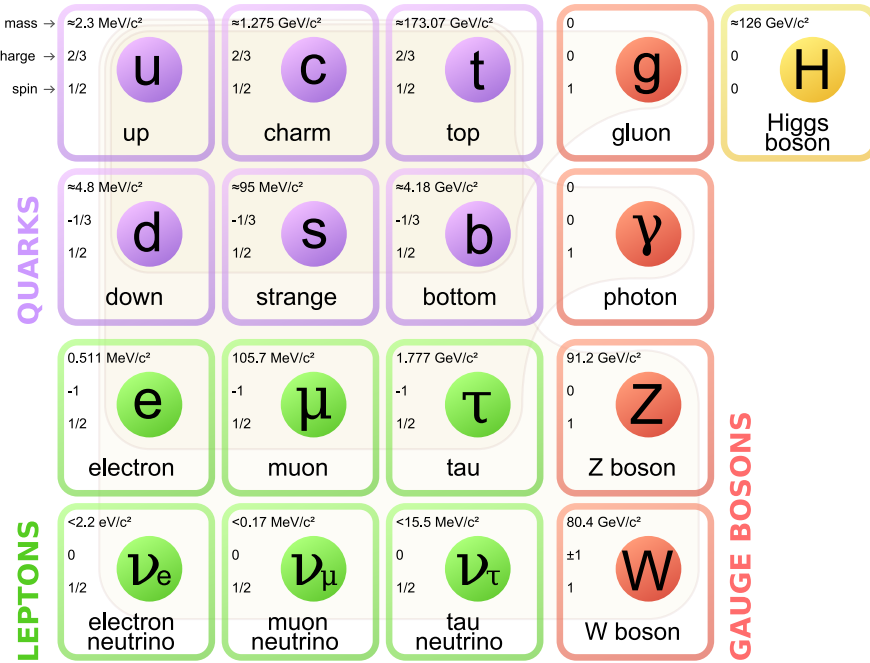


Figure 1: Standard Model families of leptons and quarks as the gauge bosons

230 **Quantum Electro-Dynamics (QED)** describes how light and matter interact. This
231 is the first theory where full agreement between quantum mechanics and special relativity
232 is achieved. It was developed between 1946 and 1950 by Tomonaga Shinichiro, Julian S.
233 Schwinger and Richard P. Feynmann. They were awarded the Nobel prize in 1965.

234
235 **Electroweak Theory (EW)** is the unified description of two of the four known funda-
236 mental interactions of nature: electromagnetism and the weak interaction. It first appeared
237 in 1961, driven by Sheldon Lee Glashow, and was completed in 1967 by Abdus Salam and
238 Steven Weinberg. They were awarded the Nobel prize in 1979. The first measurement
239 of the existence of the weak bosons W^+ , W^- and Z^0 was performed in 1983, when they
240 were produced and directly observed in $S\bar{p}\bar{p}S$ collisions at CERN. During the next year the
241 Nobel prize for this experimental result was assigned to Carlo Rubbia and Simon van der
242 Meer. In 1999 Gerardus 't Hooft and Martinus Veltman were awarded the Nobel prize for
243 showing that the electroweak theory is renormalisable.

244
245 **Quantum Chromo-dynamics (QCD)** is the theory of the strong interaction (color
246 force), describing the interactions between quarks and gluons which make up the hadrons.
247 Starting from the classification of the large amount of particles discovered during the fifties,
248 the original idea of the quark model by Gell-Mann (Nobel Prize in 1969) has been developed
249 during the sixties until 1973, when David J. Gross, H. David Politzer and Frank Wilczek
250 discovered the ?asymptotic freedom? property of the strong nuclear interaction (Nobel
251 Prize in 2004).

252 1.2 QCD and Quark-Gluon plasma

253 When, starting in 1950s, the number of known particle species became large, the idea
254 that these could be the elementary constituents of matter was replaced by the notion
255 that these species could in fact be composite objects made up of fewer, more elementary
256 particles, in a similar way to what had already happened to the elements of Mendeleev's
257 Periodic Table. The original idea by Gell-Mann (1964) was that the hadrons could be
258 obtained as combination of the fundamental representation of an $SU_f(3)$ group, where
259 three different flavors of quark ($q = u, d, s$) combine to build mesons ($q\bar{q}$) and hadrons
260 (qqq). However, when cataloging hadrons using the $SU_f(3)$ group, there are anomalous
261 states, such as the $\Omega^-(sss)$ and the $\Delta^{++}(uuu)$, that are combinations of three quarks of
262 the same flavor, in clear contrast with the Pauli exclusion principle for fermions. A solution
263 was proposed in 1965 by Moo-Young Han with Yoichiro Nambu and Oscar W. Greenberg,
264 who independently solved the problem by proposing that quarks possess an additional
265 $SU(3)$ gauge quantum number, later called color charge. This new quantum number may
266 assume three states, represented by the three primary colors: red, green and blue (denoted
267 symbolically by R, G and B, respectively). The introduction of this new quantum number
268 also provides an explanation to other empirical evidence, such as the fact that no qq , $\bar{q}q$

269 or the single quark have never been observed directly. On the other hand, the existence of
 270 color charge gives rise to the possible existence of differently colored states for each particle;
 271 thus, we could have many states for the proton, such as $u_R u_G d_B$, $u_R u_G d_G$, $u_B u_R d_R$, and
 272 so on. The fundamental rule that solves such contradictions is that all the particle states
 273 observed in nature are "colorless" or "white" (or, to be more precise, unchanged under
 274 $SU_c(3)$ rotations). The dynamics of the quarks and gluons are controlled by the gauge
 275 invariant QCD Lagrangian:

$$\mathcal{L}_{QCD} = \underbrace{i\delta_{ij}\bar{\Psi}_q^i\gamma^\mu\partial_\mu\Psi_q^j}_{\mathcal{L}_1} + \underbrace{g_s\bar{\Psi}_q^i\gamma^\mu t_{ij}^a A_\mu^a\Psi_q^j}_{\mathcal{L}_2} + \underbrace{m_q\bar{\Psi}_q^i\Psi_q^j}_{\mathcal{L}_3} + \underbrace{\frac{1}{4}F_{\mu\nu}^a F^{a\mu\nu}}_{\mathcal{L}_4} \quad (1)$$

276 where the coloured gluon field tensor, $F_{\mu\nu}^a$ (with color index a) and the squared gauge
 277 coupling parameter, g_s^2 (associated to the strong coupling constant α_s) are defined as:

$$F_{\mu\nu}^a = \partial_{mu}A_\nu^a - \partial_\nu A_\mu^a + g_s f^{abc} A_\mu^b A_\nu^c \quad (2)$$

278 and

$$g_s^2 = 4\pi\alpha_s \quad (3)$$

279 where:

- 280 • Ψ_q^i : the quark field with flavor q and color index $i \in [1;3]$, such as $\Psi_q = (\Psi_{qR}, \Psi_{qG},$
 281 $\Psi_{qB})^T$ and A_μ^a is the gluon field with color index a (adjoint representation)
- 282 • γ^μ : Dirac matrices that express the vector nature of the strong interaction, with μ
 283 being the Lorentz vector associated index
- 284 • m_q : quark mass, a priori not equal to zero (resulting from the Higgs mechanism or
 285 equivalent)
- 286 • t_{ij}^a : generator matrices of the group $SU_c(3)$, proportional to the Gell-Mann matrices,
 287 that perform revolutions in color space, representing interaction of quarks and gluons
- 288 • f^{abc} : structure constant of QCD

289 Each of the four terms of the QCD Lagrangian expresses and aspect of the interaction,
 290 specifically:

- 291 • \mathcal{L}_1 : gives the kinetic energy of the quark field Ψ_q^i
- 292 • \mathcal{L}_2 : gives the interaction between quarks (fermions) and gluons (the bosons of the
 293 interaction)
- 294 • \mathcal{L}_3 : gives the mass of the quarks

- 295 • \mathcal{L}_4 : gives the kinetic energy of the gluons

296 The terms of this equation, together with the fundamental parameters α_s and m_q ,
 297 summarize in just one expression all the features of the strong interaction. The first three
 298 terms describe the free propagation of quarks and gluons and the quark-gluon interaction.
 299 The remaining two terms show the presence of three and four gluon vertices in QCD and
 300 reflect the fact that gluons themselves carry color charge. This is a consequence of the non-
 301 abelian4 character of the gauge group. This peculiarity of the QCD interaction imposes the
 302 evolution of the strong coupling constant, α_s . The corresponding trend has been measured
 303 experimentally, and compared in Figure 2 with predictions. A practical consequence of
 304 this behavior is that the corresponding potential has a completely different shape than the
 305 other fundamental interactions and can be expressed by the following equation:

$$V(r) = -4 \frac{\alpha_s}{3r} + kr \quad (4)$$

306 where r is the separation distance between the two quarks and k is a constant that is
 307 approximately 1 GeV/fm.

308 Three are main properties of the QCD interaction:

309 **Confinement** At large distances between quarks and gluons (i.e. small values of trans-
 310 ferred momentum Q in Figure 2) the coupling constant is large and the associated force
 311 is strong enough to keep these elementary con- stituents (usually called partons) confined
 312 in bounded states. As expressed in the Equation 4, the attractive potential increases with
 313 the increasing of the relative distance between the two partons preventing the separation
 314 of an individual quark or gluon. This explains the meaning of the term "confinement"
 315 adopted to describe this energy regime. From the theoretical point of view, the large value
 316 of α_s make impossible any perturbative approach in the solution of the Hamilton equation
 317 of the system. A successful solution is to perform the study of the system on a discrete
 318 space. Such techniques are known as lattice QCD and are based on numerical Monte Carlo
 319 simulations. The challenge for the calculations is to reduce the lattice spacing in order to
 320 approach the continuum.

322 **Asymptotic freedom** Reducing the distance between quarks and gluons (i.e. increas-
 323 ing Q in Figure 2) the coupling constant α_s becomes smaller. As anticipated, this is a
 324 unique feature among the forces and comes from the non-abelian nature of the QCD gauge
 325 symmetry. Such a phenomenon is also depicted by the weakening of the anti-screening
 326 effect of the surround- ing virtual gluons with decreasing distance. In this way two quarks
 327 closer and closer in space show each other a smaller and smaller color charge. **Chiral**
 328 **symmetry** One further property of interest is connected to the chirality of the quark. It
 329 can be verified that the QCD lagrangian for massless quarks is invariant under a chiral
 330 rotation ($SU_L(N_f) \times SU_R(N_f)$), while the operator $\bar{q}q = \bar{q}_L q_R + \bar{q}_R q_L$ is not invariant (in

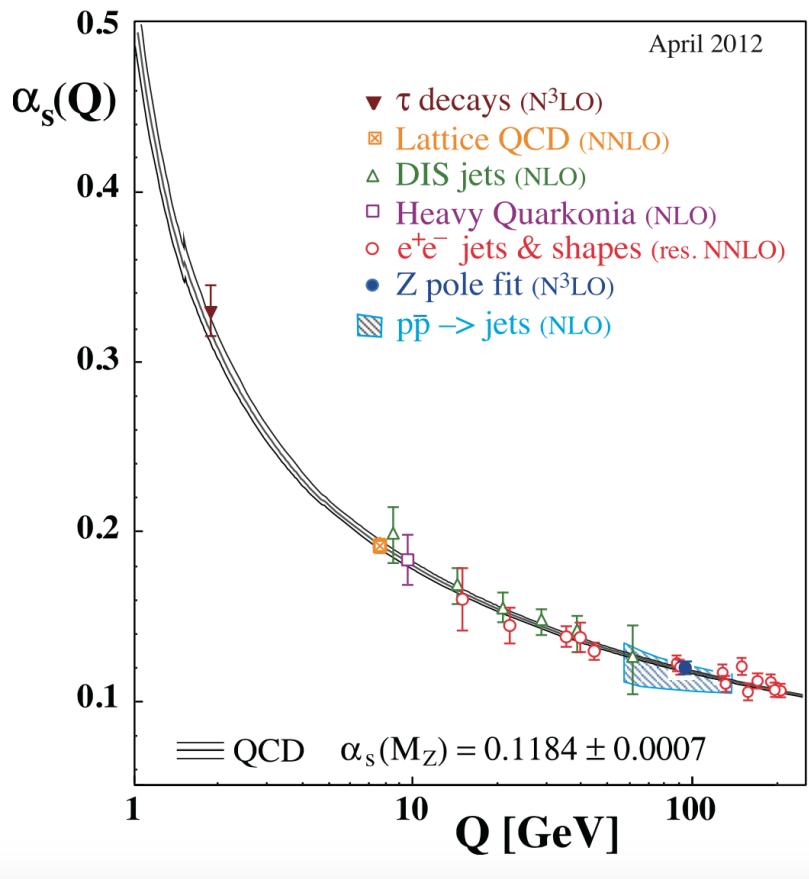


Figure 2: Summary of measurements of α_s as a function of the respective energy scale Q . The respective degree of QCD perturbation theory used in the extraction of α_s is indicated in brackets (NLO: next-to-leading order; NNLO: next-to-next-to leading order; res. NNLO: NNLO matched with resummed next-to-leading logs; N3LO: next-to-NNLO) [1]

332 the axial part), meaning that the mesons (state $\bar{q}q$) should have the same mass. Experi-
333 mentally this is clearly not true, and it could be shown that the axial current is conserved
334 (PCAC and the Goldberger-Treiman relation). The solution to this puzzle is that the chi-
335 ral (axial-vector) symmetry is spontaneously broken; this means that the symmetry of the
336 Hamiltonian is not a symmetry of the corresponding ground state. It has also been shown,
337 by G. t?Hooft, that the confinement implies a dynamical breaking of the chiral symmetry
338 [7]; this means that the breaking comes from the interaction between the objects in the
339 system. From this follows that the masses of the quarks are strongly increased because of
340 the interaction with the constituents of the system. This mechanism, known as dynamical
341 chiral symmetry breaking justifies the mass of the hadrons, reducing the role of the Higgs
342 mechanism in the mass explanation at least for the light hadrons.

343 **1.3 Heavy Ion Collisions**

344 In the case a QGP is formed, it will eventually expand because of its internal pressure.
345 As the system expands it also cools. The space-time evolution of the expansion can be
346 seen in Figure 3 (right side). A and B represent the two incoming ion beams. After a pre-
347 equilibrium phase a QGP is formed. As it expands, the system will eventually reach what
348 is known as the critical temperature (T_c). At this point partons begin to hadronize and this
349 will continue until the chemical freeze-out (T_{ch}) takes place, when inelastic collisions cease.
350 At this stage the distribution of hadrons is frozen. As cooling and expansion continue the
351 hadrons reach what is called thermal freeze out (T_{fo}). Here the elastic collisions stop and
352 the hadrons carry fixed momenta. The QGP state can not be directly observed, because of
353 its short lifetime. Instead, through experiment we measure the final state hadrons, which
354 have a fixed momentum after T_{fo} . The observables of interest should tell us about the
355 de-confinement and the thermodynamic properties of the matter. Moreover, experimental
356 measurements include yields and p_T spectra of various particle species, azimuthal studies
357 of high p_T particles, phase space distributions, and particle correlations.

358 A practical way to reach a critical condition in which a nuclear system should undergo
359 a phase transition to the QGP, at high temperature and/or matter density, is to collide
360 two nuclei at sufficiently high energy. Therefore, relativistic and ultra-relativistic heavy-ion
361 collisions are a unique tool to study nuclear matter under extreme conditions.

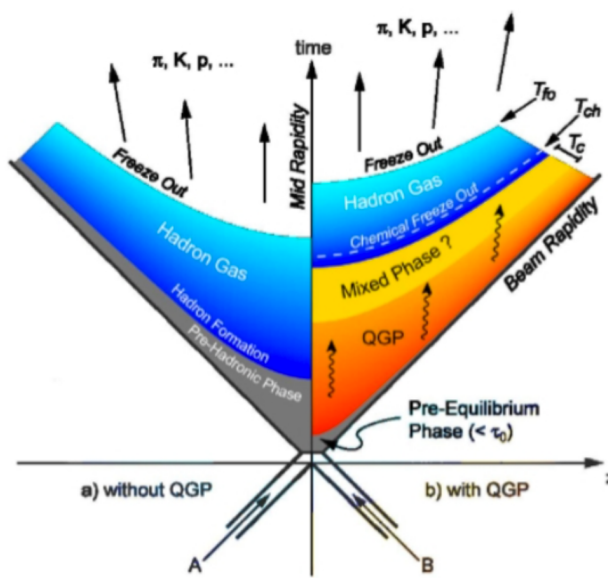


Figure 3: Hydrodynamic evolution of a heavy ion collision with and without the formation of a QGP.

362 **2 Theoretical models**

363 **2.1 Thermal statistical model**

364 The statistical-thermal model has proved extremely successful in applications to relativistic
365 collisions of both heavy ions and elementary particles. In light of this success, THERMUS,
366 a thermal model analysis package, has been developed for incorporation into the object-
367 oriented ROOT framework [15].

368
369 There are three types of statistical-thermal models in explaining data in high energy nu-
370 clear physics and THERMUS treats the system quantum numbers B (baryon number), S
371 (strangeness) and Q (charge) within three distinct formalisms:

- 372 1. **Grand-Canonical Ensemble:** Because the hot dense matter produced in nucleus-
373 nucleus collisions is large enough, this ensemble is the most widely used in applications
374 to heavy-ion collisions, in which the quantum numbers are conserved on average.
- 375 2. **Fully-Canonical Ensemble:** In which B, S and Q are each exactly conserved and
376 this ensemble used in high-energy elementary collisions such as pp, p \bar{p} and e $^-$ e $^+$
377 collisions.
- 378 3. **Strangeness-Canonical Ensemble:** In small systems or at low temperatures, a
379 canonical treatment leads to a suppression of hadrons carrying non-zero quantum
380 numbers, since these particles have to be created in pairs and the resulting low
381 production of strange particles requires a canonical treatment of strangeness.

382 In order to calculate the thermal properties of a system, one starts with an evaluation
383 of its partition function. The form of the partition function obviously depends on the
384 choice of ensemble. In the present analysis the strangeness-canonical ensemble used and
385 the statistical-thermal model requires six parameters as input: the chemical freeze-out
386 temperature T , baryon and charge chemical potentials μ_B and μ_Q respectively, canonical
387 or correlation radius, R_C ; the radius inside which strangeness is exactly conserved and the
388 fireball radius R . An additional strangeness saturation factor γ_S has been used as indicator
389 of a possible departure from equilibrium and $\gamma_S = 1.0$ corresponds to complete strangeness
390 equilibration.

391 The volume dependence cancels out when studying the particle ratios as well as strangeness
392 canonical equivalent to grand canonical formalism if $\Delta S = 0$ in the ratios and γ_S also can-
393 celes out. Parameters used in the analysis listed in Table 1. The μ_B parameter taken from
394 the Ref. [16].

395

Table 1: Parameters used in the thermal-model calculations.

Parameter	Value
T (MeV)	varied (see text)
μ_B (MeV)	$9.2 \times 10^{-2}????$
μ_Q (MeV)	0.0
γ_S	1.0

396 2.1.1 Calculations

397 *Concept:*

398 In order to calculate the particle ratios within strangeness canonical formalism of THER-
 399 MUS, temperature varied between 60 MeV to 180 MeV and particle yields extracted for
 400 each temperature value and then primary particle ratios calculated for each case.

401

402 *Feed-Down Correction:*

403 Since the particle yields measured by the detectors in collision experiments include feed-
 404 down from heavier hadrons and hadronic resonances, the primordial hadrons are allowed to
 405 decay to particles considered stable by the experiment before model predictions are com-
 406 pared with experimental data. In the analysis only Λ particles counted as stable (do not
 407 allowed to decay) so there is no feed-down contribution from these particles to the other
 408 ratios.

409

410

411 Properties of studied particles and their particle ratios listed in Table 2 and Table 3,
 412 respectively.

413

414

415 2.1.2 Results

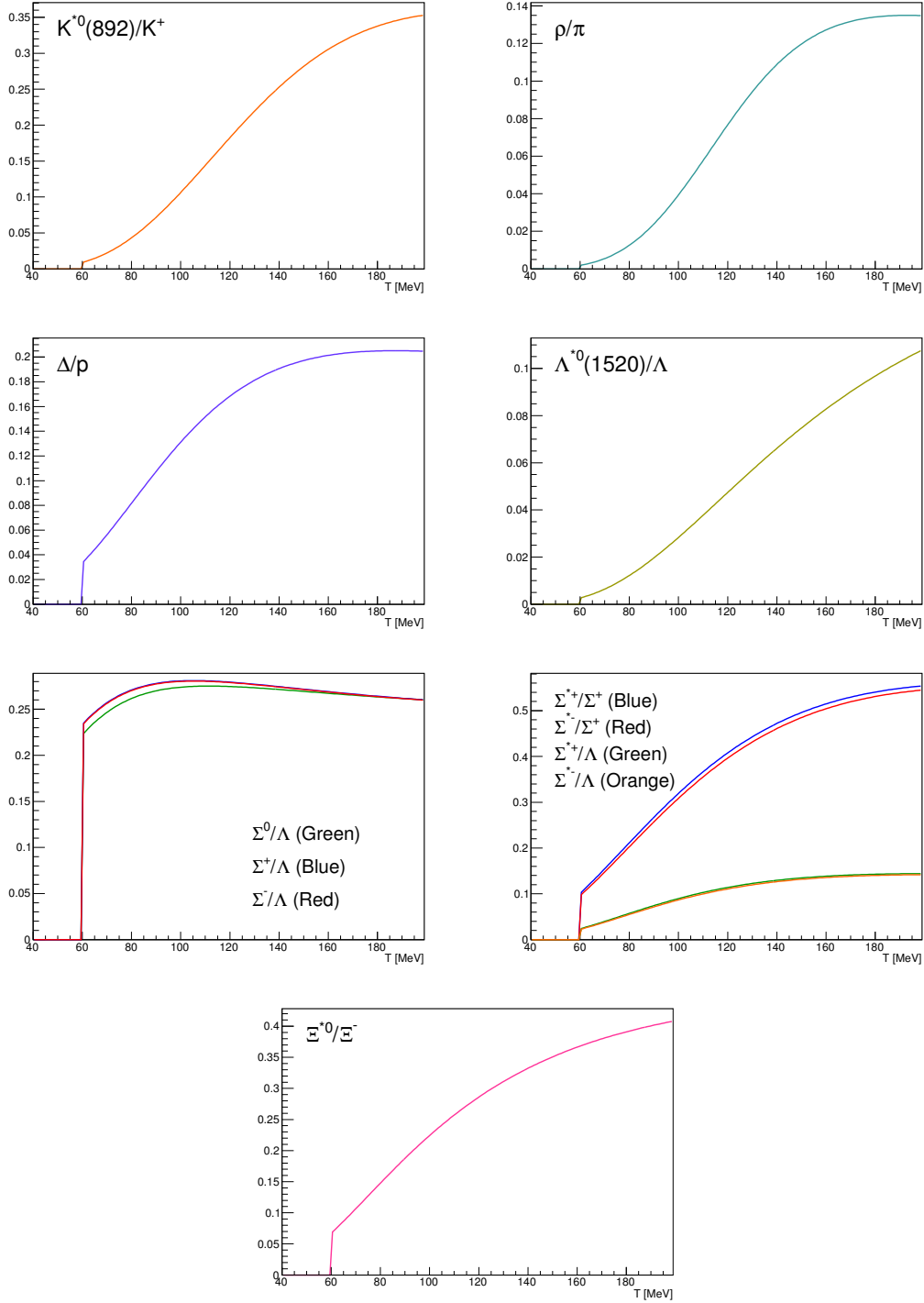


Figure 4: Ratio of baryonic and mesonic resonances over their stable partner as a function of temperature.

Table 2: Properties of particles used in the ratio calculations.

Particle	Δ^{++}	p	K^{*0}	K^0	K^+	Λ^*	Λ	Σ^{*+}	Σ^+	Σ^0
Mass (MeV/c^2)	1232	938.27	895.92	497.61	493.67	1519.5	1115.68	1382.8	1189.37	1192.6
Width (MeV/c^2)	120	—	50.7	—	—	15.6	—	37.6	—	—
$c\tau$ (fm)	1.6	—	3.9	—	—	12.6	—	5.51	—	—
Ang. Momentum (J)	3/2	1/2	1	1	0	3/2	1/2	3/2	1/2	1/2
Isospin (I)	3/2	1/2	1/2	1/2	1/2	0	0	1	1	1
Parity (P)	+1	+1	-1	-1	0	-1	+1	+1	+1	+1
Strangeness (S)	0	0	1	1	1	-1	-1	-1	-1	-1
Baryon Number (B)	1	1	0	0	0	1	1	1	1	1
Decay Channel	$p\pi^+$	—	π^-	—	$\mu^+\nu_\mu$	pK^-	$p\pi^-$	$\Lambda\pi^+$	$p\pi^0$	$\Lambda\gamma$
Branching Ratio (%)	~ 100	—	~ 66.7	—	~ 63.54	~ 45	~ 63.9	~ 87	~ 51.6	~ 100
Q-Value(MeV/c^2)	154.16	—	262.68	—	—	87.55	37.84	127.55	111.53	76.96

 Table 3: Difference of mass (ΔM), baryon number (ΔB), strangeness (ΔS) and charge (ΔQ) of the ratios. The values of the slopes needs to be checked!!!!

Particle	Δ^{++}/p	K^*/K^+	Λ^*/Λ	Σ^{*+}/Λ	Σ^{*+}/Σ^0	Σ^0/Λ	Σ^{*+}/Σ^+	Ξ^{*0}/Ξ^-
ΔM (MeV/c^2)	293.8	402.25	403.82	267.12	190.16	76.96	193.43	210.49
ΔB	0	0	0	0	0	0	0	0
ΔS	0	0	0	0	0	0	0	0
ΔQ	+1	-1	0	+1	0	+1	0	-1
Slope (%) per MeV ??????	0.19	0.76	0.98	0.25	-	-0.08	0.37	0.42

⁴¹⁶ **2.1.3 Comparison with data**

⁴¹⁷ **2.2 UrQMD**

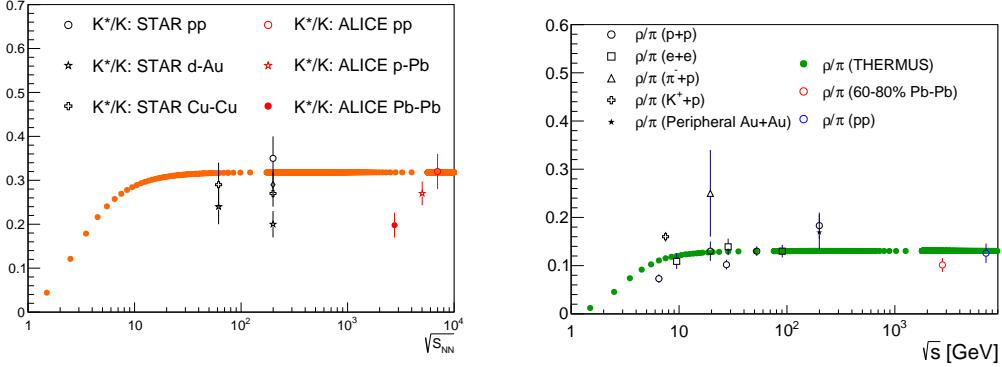


Figure 5: Ratio of resonances over their stable partner as a function of $\sqrt{(s)}$.

418 3 Production of resonance with strangeness

419 The Quark Model, proposed independently by Murray Gell-Mann and Yuval Ne?eman in
 420 1964 [13], enables the classification of hadrons in terms of their constituent quarks. In
 421 this model, the lighter mesons and baryons are representations of an $SU_f(3)$ group, whose
 422 fundamental representation is the three dimensional vector (u, d, s). These are the three
 423 lighter quarks whose characteristics are reported in Table reftable:quark.

Light flavor	d	u	s
Baryon number (B)	+1/3	+1/3	+1/3
Electric charge (Q)	-1/3	+2/3	-1/3
Isospin (I)	-1/2	+1/2	0
Strangeness (S)	0	0	-1
mass (MeV/c^2)	$2.3^{+0.7}_{-0.5}$	$4.8^{+0.5}_{-0.3}$	95 ± 5

Table 4: Quantum numbers and masses associated to the three lighter quarks: u, d and s

424 The hadronic state are obtained from the decomposition of the following scalar prod-
 425 ucts of the fundamental representations of the group:

426

$$427 \text{ Meson } (q\bar{q}) \text{ } 3 \otimes \bar{3} = 1 \oplus 8$$

428

$$429 \text{ Baryon } (qqq) \text{ } 3 \otimes 3 \otimes 3 = 10_S \oplus 8_M \oplus 8_M \oplus 1_A$$

430

431 For the baryons without c or b quark, flavor and spin may be combined in an approxi-

432 mate flavor-spin SU(6), in which the six basic states are $d \uparrow, d \downarrow, \dots, s \downarrow$ (\uparrow, \downarrow = spin up,
 433 down). Then the baryons belong to the multiplets on the right side of

434

$$435 \quad 6 \otimes 6 \otimes 6 = 56_S \oplus 70_M \oplus 70_M \oplus 20_A$$

436

437 Here, the 56 representation can be decompose in an octet ($J^P = 1/2^+$) and a decuplet
 438 ($J^P = 3/2^+$), as can be seen in Figure 6 and Figure 7.

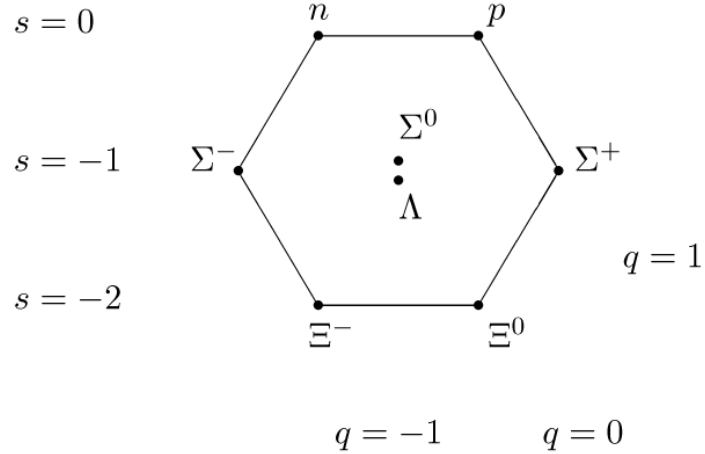


Figure 6: The $J^P = 1/2^+$ ground state baryon octet

439 Among the hadrons, the special family of particles that contain at least one strange
 440 quark but not heavier quarks (like charm or bottom), are called hyperons. These are:
 441 the $\Lambda(\text{uds})$, the triplet $\Sigma^+(\text{uus}), \Sigma^0(\text{uds}), \Sigma^-(\text{dds})$, the doublet $\Xi^-(\text{dss}), \Xi^0(\text{uss})$ and the
 442 $\Omega(\text{sss})$ and the corresponding antiparticles. Ξ and Ω are the only hyperons containing more
 443 than one strange quark, hence they are called multi-strange baryons. Resonances shown in
 444 Figure reffig:decuplet having * with its name (e.g. $X^{*\pm}$) are particles with higher mass than
 445 the corresponding ground state particle with the same quark content. Different resonances
 446 with different lifetimes can probe different stages of the fireball expansion. The lifetime
 447 of some short-lived resonances is reported in Table 5. The ratios between resonances and
 448 stable hadrons can be compared for resonances with different lifetimes and provide insights
 449 on the role of the re-scattering effect between the two freeze-out phases.

450 In the following, a general overview of the role of the strange quark within the QGP
 451 studies with heavy-ion collisions is given. And importance of the measurement of resonance
 452 is explained as probe of properties in hadronic phase between the chemical(T_{ch}) and the

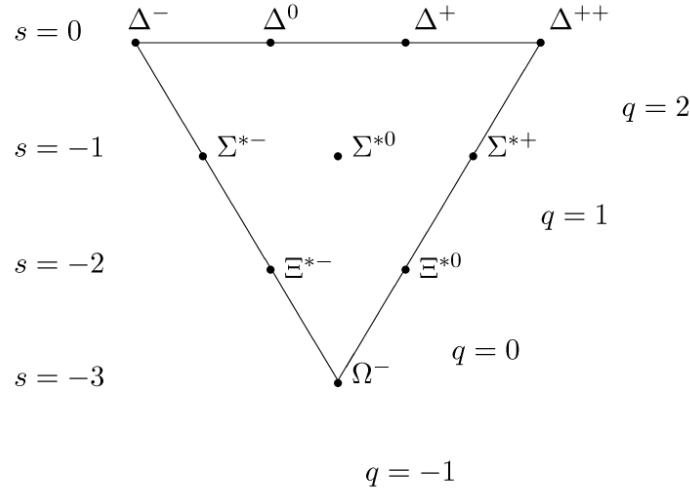


Figure 7: The $J^P = 3/2^+$ baryon decuplet

Particle	$\rho(770)$	$\Delta(1232)$	$K^*(892)$	$\Sigma(1385)$	$\Lambda(1520)$	$\Xi(1530)$	$\Phi(1020)$
Lifetime[c τ]	1.3 fm	1.7 fm	4.0 fm	5.5 fm	10.3 fm	22 fm	46 fm

Table 5: Lifetime of hadronic resonances

453 kinetic freeze-out(T_{kin}).

454

3.1 Strange quark and hyperons

455 The original interest in the strangeness in the context of the QGP comes from an idea by
 456 Johann Rafelski and Berndt Müller. In 1982, they suggested a possible signature for the
 457 formation of a QGP in a heavy-ion collision [14]. The key argument, at a fixed collision
 458 energy, rests on the different production mechanism of the s quark within two different
 459 systems:

460 **1. Hadron Gas (HG)** , where the degrees of freedom are the hadronic ones, as quark
 461 and gluons are confined

462 **2. QGP** , where the degrees of freedom are partonic ones, with quarks and gluons free
 463 with respect to each other

464 The mass of the hadrons is only partly due to the mass of the constituent valence
 465 quarks.

466 Naively speaking, the quarks ?dress up? due to the strong interaction that keeps them
467 confined. Once they are free, as in a QGP, the quarks recover their bare masses. It was
468 predicted that, if the QGP is formed, an enhancement of the strange quarks should occur,
469 because the production of $s\bar{s}$ pairs becomes easier due to the lower energy needed. When
470 the QGP cools down, these strange quarks eventually recombine into hadrons favoring also
471 an enhancement of the number of strange hadrons. This effect is larger for hadrons with
472 higher strangeness, with the following scaling for the number type:

473

474 $N_\Omega > N_\Xi > N_\Lambda$

475 where N_Ω , N_Ξ , N_Λ are the number of produced Ω , Ξ and Λ . A certain enhancement of
476 strange hadrons can occur also in a hadron gas system, but the processes of hadronisation
477 in this case are relatively easy for K and Λ . and progressively harder for hadrons with
478 higher strangeness, hence the relation would be:

479

480 $N_\Omega < N_\Xi < N_\Lambda$.

481 The production of multi-strange hadrons with respect to pp - like collisions is considered
482 to be a signature of the formation of the QGP and it was observed at SPS, RHIC and LHC.
483 [42]

484 The measured enhancement factors of baryons with increasing strangeness content are
485 reported in Figure 8 as a function of the number of participant nucleons, $\langle N_{part} \rangle$, in com-
486 parison with similar measurements at SPS and RHIC. For p–Pb collisions there is no
487 evidence of enhancement. For Pb–Pb collisions the enhancement increases with centrality
488 and the effect is larger for particles with higher strangeness content, up to a factor ?20 for
489 ?s. No hadronic model has reproduced these observations and they can be interpreted as
490 clear signal of QGP state formation. The comparison with results from the previous ex-
491 periments shows that the relative enhancements decrease with increasing collision energy.
492 An explanation of this behavior is given in terms of a statistical model, with canonical
493 strangeness conservation. In a small system, with small particles multiplicities, quantum
494 numbers conservation laws (such as strangeness) must be applied locally, event-by-event,
495 whereas in a large system, with many degrees of freedom, they can be applied in average,
496 by means of the corresponding chemical potential. The conservation of quantum numbers
497 is known to reduce the phase space available for particle production. This canonical sup-
498 pression factor decreases with lower energy in the centre of mass of the collisions and could
499 explain the larger enhancement for lower energy systems.

500 **3.2 Resonance production**

501 Resonances are particles with higher mass than the corresponding ground state particle
502 with the same quark content. Hadronic resonances decay strongly, thus with a short
503 lifetime, $\tau \sim$ few tenths of fm/c. The resonance natural width is given by $\Gamma = \hbar/\tau$, that
504 is inversely proportional to the lifetime. Broad states with finite Γ decay very shortly

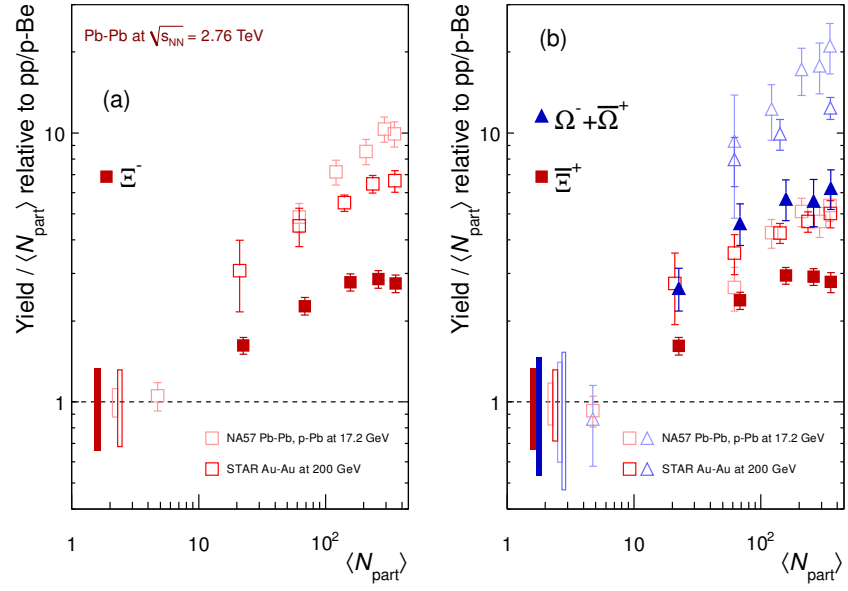


Figure 8: Enhancements in the rapidity range $|y| < 0.5$ as a function of the mean number of participants $\langle N_{part} \rangle$, showing LHC (ALICE, full symbols), RHIC and SPS (open symbols) data. Boxes on the dashed line at unity indicate statistical and systematic uncertainties on the pp or p-Be reference. Error bars on the data points represent the corresponding uncertainties for all the heavy-ion measurements and those for p-Pb at the SPS.

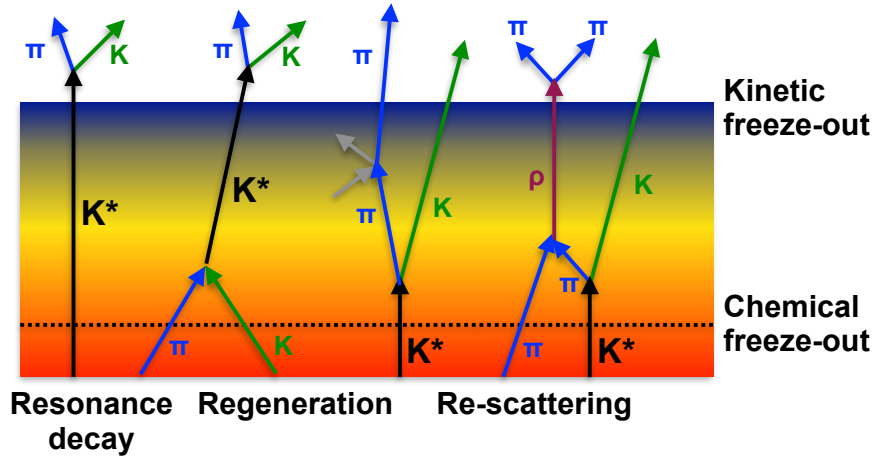


Figure 9: Hadronic phase

505 after being produced and can be measured only by reconstruction of their decay products
 506 (or "daughters") in a detector. In heavy-ion collisions, hadronic resonances are produced
 507 within the bulk of the expanding medium, where they can decay while still traversing its
 508 volume. Decay products may interact with the other particles of the medium (mostly pions
 509 at the LHC), resulting in the impossibility of reconstructing the resonance, because the
 510 invariant mass of the daughters does not match that of the parent particle. Conversely,
 511 resonances may be regenerated as a consequence of pseudo-elastic collisions in the time
 512 lapse between the chemical (T_{ch}) and the kinetic freeze-out (T_{kin}). Re-scattering and
 513 regeneration depend on the individual cross section, hence lifetime, of the resonances and
 514 affect the measurement of their yield and momentum spectrum. The yield is decreased if the
 515 re-scattering dominates, vice versa the regeneration feeds the system with more particles.
 516 The two effects may even compensate. Different resonances with different lifetimes can
 517 probe different stages of the fireball expansion. The ratios between resonances and stable
 518 hadrons can be compared for resonances with different lifetimes and provide insights on
 519 the role of the re-scattering effect between the two freeze-out phases.

520 **4 A Large Ion Collider Experiment at the LHC**

521 ALICE (A Large Ion Collider Experiment) has been collecting data during the whole first
522 phase of the Large Hadron Collider operations, from its startup on the 23 November 2009
523 to the beginning of the first long technical shutdown in February 2013. During the first
524 three years of operations LHC provided pp collisions at 0.9, 2.76, 7 and 8 TeV, Pb–Pb colli-
525 sions at 2.76A TeV and finally p–Pb collisions at 5.02 TeV. The first section of this chapter
526 focuses on the LHC performance during this phase and includes details on the accelerator
527 parameters that allow the LHC to perform as a lead ion collider. A detailed description
528 of the ALICE detector follows in the section 4.2.1. ALICE has been designed and op-
529 timized to study the high particle-multiplicity environment of ultra-relativistic heavy-ion
530 collisions and its tracking and particle identification performance in Pb–Pb collisions are
531 discussed. The attention is drawn in particular on the central barrel detectors. Section
532 4.2.2 describes the ALICE Data Acquisition (DAQ) system, that also embeds tools for the
533 online Data Quality Monitoring (DQM). The final part of the chapter is dedicated to the
534 offline computing and reconstruction system based on the GRID framework.

535 **4.1 The Large Hadron Collider**

536 The Large Hadron Collider (LHC) [17] at CERN is the biggest particle accelerator world-
537 wide. The LHC project was approved in 1994 and construction works in the existing
538 underground tunnel started in 2001 after the dismantling of the LEP collider, which had
539 previously been built in the tunnel which is located under the Swiss-French border area
540 close to Geneva at a depth of 50 to 175 m. The LHC has a circumference of 26.7 km. By
541 design, its maximum achievable energies are 7 TeV for beam of protons and 2.76 TeV per
542 nucleon for beam of lead ions, thus providing collisions at $\sqrt{s} = 14$ TeV and $\sqrt{s_{NN}} = 5.5$
543 TeV, respectively. These would be the largest energies ever achieved in particle collision
544 experiments. The LHC is a synchrotron that accelerates two counter-rotating beams in
545 separate parallel beam pipes. In each of them bunches of particles travel many times
546 around the accelerator ring before the collision energy is reached. The accelerator has to
547 bend the beams around the ring, keep the bunches focused and accelerate them to their
548 collision energy. Finally, the spatial dimension of the bunches has to be minimized in order
549 to attain high luminosity, which ensure a high number of collisions per time interval at
550 the collision points, i.e. a high luminosity. A combination of magnetic and electric field
551 components performs the mentioned tasks. Despite the high luminosity reached, only a
552 very small fraction of the particles of two bunches collides in a single bunch crossing. The
553 others leave the interaction region essentially uninfluenced, are defocused, and continue to
554 circulate in the accelerator.

555 Injection of bunches into the LHC (Figure 10) is preceded by acceleration in the
556 LINAC2, PS booster, PS, and SPS accelerators. The acceleration sequence is slightly
557 different for heavy-ions, in which case bunches pass the LINAC3, LEIR, PS, and SPS

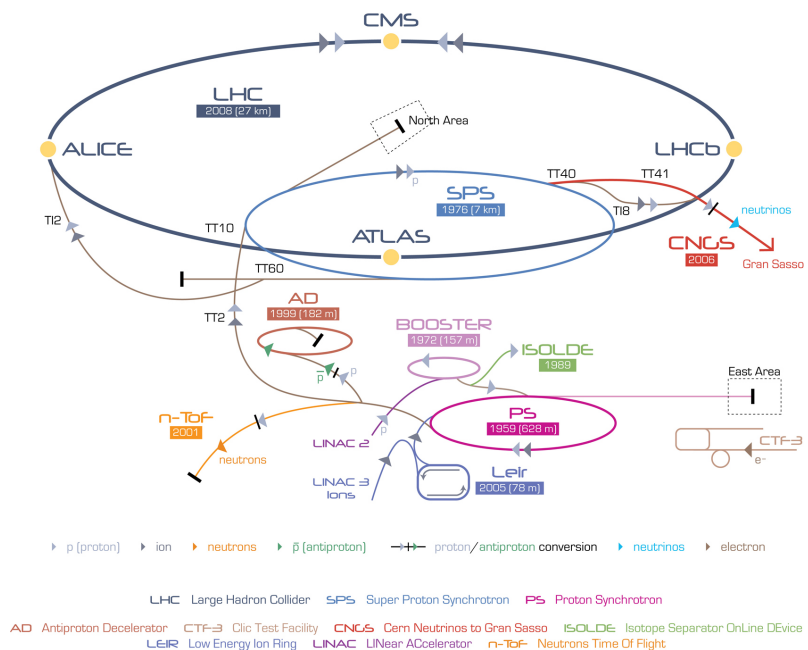


Figure 10: The CERN accelerator complex [2]

accelerators (more information can be found in [90]). Several injections to the LHC are needed until all bunches of both beams are filled. The first pp collisions at 900 GeV centre-of-mass energy were delivered by the LHC on September 10th 2008. Nine days later, the operations were interrupted due to a failure in an electrical connection between two magnets. The machine operators spent over a year repairing and consolidating the accelerator. On November 20th 2009 low energy proton beams circulated again, and a few days later, by achieving the energy of 1.18 TeV per proton beam, LHC became the most powerful accelerator in the world. The first pp collisions at centre-of-mass energy of 7 TeV were delivered in March 2010, and the first Pb?Pb collisions at centre-of-mass energy of 2.76 TeV per nucleon pair in November 2010. In 2010 the integrated luminosity delivered by the LHC was $\sim 48 \text{ pb}^{-1}$ for pp collisions at $\sqrt{s}= 7 \text{ TeV}$ ($\sim 0.5 \text{ pb}^{-1}$ in ALICE) and $\sim 10 \mu\text{b}^{-1}$ for Pb?Pb at $\sqrt{s_{\text{NN}}}= 2.76 \text{ TeV}$ ($\sim 10 \mu\text{b}^{-1}$ in ALICE). In 2011 the beam energy was the same as in 2010 both for pp and Pb-Pb. The performance of the LHC improved in terms of luminosity with $\sim 5.61 \text{ fb}^{-1}$ for pp ($\sim 2 \text{ pb}^{-1}$ in ALICE) and $\sim 166 \mu\text{b}^{-1}$ for Pb-Pb collisions ($\sim 143.62 \mu\text{b}^{-1}$ in ALICE). In 2012, the centre-of-mass energy for pp collisions was brought to 8 TeV and the integrated luminosity (up to December 2012, end of the pp program) was $\sim 23.3 \text{ fb}^{-1}$ ($\sim 10 \text{ pb}^{-1}$ in ALICE). A pilot p-Pb run operated at $\sqrt{s_{\text{NN}}}= 5.02 \text{ TeV}$ on September 2012, followed by a long p-Pb run on February 2013 with a delivered luminosity of 31.2 nb^{-1} . A very short pp run at $\sqrt{s}= 2.76 \text{ TeV}$ ended the Run1 of the LHC program, marking the start of the first long shutdown (LS1) until the end of 2014. Despite its excellent performance, the LHC has not yet achieved the nominal parameters (\sqrt{s}, L), that is the main goal for the next ignition of the machine in 2015. The LHC produces collisions in four so called Interaction Points (IPs) in correspondence of which are located six detectors of different dimensions and with different goals, all able to study the products of the interactions. These are:

ALICE (A Large Ion Collider Experiment-IP₂) [18] is a dedicated heavy-ion experiment designed to study strongly-interacting matter at very high energy density. It explores the phase transition to the QGP, its phase diagram, and its properties. Furthermore, ALICE will also study collisions of protons, on one hand as a baseline for heavy-ion measurements and on the other hand it contributes to measurements of identified particles by making use of its excellent particle identification capability and its acceptance at very low transverse momenta.

ATLAS (A Toroidal LHC ApparatuS-IP₁) and CMS (Compact Muon Solenoid - IP₅) [19][20] are general-purpose detectors for pp collisions that are built to cover the widest possible range of physics at the LHC. Specific topics are the search for the Higgs boson and physics beyond the Standard Model, e.g. new heavy particles postulated by supersymmetric extensions (SUSY) of the Standard Model and evidence of extra dimensions.

LHCb (The Large Hadron Collider beauty experiment-IP₈) [21] is a dedicated

599 experiment for the study of heavy flavor physics at the LHC. In particular, the experiment
600 focuses on the study of CP violation and rare decays of beauty and charm particles, to
601 test the Standard Model and to search for evidence of New Physics. The LHCb physics
602 program is complementary to the flavor physics studies conducted at the B-factories and
603 to the direct searches for new particles performed at ATLAS and CMS.

604

605 **LHCf (Large Hadron Collider forward experiment-IP₁)** [22] measures forward
606 particles created during LHC collisions to provide further understanding of high energy
607 cosmic rays. The detector is placed close to the ATLAS experiment.

608

609 **TOTEM (TOTal Elastic and diffractive cross-section Measurement-IP₅)** [23]
610 measures the total cross-section, elastic scattering, and diffractive processes. The detector
611 is located close to the CMS experiment.

612

613 4.2 The ALICE project

614 The ALICE experiment at the LHC [24] has as main goal the study of nuclear matter
615 under extreme conditions of temperature and energy density such as those reached in ultra-
616 relativistic heavy-ion collisions. The aim is to verify the QCD prediction of the existence of
617 a phase transition from the common hadronic matter to the Quark-Gluon Plasma. Since
618 ALICE is the only LHC experiment specifically designed for Pb–Pb collisions, it has to
619 be able to cope with the large multiplicities associated with these collision systems and at
620 the same time has to cover as many QGP-related observables as possible. ALICE is also
621 interested in the study of pp interactions, as these are crucial for a comparison with Pb–Pb
622 collisions, to tune Monte Carlo models and per se, like the other LHC experiments. With
623 respect to these experiments, ALICE is endowed with an excellent Particle IDentification
624 (PID) performance, obtained combining different PID techniques from different detectors
625 that are optimized in different momentum (p) regions.

626 4.2.1 ALICE detector

627 ALICE is a complex of 14 detector subsystems (Figure 11) that can be classified in three
628 groups:

629

630 **Central detectors** are housed in a solenoid magnet which provides the experiment
631 with a 0.5 T magnetic field and covers the pseudo-rapidity interval $-0.9 < \eta < 0.9$ (corre-
632 sponding to a polar acceptance $\pi/4 < \theta < 3\pi/4$). The azimuthal acceptance is 2π . They
633 are mainly dedicated to vertex reconstruction, tracking, particle identification and momen-
634 tum measurement. Starting from the interaction region and going outward, we find the
635 following detectors:

- 636 • Inner Tracking System (ITS)
- 637 • Time Projection Chamber (TPC)
- 638 • Transition Radiation Detector (TRD)
- 639 • Time Of Flight (TOF)

640 In the mid-rapidity region there are also three detectors with limited azimuthal accep-
641 tance:

- 642 • High Momentum Particle Identification Detector (HMPID)
- 643 • PHOton Spectrometer (POHS)
- 644 • ElectroMagnetic CALorimeter (EMCAL)

645 **Muon spectrometer** is placed in the forward pseudo-rapidity region ($-4.0 < \eta < -2.5$) and consists of a dipole magnet and tracking and trigger chambers. It is optimized to
646 reconstruct heavy quark resonances (such as J/Ψ through their $\mu^+\mu^-$ decay channel) and
647 single muons.

649 **Forward detectors** are placed in the high pseudo-rapidity region (small angles with
650 respect to the beam pipe). They are small and specialized detector systems used for
651 triggering or to measure global event characteristics. They are:

- 653 • Time Zero (T0) to measure the event time with precision of the order of tens of
654 picoseconds, as needed by TOF
- 655 • VZERO (V0) to reject the beam-gas background and to trigger minimum bias events
- 656 • Forward Multiplicity Detector (FMD) to provide multiplicity information over a large
657 fraction of the solid angle ($-3.4 < \eta < -1.7$ and $1.7 < \eta < 5$)
- 658 • Photon Multiplicity Detector (PMD) to measure the multiplicity and the spatial
659 distribution of photons on an event-by-event basis in the $2.3 < \eta < 3.7$ region
- 660 • Zero Degree Calorimeter (ZDC) to measure and trigger on the impact parameter. The
661 ZDC consists of two calorimeters, one for neutrons (ZDC:ZN) and one for protons
662 (ZDC:ZP), and includes also an electromagnetic calorimeter (ZEM)

663 The ALICE global coordinate system [25] is a right-handed orthogonal Cartesian system
664 with the origin X, Y, Z = 0 at the centre of the detector. The three Cartesian axes are
665 defined as follows: the X axis pointing towards the centre of the LHC, the Y axis pointing
666 upward and the Z axis parallel to the local mean beam line pointing in the direction opposite

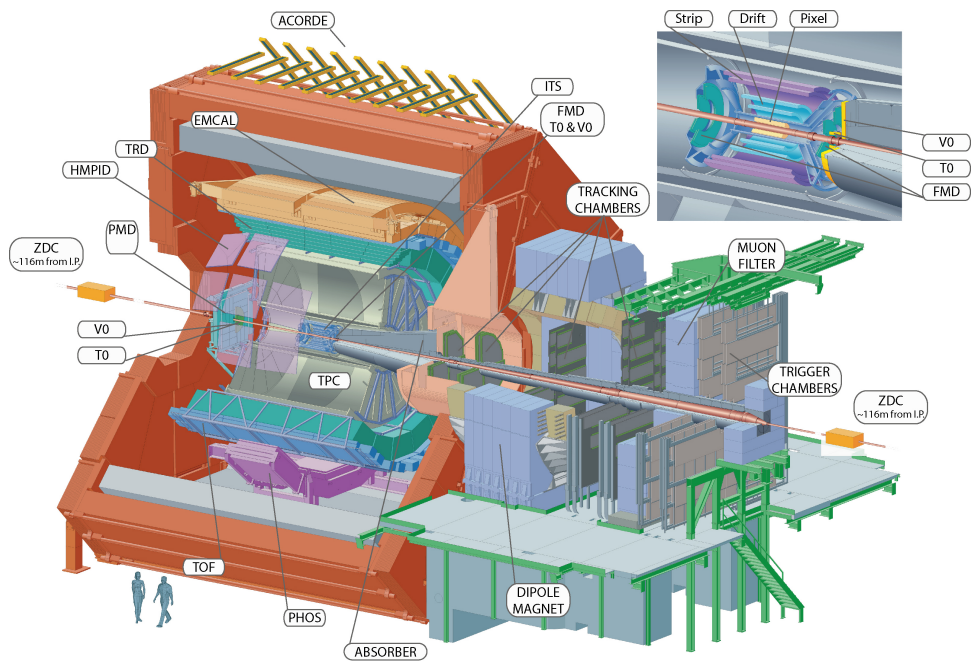


Figure 11: The ALICE detector

667 to the muon spectrometer. The azimuthal angle increases counter-clockwise from the
668 positive X axis ($\Phi = 0$) to the positive Y axis ($\Phi = \pi/2$) with the observer standing at
669 positive Z and looking at negative Z; the polar angle increases from the positive Z axis (θ
670 = 0) to the X-Y plane ($\theta = \pi/2$) and to the negative Z axis ($\theta = \pi$).

671 In the following Sections more specific descriptions of the detectors used in the identifi-
672 cation of the $\Xi(1530)^0$ baryons and in the determination of the characteristics of typical
673 collisions will be given.

674

ITS

675 The ITS [24] (Figure 12) is the barrel detector closest to the beam pipe. Its main goals
676 are:

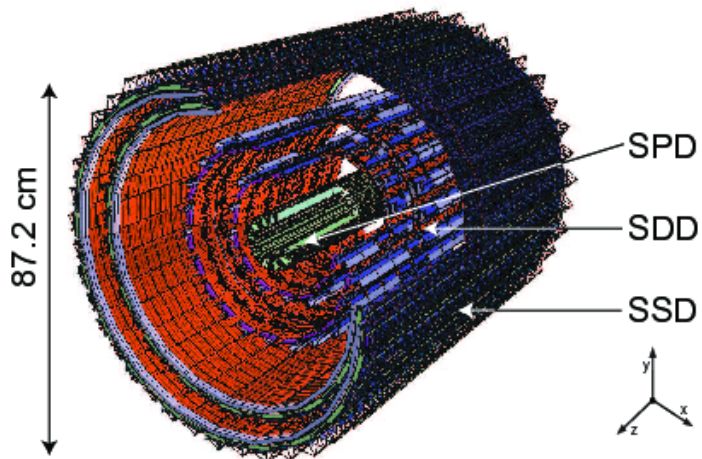


Figure 12: Schematic view of the ITS [3]

677

- 678 • to contribute with the TPC to the global tracking of ALICE by improving the angle
679 and momentum resolution
- 680 • to reconstruct the position of the primary interaction vertex
- 681 • to reconstruct secondary vertices from decays of heavy-flavor and strange particle
682 decays;
- 683 • to track and identify particles with momentum below $100 \text{ MeV}/c^2$
- 684 • to improve the momentum, impact parameter and angle resolution for the measure-
685 ment of high p_T particles performed with the TPC

- 686 • to reconstruct particles traversing dead regions of the TPC

687 The ITS surrounds the beam pipe (which is a 800 μm thick cylinder with an outer
 688 diameter of 2.9 cm) and consists of six cylindrical layers of silicon detectors located at radii
 689 between 4 cm and 43 cm. Due to the high track density, the two innermost layers are
 690 Silicon Pixel Detectors (SPD) which guarantee a high granularity. They are followed by
 691 two layers of Silicon Drift Detectors (SDD), while the two outmost layers are double-sided
 692 Silicon micro-Strip Detectors (SSD).

693 Since the momentum and impact parameter resolutions for low momentum particles
 694 are dominated by multiple scattering effects, the amount of material in the active volume
 695 has been minimized as much as possible. The granularity of the detector was optimized to
 696 keep the occupancy low in all the layers. With the technology chosen, the ITS detectors
 697 reach a spatial resolution of the order of a few tens of m resulting in a resolution on the
 698 impact-parameter⁵ better than 70 m in the r plane for $p_T > 1 \text{ GeV}/c$ and thus well suited
 699 for the reconstruction of heavy-flavor decays (see Figure 13).

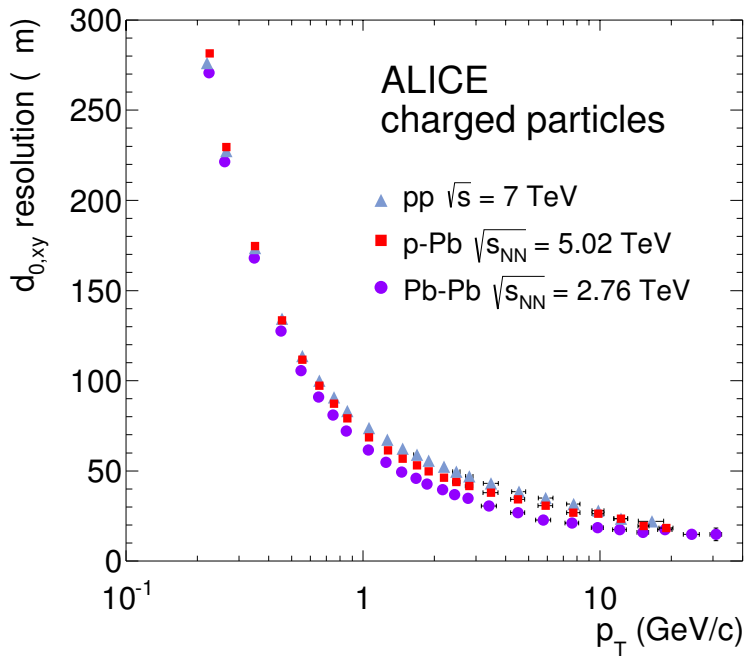


Figure 13: Track impact parameter resolution in the transverse plane ($r\phi$) vs p_T for charged particle

700 TPC

701 The TPC [26] (Figure 14) is the main tracking detector of the central barrel, optimized

702 to provide, together with the other central barrel detectors, charged- particle momentum
 703 measurements with good two-track separation, particle identification and vertex determina-
 704 tion. The TPC was designed for an excellent tracking performance in the high multiplicity
 705 environment of Pb–Pb collisions. For this reason, it was chosen to be a drift chamber,
 706 cylindrical in shape, 5 m long, with the inner radius ($r_{in} \sim 85$ cm) determined by the
 707 maximum acceptable track density, and the external one ($r_{ext} \sim 250$ cm) by the minimum
 708 track length for which dE/dx resolution is $< 10\%$. The TPC volume is filled with 90 m^3 of
 709 Ne/CO₂/N₂ (90/10/5). The readout planes are divided in 18 sectors in which multi-wire
 710 proportional chambers (with cathode pad readout) are housed. Because of its good dE/dx
 711 resolution, the TPC can identify particles with $p_T < 1\text{ GeV}/c$ on a track-by-track basis.

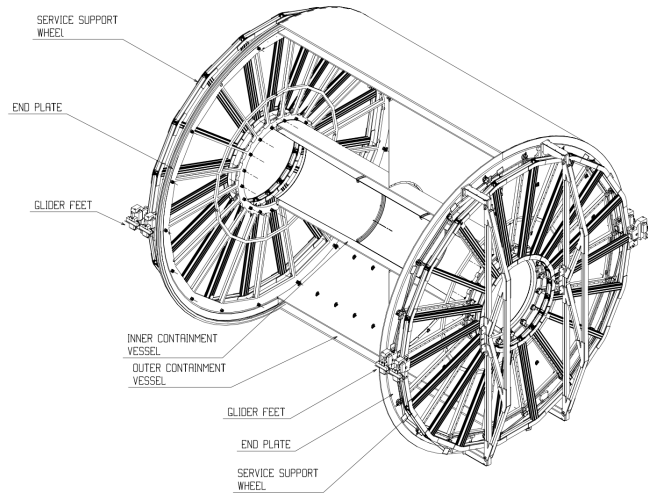


Figure 14: Schematic view of the TPC

712 Charged particles traveling through the TPC ionize the detector's gas; the measure-
 713 ment of this loss of energy is what we need to identify a particle. The physics observable
 714 in this case is the energy loss per unit length, within the matter crossed by the charged
 715 particle, which we call specific energy loss, also denoted by dE/dx . This is described by
 716 the Bethe–Bloch equation, 5, that highlights the key of the identification technique: this
 717 observable depends only on the charge and on velocity (β) of the particle, which, in turn,
 718 depends only on the momentum and the mass of the ionizing particle. Since momentum is
 719 already known due to track curvature and charge is unitary for most measured tracks, mea-
 720 suring the dE/dx allows us to indirectly determine mass and thus determine the particle
 721 species. The Bethe-Bloch equation gives the mean specific energy loss:

$$-\langle \frac{dE}{dx} \rangle = k_1 \cdot z^2 \frac{Z}{A} \cdot \frac{1}{\beta^2} \left[\frac{1}{2} \ln(k_2 \cdot m_e c^2 \cdot \beta^2 \gamma^2) - \beta^2 + k_3 \right] \quad (5)$$

722 where $\beta\gamma = p/Mc$ and: Z: atomic number of the ionized gas (in this case Ne/CO₂/N₂)
 723 A: mass number of the ionized gas (g/mol)
 724 m_e: electron mass
 725 z: electric charge of the ionizing particle in unit of electron charge e
 726 M: ionizing particle mass
 727 p: ionizing particle momentum
 728 β: ionizing particle velocity normalized to the light velocity c
 729 γ = 1/√(1 - β²), Lorentz factor
 730 k₁, k₂, k₃: constants depending on the ionized medium

731
 732 For a given ionizing particle mass hypothesis, a given momentum and a given length
 733 of the trajectory in the ionizing medium, the total charge deposited along the trajectory
 734 is subject to statistical fluctuations. This random variable follows a Landau distribution,
 735 that give us the opportunity to measure the mean value hdE/dx . The long tail of the
 736 Landau distribution is usually truncated at 50%-70% of the collected signal.

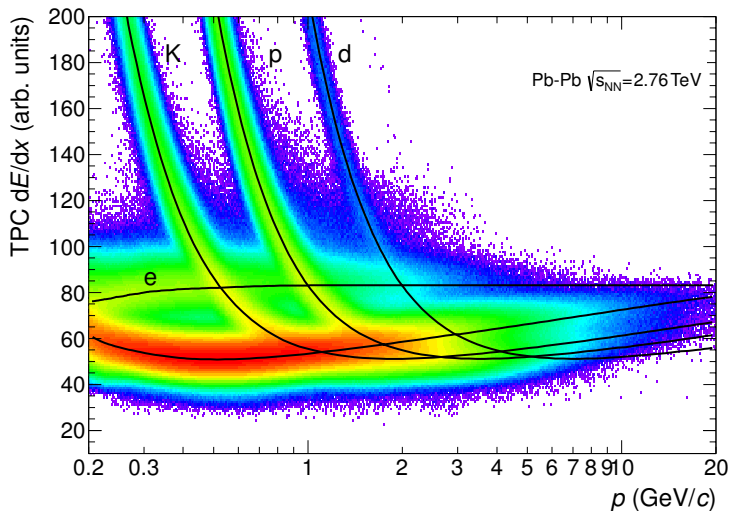


Figure 15: Specific energy loss (dE/dx) in the TPC vs. particle momentum in Pb–Pb collisions at $\sqrt{s_{NN}} = 2.76 \text{ TeV}$. The different bands characteristic for e^\pm , π^\pm , K^\pm , p^\pm are clearly visible. These are the evidence of the statistical distribution of the measured energy loss around the expected mean value. The expected value correspond to the prediction by a Bethe–Bloch experimental parametrization (superimposed as black lines in the Figure).

737 The specific energy loss in the TPC as a function of momentum is shown in Figure
 738 15. The different bands characteristic for e^\pm , π^\pm , K^\pm , p^\pm are clearly visible. These
 739 are the evidence of the statistical distribution of the measured energy loss around the
 740 expected mean value. The expected value correspond to the prediction by a Bethe–Bloch
 741 experimental parametrization (superimposed as black lines in the Figure). For a track

742 within the TPC the relevant quantity to be considered for PID is the difference between
 743 the measured specific energy loss and the corresponding predicted value, by the Bethe-
 744 Bloch parametrization for a given measured momentum. If normalized to the resolution
 745 of the dE/dx measurement in the TPC, this difference could be expressed in number of
 746 σ (see Equation 6). In this way it is possible to estimate more quantitatively the goodness
 747 of a mass hypothesis. This also gives us the possibility to choose the strictness we want to
 748 adopt in the identification of a particle (n_σ , $n = 2, 3, 4$):

$$n_\sigma = \frac{(dE/dx)_{measured} - (dE/dx)_{Bethe-Bloch}}{\sigma_{TPC}} \quad (6)$$

V0

750 The VZERO detector [27] consists of two segmented arrays of plastic scintillator counters,
 751 called VZERO-A and VZERO-C, placed around the beam-pipe on either side of the IP:
 752 one at $Z = 340$ cm, covering the pseudo-rapidity range [2.8; 5.1], and the other at $Z = -90$
 753 cm (in front of the absorber), covering the pseudo-rapidity range [-3.7; -1.7]. They consist
 754 of 32 counters distributed in four rings, each divided in eight 45 sectors. Each counter
 755 is made of scintillator material embedded with WaveLength Shifting fibers. Clear fibers
 756 collect and transport the signal to photomultipliers 3 - 5 m far from the detector, inside
 757 the L3 magnet. The counters have a time resolution better than 1 ns. Their response is
 758 recorded in a time window of 25 ns around the nominal beam crossing time. The VZERO
 759 has an important role in rejecting background from beam-gas collisions (see, Figure 16)
 760 exploiting the relative time-of-flight measurement between the two arrays: when the beam-
 761 gas collision takes place outside the region between the two arrays, particles arrive 6 ns
 762 before or after the time of a beam-beam collision.

763 The VZERO is a trigger detector that will provide a minimum-bias trigger for all
 764 colliding systems to the central barrel detectors and three centrality triggers in p-Pb and
 765 Pb-Pb collisions (multiplicity, central and semi-central).

766 The first parameter to be determined in A-A(p-A) collisions is the centrality(multipliciy).
 767 This is defined according to the value of the impact parameter, b , and provides a geomet-
 768 rical scale of the overlapping region between the colliding nuclei: a collision will be defined
 769 from central to peripheral, as the impact parameter increases. The centrality of a collision
 770 is not directly available and must be deduced from a combination of experimentally mea-
 771 sured quantities and Monte Carlo simulations. There are a number of observables that can
 772 be measured and used as centrality estimators. The charged-particle multiplicity N_{ch} and
 773 the transverse energy E_T measured around mid-rapidity are measurable quantities related
 774 to the energy deposited in the interaction region (these are therefore related to N_{part}).
 775 These variables increase significantly increasing the centrality of the collisions. Another
 776 measurable quantity to estimate the centrality is the zero-degree energy EZDC, namely
 777 the energy carried by spectator nucleons $N_{spec} = 2A - N_{part} = E_{ZDC}/E_A$, where E_A is
 778 the beam energy per nucleon. Typically a measured distribution of one of the previous
 779 observables is mapped to the corresponding distribution obtained from phenomenological

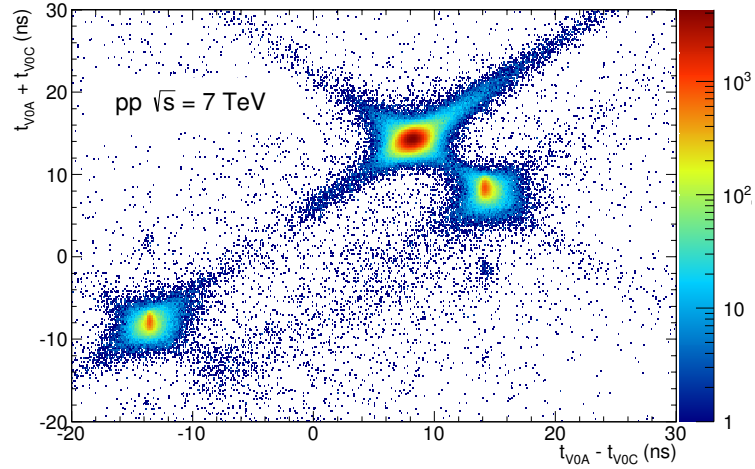


Figure 16: Correlation between the sum and difference of signal times in V0A and V0C. Three classes of events collisions at (8.3 ns, 14.3 ns), background from Beam 1 at (-14.3 ns, -8.3 ns), and background from Beam 2 at (14.3 ns, 8.3 ns) can be clearly distinguished.

Glauber calculations. The Glauber model [28, 29] uses a semi-classical approach: the A?A collision is assumed to be an incoherent superposition of N elementary nucleon- nucleon collisions. The main parameters of the model are the inelastic nucleon- nucleon collision cross-section σ_n and the nuclear density distribution $\rho(r)$. In practice, the simulated distribution well reproduce the measured distribution or the latter is fitted with an analytical function. The experimental distribution can then be divided in classes with sharp cuts on the measured observable (E_{ZDC} , E_T or N_{ch}). These "centrality" classes will correspond to well defined percentage of the integral of the distribution. A given centrality class in the measured distribution, corresponds to the same class in the simulated distribution, where the main geometrical variables (N_{part} , N_{coll} and T_{AA}) can be determined. The number of classes that can be defined depends on the resolution achievable on the selection variable. In the analysis described in this thesis the centrality(multiplicity) estimation is based on the measurement of the multiplicities from the VZERO scintillators [30][31]. This is the method that achieve the best centrality resolution: it ranges from 0.5% in central to 2% in peripheral collisions. Other methods, as the ones based on the E_{ZDC} measurement or based on the estimate of the number of tracks in the SPD or TPC, are used to asses a systematic uncertainty on the centrality determination. The distribution of the VZERO amplitudes is shown in Figure 17 where the centrality(multiplicity) percentiles are also indicated.

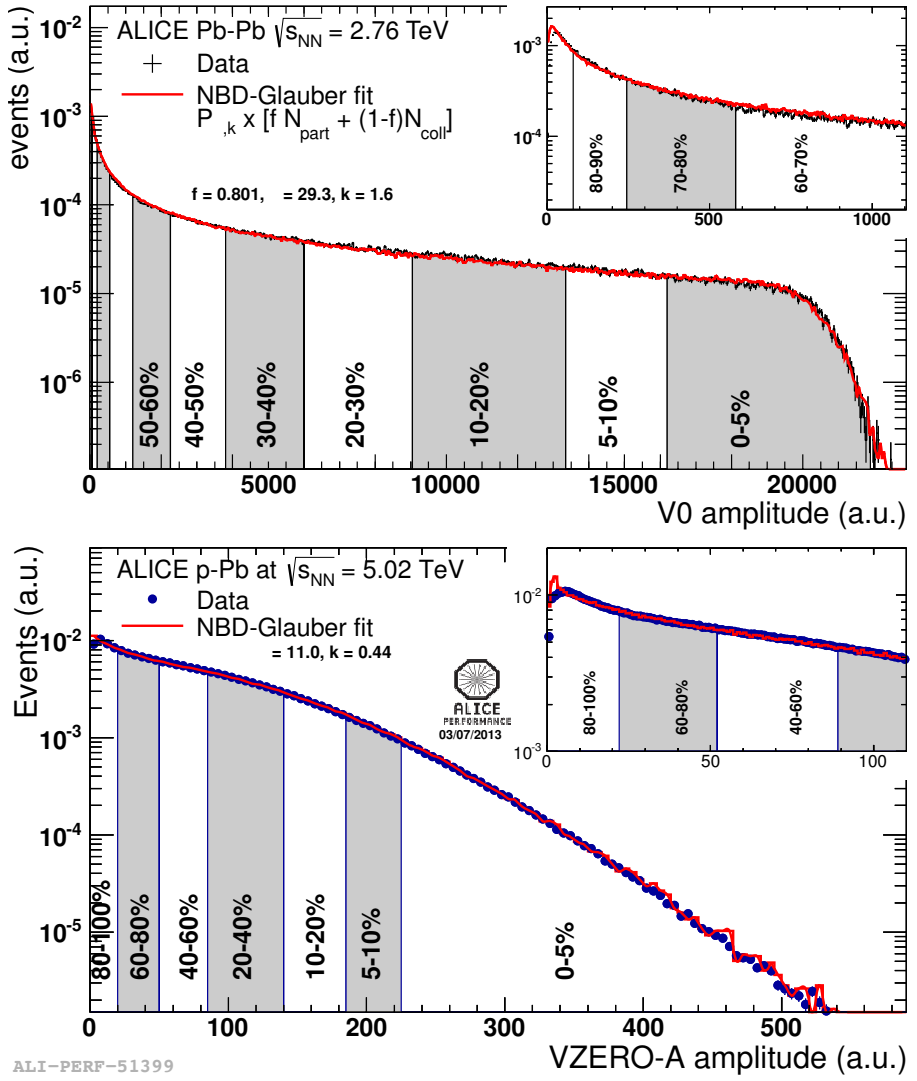


Figure 17: Distribution of the V0 amplitude (sum of V0A and V0C in top, V0A in bottom). The inset shows a magnified version of the most peripheral region.

799 **4.2.2 Data Acquisition (DAQ) and trigger system**

800 The architecture of data acquisition is shown in Figure 18. The tasks of the ALICE DAQ
 801 system are the assembly of event informations from individual detectors into complete
 802 events (event building) as well as buffer- ing and export of assembled events to permanent
 803 storage. The DAQ is designed to process a data rate up to 1.25 GB/s in heavy-ion runs.
 804 Event building is done in two steps. Data from the detectors is received by Detector Data
 805 Links (DDLs) on Local Data Concentrators (LDCs). The LDCs assemble the data into
 806 sub-events that are then shipped to Global Data Collectors (GDCs). A GDC re- ceives all
 807 sub-events from a given event and assembles them into a complete event. These events are
 808 subsequently stored on a system called Transient Data Storage (TDS).

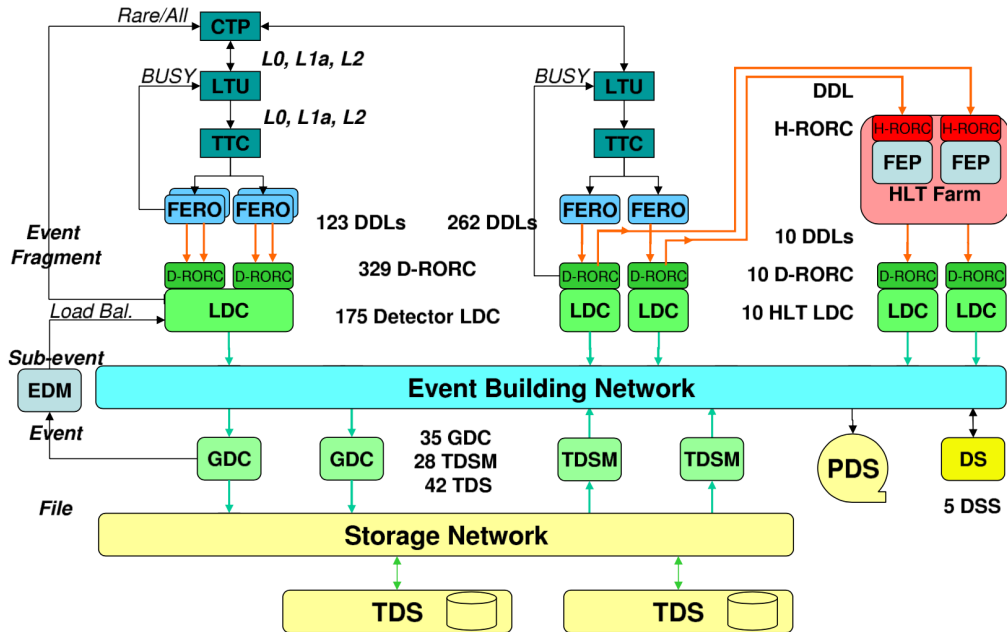


Figure 18: The overall architecture of the ALICE DAQ and the interface to the HLT system.

809 ALICE can simultaneously take data in several partitions, where a set of detec-
 810 tors can store their outputs. Since a partition is a group of commonly controlled detectors, a
 811 given detector can only be active in one partition at a time. The ac-
 812 tive detectors in a given partition may be assigned to data taking groups called clusters, for which triggers

813 can be defined. Therefore, upon a trigger only a sub-set of the whole partition may
814 be read out. Furthermore, a triggering detector does not have to be necessarily part of
815 the partition. ALICE has a two-layer trigger architecture [32]. The low-level trigger is a
816 hardware trigger called Central Trigger Processor (CTP). The High-Level Trigger (HLT)
817 is implemented as a pure software trigger. The CTP combines inputs from different trigger
818 sources, namely the various detectors. These inputs are single signals, like a hit in the
819 detector, or, can be the result of fast calculation performed directly in the detectors. The
820 HLT allows the implementation of sophisticated logic for the triggering. In contrast to the
821 CTP which governs the readout of the detectors, the HLT receives a copy of the data read
822 out from the detectors and processes them. The hardware trigger combines the trigger
823 signals of the various detectors to decide if an event is accepted, that means it is read out
824 and written to disk. Several trigger levels reduce the event rate depending on the input
825 signals. The first level, called L0, is delivered after 1.2 ?s, while the second, called L1,
826 after 6.5 ?s. The final trigger, L2, is delivered after 100 ?s, upon completion of the drift
827 time in the TPC. Only after an L2 trigger the event is finally stored. The rates of different
828 trigger classes are very different. By definition minimum-bias triggers have the highest
829 rate; other triggers that look for rare signals are characterized by much lower rates. In
830 order to cope with different scenarios, downscaling factors can be applied to the trigger
831 classes individually, i.e. only every nth event fulfilling the trigger condition is read out. The
832 total recording rate is limited by the maximum bandwidth of data that can be recorded
833 to disk and tape. The ALICE software trigger, called HLT, is a farm of multiprocessor
834 computers. The aim is to have about 1000 PCs processing the data in parallel allowing
835 an online analysis of the events. A trigger decision comes from the analysis of a more
836 comprehensive set of information than what happens for the hardware trigger, giving the
837 possibility to apply more sophisticated triggers. Examples include triggers on high energy
838 jets or on muon pairs. Furthermore, the HLT can significantly reduce the event size by
839 selecting regions of interest (partial readout of detectors) and by further compression of the
840 data. The HLT receives a copy of the raw data and performs per detector reconstruction,
841 partly aided by hardware coprocessors. Subsequently, the trigger decision is based on the
842 global reconstructed event. In the same step a region of interest can be selected. In the
843 last optional step, if the trigger decision is positive, the data are compressed. The trigger
844 decision, partial readout information, compressed data, and the re-construction output
845 is sent to LDCs and subsequently processed by the DAQ. In terms of the overall DAQ
846 architecture, data sent by HLT is treated like stemming from a detector.

847 **4.2.3 ALICE offline software frame work**

848 The required computing resources for the reconstruction and analysis of the raw data as
849 well as the production of simulated events needed for the understanding of the data exceed
850 the computing power of single institutes and even centers like CERN. Therefore, institutes
851 that are part of the Collaboration also provide storage and computing resources. Distribu-
852 tion of the data for reconstruction and analysis cannot be performed manually and this
853 led to the need for an automated system. The concept of a decentralized computing model
854 called Grid [33] was identified as a solution.

855

856 *The AliEn Framework*

857 The Grid paradigm implies the unification of resources of distributed computing center,
858 in particular computing power and storage, to provide them to users all over the World.
859 It allows computing center to offer their resources to a wider community and the local re-
860 sources to be shared by an entire collaboration. Software that implements the Grid concept
861 is called Grid middleware. ALICE has developed a Grid middleware called AliEn [34] since
862 2001. An ALICE user employs AliEn to connect to the ALICE Grid which is composed
863 of a combination of general services that are provided by many Grid middleware solutions
864 and ALICE-specific services provided by AliEn. Parts of the ALICE Grid are: i) a global
865 file catalog that is a directory of files in storage elements distributed over the Globe, ii)
866 the automatic matching of jobs for execution to a suitable location in one of the connected
867 sites, iii) a shell-like user interface and iv) API9 services for the ROOT framework [35].

868

869 *AliRoot Framework*

870 AliRoot [24] is the offline framework for simulation, alignment, calibration, reconstruction,
871 visualization, quality assurance, and analysis of experimental and simulated data. It is
872 based on the ROOT framework. Most of the code is written in C++ with some parts in
873 Fortran that are wrapped inside C++ code. Re-usability and modularity are the basic
874 features of the AliRoot framework. Modularity allows parts of the code to be replaced,
875 with minimum or no impact on the rest (for example changing the event generator, the
876 transport Monte Carlo or the reconstruction algorithms). This is achieved implementing
877 abstract interfaces. In addition codes for each detector subsystem are independent modules
878 with their specific code for simulation and reconstruction and the code can be developed
879 concurrently with minimum interference. Re-usability is meant to maintain a maximum
880 amount of backward compatibility as the system evolves.

881 The central module of the AliRoot framework is STEER (Figure 19) which provides
882 several common functions such as: steering of program execution for simulation, reconstruc-
883 tion and analysis; general run management, creation and destruction of data structures,
884 initialization and termination of program phases; base classes for simulation, event genera-
885 tion, reconstruction, detectors elements. For event simulation the framework provides the
886 following functionality:

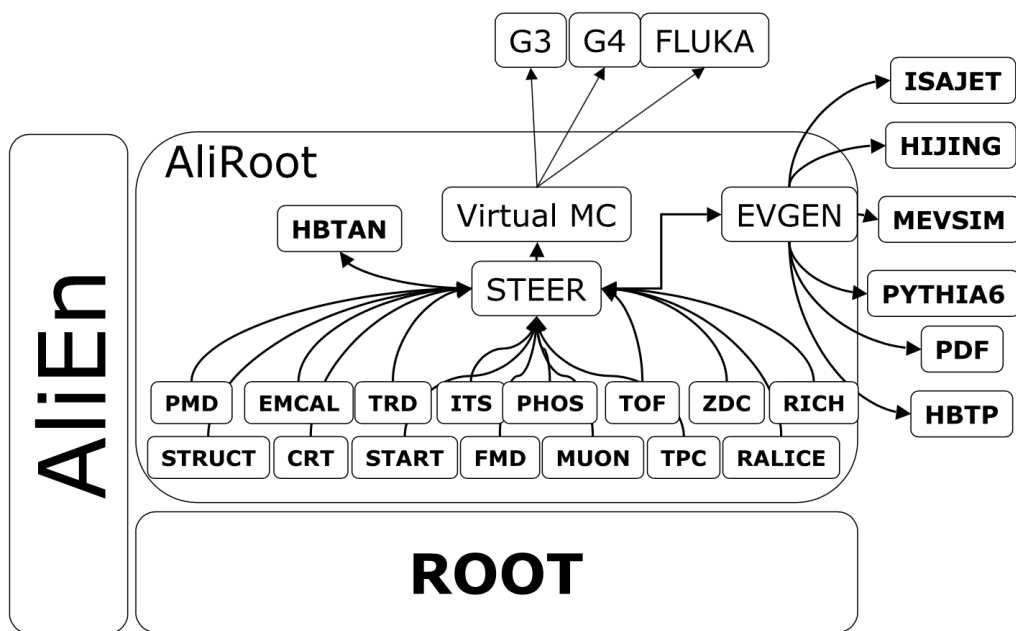


Figure 19: Schematic view of the AliRoot framework

887 **5 Measurement of $\Xi(1530)^0$ production in p–Pb and Pb–Pb**

888 The measurement of resonance production in p–Pb collisions helps to disentangle cold
889 nuclear matter effects from genuine hot medium effects and contribute to the study of
890 the system size dependence of re-scattering in the hadronic phase. And the measurement
891 in ultra-relativistic heavy-ion collisions such as Pb–Pb collisions, provide information on
892 the properties of hadronic medium and different stage of its evolution. In order to study
893 the particle production mechanism in the hadronic phase between the chemical and ki-
894 netic freeze-out, the $\Xi(1530)^0$ resonance production at mid-rapidity ($-0.5 < y_{\text{CMS}} < 0$) is
895 measured in p–Pb collisions $\sqrt{s_{\text{NN}}} = 5.02$ TeV and in Pb–Pb collisions with $|y| < 0.5$ at
896 $\sqrt{s_{\text{NN}}} = 2.76$ TeV with the ALICE experiment, via the reconstruction of its hadronic decay
897 into $\Xi\pi$.

898 **5.1 $\Xi(1530)^0$ -reconstruction**

899 The Ξ^{*0} production in p–Pb and Pb–Pb collisions at mid-rapidity has been studied in dif-
900 ferent multiplicity classes, from very central to peripheral collisions. The analysis strategy
901 is based on the invariant mass study of the reconstructed pairs (referred to as the candi-
902 dates) whose provenance could be the decay of a Ξ^{*0} baryon into charged particles. The
903 decay products (also called daughters in the text) are identified as oppositely charged Ξ and
904 π among the tracks reconstructed in the central barrel. The event selection, track selec-
905 tion and the particle identification strategy is described. The raw signal yield is extracted
906 by fitting the background-subtracted invariant mass distribution in several transverse mo-
907 mentum intervals. In order to extract the p_{T} -dependent cross section, these yields are
908 corrected for efficiency. The p_{T} -dependent correction due to the detector acceptance and
909 reconstruction efficiency, $(\text{Acc} \times \epsilon_{\text{rec}})(\text{pt})$, is computed from a Monte Carlo simulation.
910 The absolute normalisation is then performed, by dividing for the number of the events in
911 each multiplicity and centrality classes.

912 **5.1.1 Data sample and event selection**

913 A description of the ALICE detector and of its performance during the LHC Run 1 (2010–
914 2013) can be found in [24, 36]. The data sample in the analysis from Pb–Pb collisions with
915 energy of $\sqrt{s_{\text{NN}}} = 2.76$ obtained during 2011 and the sample of p–Pb run at $\sqrt{s_{\text{NN}}} = 5.02$
916 TeV was recorded in 2013.

917 Due to the asymmetric energies of the proton (4 TeV) and lead ion (1.57 A TeV) beams,
918 the centre-of-mass system in the nucleon-nucleon frame is shifted in rapidity by $\Delta y_{\text{NN}} =$
919 0.465 towards the direction of the proton beam with respect to the laboratory frame of
920 the ALICE detector [5]. For the analysed p–Pb data set, the direction of the proton beam
921 was towards the ALICE muon spectrometer, the so-called “C” side, standing for negative
922 rapidities; conversely, the Pb beam circulated towards positive rapidities, labelled as “A”

923 side in the following. The analysis in this paper was carried out at midrapidity, in the
924 rapidity window $-0.5 < y_{\text{CMS}} < 0$.

925 The minimum-bias trigger during the p–Pb run was configured to select events by
926 requiring a logical OR of signals in V0A and V0C [36], two arrays of 32 scintillator detectors
927 covering the full azimuthal angle in the pseudo-rapidity regions $2.8 < \eta_{\text{lab}} < 5.1$ and
928 $-3.7 < \eta_{\text{lab}} < -1.7$, respectively [37]. In the data analysis it was required to have a
929 coincidence of signals in both V0A and V0C in order to reduce the contamination from
930 single-diffractive and electromagnetic interactions. Out of this sample in p–Pb collision
931 events about 109.3 million events, 93.9 million events satisfy the following selection criteria
932 and have been actually used for the analysis.

933 The Pb–Pb collisions data sample was selected by online centrality trigger requiring a
934 signal in the forward V0 detectors[31] to record enhanced data in central collision. The
935 data consists of 24.8 million events in most central collisions (0-10%), 21.8 million events in
936 semi-central collisions (10-50%) and 3.5 million events with minimum-bas trigger (0-90%).
937 Among 49.6 million events in total, 43.0 million events have been analyzed as passed the
938 criteria below.

- 939 • Events with z-coordinate of primary vertex (V_z) falling within ± 10 cm from the
940 interaction point
- 941 • Rejection of pile-up event
- 942 • Requiring primary tracks to have at least one hit in one of the two innermost layers
943 of the ITS (silicon pixel detector, SPD)
- 944 • p–Pb: multiplicity ranges in percentile (V0A): 0-20%, 20-40%, 40-60%, 60-100% and
945 MB(0-100%)
- 946 • Pb–Pb: centrallity classes (V0A and V0C): 0-10%, 10-40%, 40-80% and MB (0-80%)

947 The distribution of the vertex z position of the accepted events in p–Pb collision is
948 reported on left panel in Figure 20 and corresponding figure but obtained from Pb–Pb
949 collisions is shown on right panel in Figure. 20. Events with $|V_z| < 10$ cm have been used
950 to ensure a uniform acceptance in the central pseudo-rapidity region, $|\eta| < 0.8$, where the
951 analysis is performed. This cut reduces the total number of events to 97.5 million events,
952 that is the $\sim 89.2\%$ of the initial sample in p–Pb collisions and 43.04 million events which
953 is $\sim 86.8\%$ of the initial sample in Pb–Pb collisions are survived.

954 Fig. 21 shows the multiplicity distribution of the accepted events in p–Pb collision
955 divided in bins of percentile. The each color on the histogram indicate the multiplicity
956 ranges used in this analysis. Corresponding events for each multiplicity range are in Table
957 6.

958 The distribution of centrality in each trigger used to select the events in Pb–Pb collision
959 is shown in Fig. 22 and the reason why the centrality has step structure is that there are

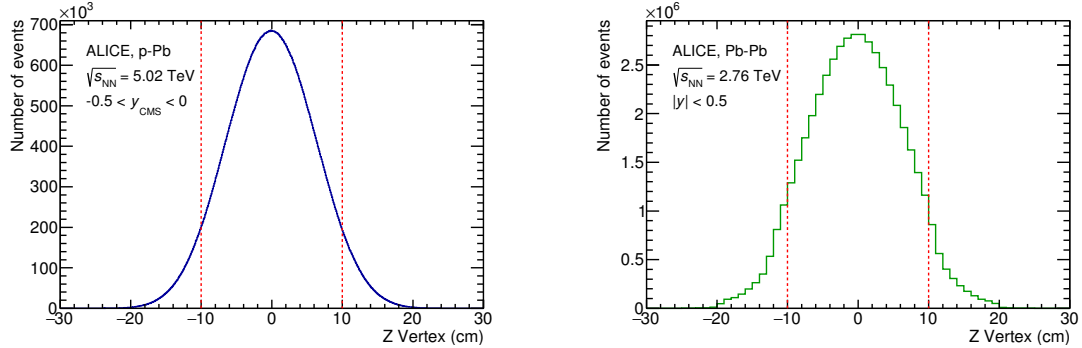


Figure 20: Vertex-z coordinate distribution of the accepted events in p–Pb collision(Left) and in Pb–Pb collisions(Right). The red dashed line indicates vertex cut

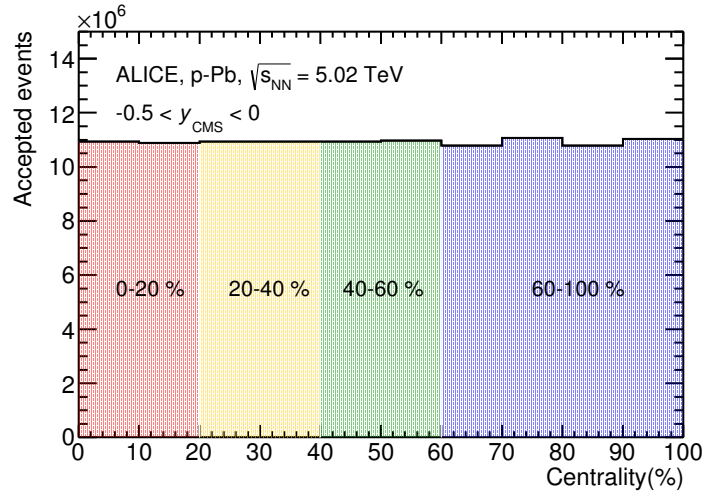


Figure 21: Multiplicity distribution of accepted events in p–Pb collision in percentile. The each color and labels define the four intervals in which the analysis is performed.

960 three different trigger classes classified by the amplitude threshold on VZERO detector.
961 Because the distribution of events as function of centrality is not a flat, this may lead to
962 additional bias, in particular when one needs to combine the results from different triggers.
963 For example, events from 40-80% centrality bin have bias with high statistics in 40-60%. In
964 order to avoid this effect, we have applied a flattening procedure to have flat distribution
965 of events as function of centrality. A brief explanation of the method is below :

- 966 1. Histograms are obtained for the effective mass distribution in 1% centrality bins and
967 for the centrality distribution
968 2. The effective mass distributions are scaled in each 1% centrality bin by a factor:
969 Factor = Nevent in 20-40% / 20 / Nevent in current 1% bin
970 3. Each bin in the centrality distribution is scaled using the factor described above
971 4. Histograms are added for centrality bins of interest: 0-10%, 10-40%, 40-80%, 0-80%

972 The resulting number of events in each centrality classes is summarized in Table 6.

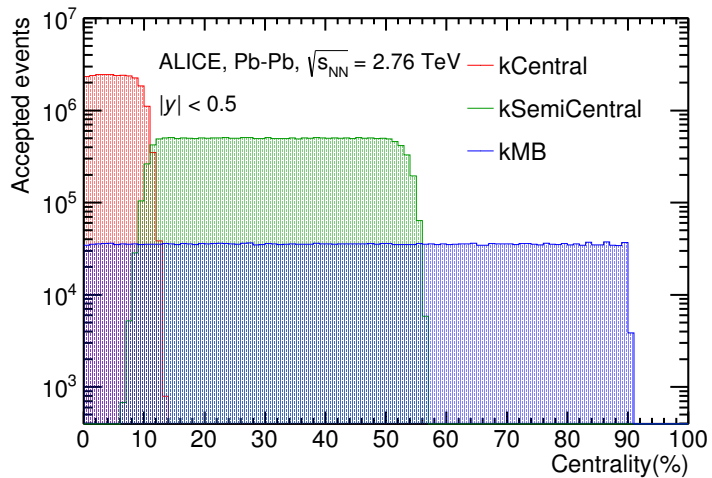


Figure 22: Centrality distribution of three different trigger classes.

p-Pb	0-20%	21.82×10^6
	20-40%	21.86×10^6
	40-60%	21.91×10^6
	60-100%	43.68×10^6
Pb-Pb	0-10%	5.58×10^6
	10-40%	16.73×10^6
	40-80%	22.31×10^6

Table 6: Number of accepted and analyzed events per multiplicity/centrality interval

5.1.2 Track and topological selection

In comparison with the Ξ^{*0} analysis carried out in pp collisions at $\sqrt{s} = 7$ TeV [7], track and topological selections were revised and adapted to the p-Pb dataset. Pions from strong decays of Ξ^{*0} were selected according to the criteria for primary tracks. As summarized in Table 7, all charged tracks were selected with $p_T > 0.15$ GeV/c and $|\eta_{\text{lab}}| < 0.8$, as described in Ref. [36]. The primary tracks were chosen with the Distance of Closest Approach (DCA) to PV of less than 2 cm along the longitudinal direction (DCA_z) and lower than $7\sigma_r$ in the transverse plane (DCA_r), where σ_r is the resolution of DCA_r . The σ_r is strongly p_T -dependent and lower than 100 μm for $p_T > 0.5$ GeV/c [36]. To ensure a good track reconstruction quality, candidate tracks were required to have at least one hit in one of the two innermost layers (SPD) of the ITS and to have at least 70 reconstructed points in the Time Projection Chamber (TPC), out of a maximum of 159. The Particle IDentification (PID) criteria for all decay daughters are based on the requirement that the specific energy loss (dE/dx) is measured in the TPC within three standard deviations (σ_{TPC}) from the expected value (dE/dx_{exp}), computed using a Bethe-Bloch parametrization [36].

Common track selections	$ \eta_{\text{lab}} $	< 0.8
	p_T	> 0.15 GeV/c
	PID $ (\text{d}E/\text{d}x) - (\text{d}E/\text{d}x)_{\text{exp}} $	$< 3 \sigma_{\text{TPC}}$
Primary track selections	DCA_z to PV	< 2 cm
	DCA_r to PV	$< 7\sigma_r$ - $10\sigma_r$ (p_T)
	number of SPD points	≥ 1
	number of TPC points	> 70
	χ^2 per cluster	< 4

Table 7: Track selections common to all decay daughters and primary track selections applied to the charged pions from decays of Ξ^{*0} .

Since pions and protons from weak decay of Λ ($c\tau = 7.89$ cm [1]) and pions from weak decay of Ξ^- ($c\tau = 4.91$ cm [1]) are produced away from the PV, specific topological and

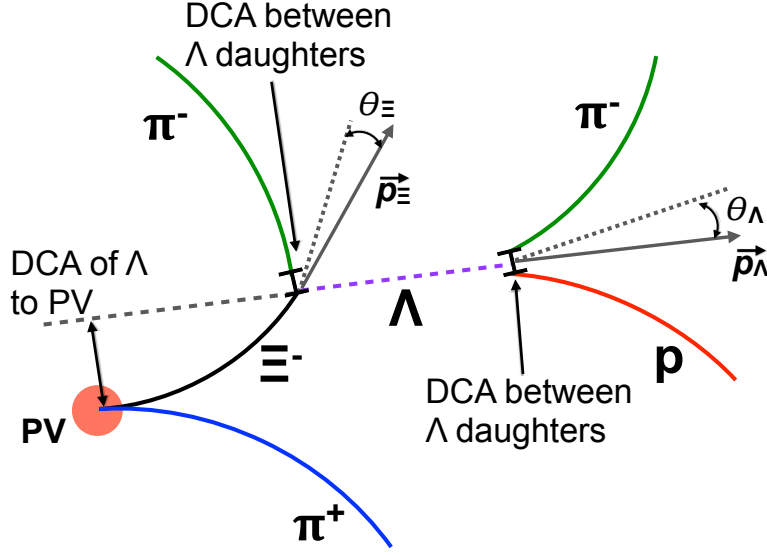


Figure 23: Sketch of the decay modes for Ξ^{*0} and depiction of the track and topological selection criteria.

990 track selection criteria, as summarized in Table 8, were applied [6, 7, 38].

Topological cuts	p-Pb	Pb-Pb
DCA _r of Λ decay products to PV	> 0.06 cm	> 0.11 cm
DCA between Λ decay products	< 1.4 cm	< 0.95 cm
DCA of Λ to PV	> 0.015 cm	> 0.06
$\cos\theta_\Lambda$	> 0.875	> 0.998
$r(\Lambda)$	$0.2 < r(\Lambda) < 100$ cm	$0.2 < r(\Lambda) < 100$ cm
$ M_{p\pi} - m_\Lambda $	$< 7 \text{ MeV}/c^2$	$< 7 \text{ MeV}/c^2$
DCA _r of pion (from Ξ^-) to PV	> 0.015 cm	> 0.035 cm
DCA between Ξ^- decay products	< 1.9 cm	< 0.275
$\cos\theta_\Xi$	> 0.981	> 0.9992
$r(\Xi^-)$	$0.2 < r(\Xi^-) < 100$ cm	$0.2 < r(\Xi^-) < 100$ cm
$ M_{\Lambda\pi} - m_\Xi $	$< 7 \text{ MeV}/c^2$	$< 7 \text{ MeV}/c^2$

Table 8: Topological and track selection criteria.

991 In the analysis of Ξ^{*0} , Λ and π from Ξ^- were selected with a DCA of less than 1.9 cm
992 and with a DCA_r to the PV greater than 0.015 cm. The Λ daughter particles (π and p)

⁹⁹³ were required to have a DCA_r to the PV greater than 0.06 cm, while the DCA between the
⁹⁹⁴ two particles was required to be less than 1.4 cm. Cuts on the invariant mass, the cosine
⁹⁹⁵ of the pointing angle ($\theta_\Lambda, \theta_\Xi$) and the radius of the fiducial volume ($r(\Lambda), r(\Xi)$) in Table 8
⁹⁹⁶ were applied to optimize the balance of purity and efficiency of each particle sample.

997 **5.1.3 Particle identification**

998 PID selection criteria are applied for

- 999 1. π^\pm (last emitted π) and proton from Λ
1000 2. π^\pm (second emitted π) from Ξ^\pm
1001 3. π^\pm (first emitted π) from $\Xi(1530)^0$

1002 by using TPC. On TPC dE/dx versus momentum distribution, 3σ cuts are applied to TPC
1003 for selecting each of the particles. The TPC dE/dx selection allows to have better signal
1004 with $\sim 20\%$ increase of significance.

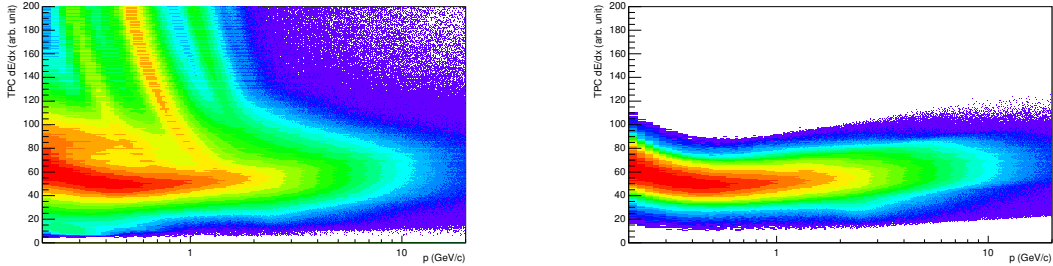


Figure 24: TPC dE/dx as function of transverse momentum for total (top) and selected first emitted π in 3σ (bottom)

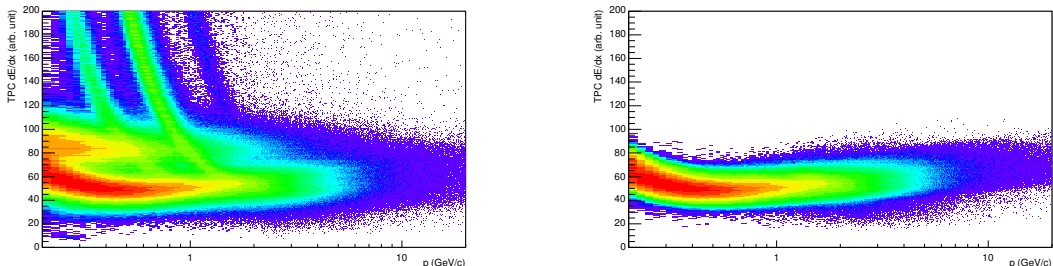


Figure 25: TPC dE/dx as function of transverse momentum for total (top) and selected second emitted π in 3σ (bottom)

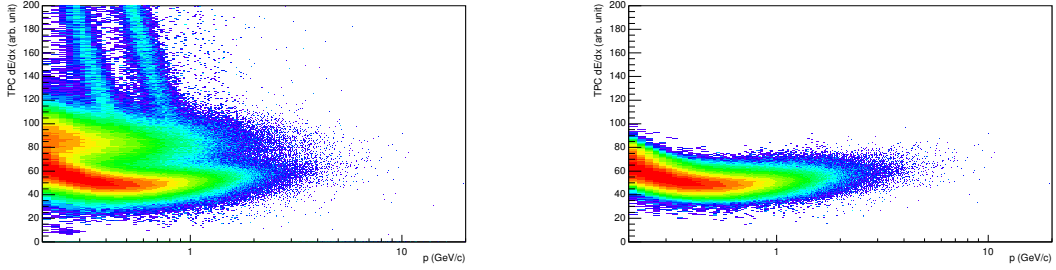


Figure 26: TPC dE/dx as function of transverse momentum for total (top) and selected last emitted π in 3σ (bottom)

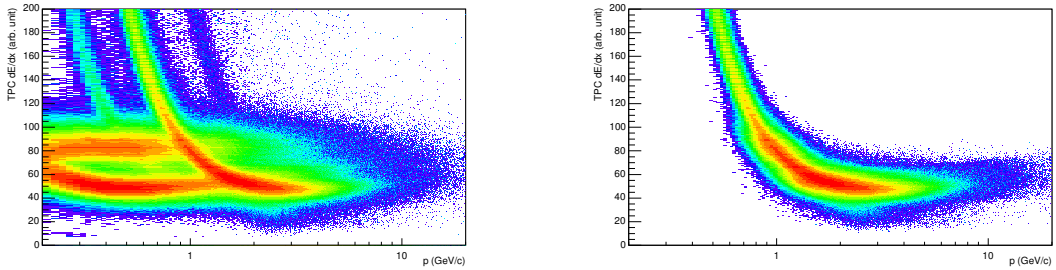


Figure 27: TPC dE/dx as function of transverse momentum for total (top) and selected proton in 3σ (bottom)

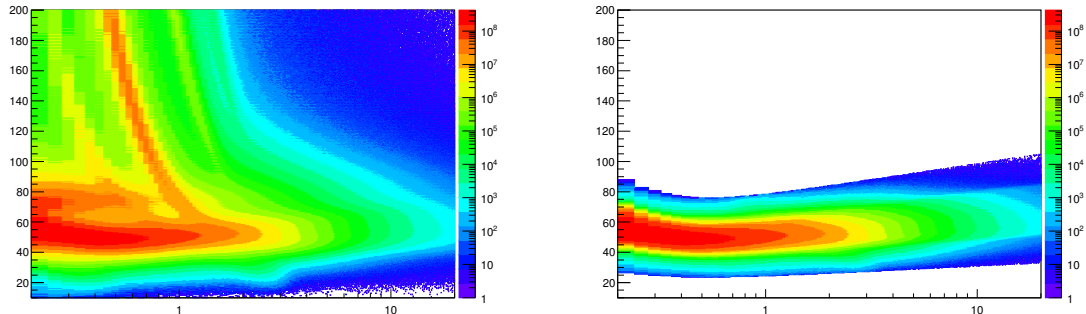


Figure 28: TPC dE/dx as function of transverse momentum for total (top) and selected first emitted π in 3σ (bottom)

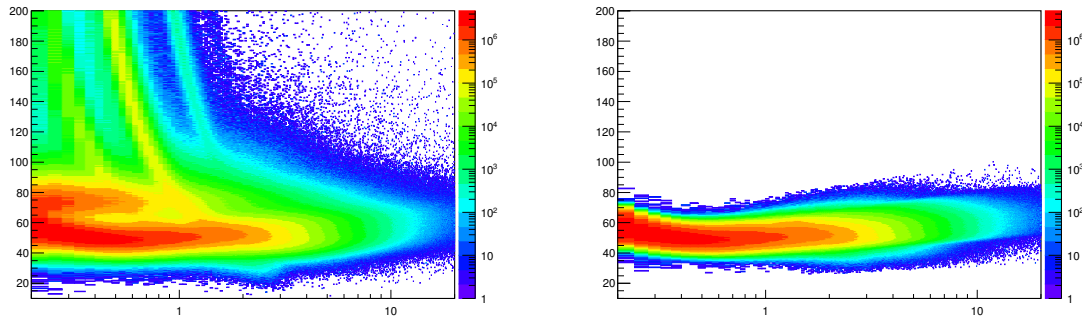


Figure 29: TPC dE/dx as function of transverse momentum for total (top) and selected second emitted π in 3σ (bottom)

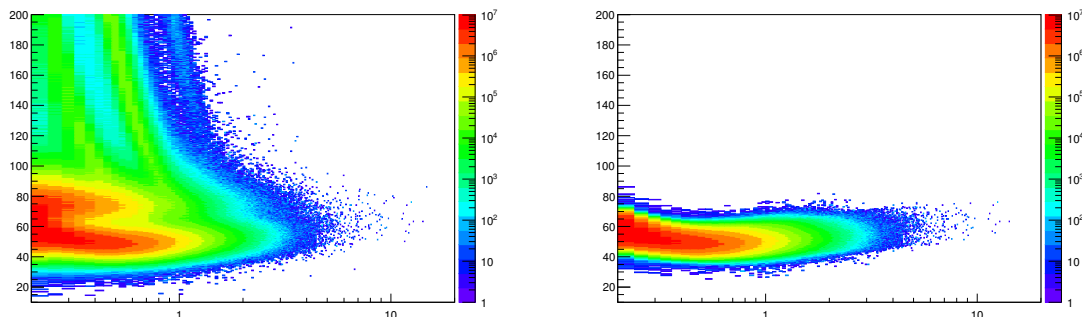


Figure 30: TPC dE/dx as function of transverse momentum for total (top) and selected last emitted π in 3σ (bottom)

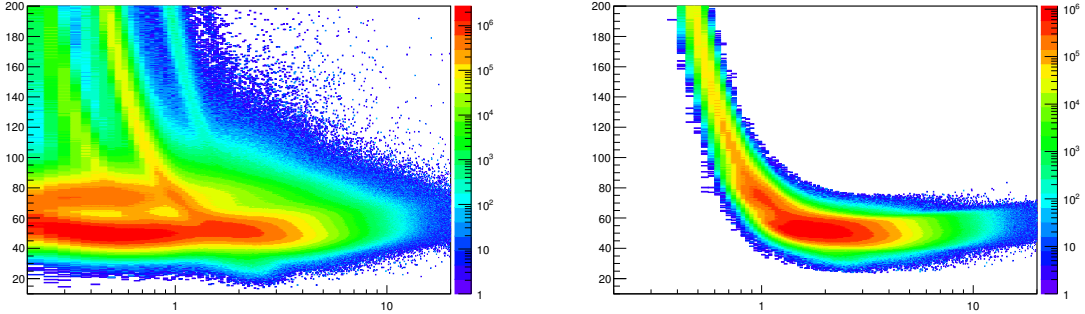


Figure 31: TPC dE/dx as function of transverse momentum for total (top) and selected proton in 3σ (bottom)

1005 5.1.4 Signal extraction

1006 The Ξ^{*0} signals were reconstructed by invariant-mass analysis of candidates for the decay
 1007 products in each transverse momentum interval of the resonance particle, and for each
 1008 multiplicity class. The $\Xi^-\pi^+(\Xi^+\pi^-)$ invariant mass distribution is reported in Figure 5.1.4
 1009 for semi-central events (20-40%) in p–Pb collisions and Figure 5.1.4 for central events(0-
 1010 10%) in Pb–Pb collisions.

1011 Since the resonance decay products originate from a position which is indistinguishable
 1012 from the PV, a significant combinatorial background is present. In order to extract
 1013 $\Xi(1530)^0$ signal it is necessary to remove or, at least reduce, the combinatorial background.
 1014 For this analysis, this has been done with the event mixing (EM) technique, by combining
 1015 uncorrelated decay products 20 different events in p–Pb (5 different events in Pb–Pb). The
 1016 events for the mixing have been selected by applying the similarity criteria to minimise
 1017 distortions due to different acceptances and to ensure a similar event structure, only tracks
 1018 from events with similar vertex positions z ($|\Delta z| < 1$ cm) and track multiplicities n ($|\Delta n| <$
 1019 10) were taken.

1020 The mixed-event background distributions were normalised to two fixed regions,
 1021 $1.49 < M_{\Xi\pi} < 1.51 \text{ GeV}/c^2$ and $1.56 < M_{\Xi\pi} < 1.58 \text{ GeV}/c^2$, around the Ξ^{*0} mass
 1022 peak (Figure 5.1.4 and 5.1.4). These regions were used for all p_T intervals and multiplicity
 1023 classes, because the background shape is reasonably well reproduced in these regions and
 1024 the invariant-mass resolution of the reconstructed peaks appears stable, independently of
 1025 p_T . The uncertainty on the normalisation was estimated by varying the normalisation
 1026 regions and is included in the quoted systematic uncertainty for the signal extraction (Section 5.4).

1028 After the background subtraction, the resulting distribution is shown in Figure 5.1.4
 1029 and 5.1.4. In order to obtain raw yields, a combined fit of a first-order polynomial for

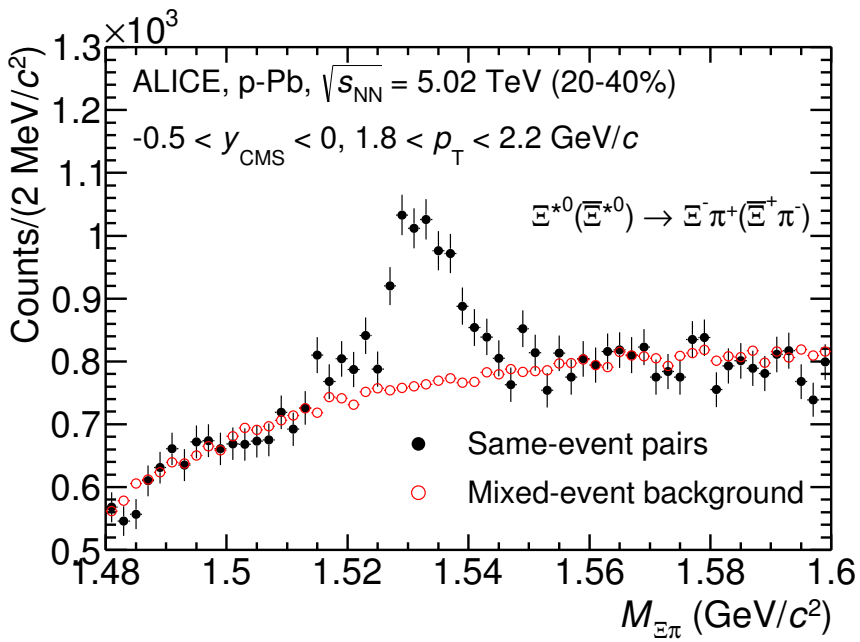


Figure 32: The $\Xi^\pm\pi^\pm$ invariant mass distribution (Same-event pairs) in $1.8 < p_T < 2.2 \text{ GeV}/c$ and for the multiplicity class 20-40%. The background shape, using pairs from different events (Mixed-event background), is normalised to the counts in $1.49 < M_{\Xi\pi} < 1.51 \text{ GeV}/c^2$ and $1.56 < M_{\Xi\pi} < 1.58 \text{ GeV}/c^2$.

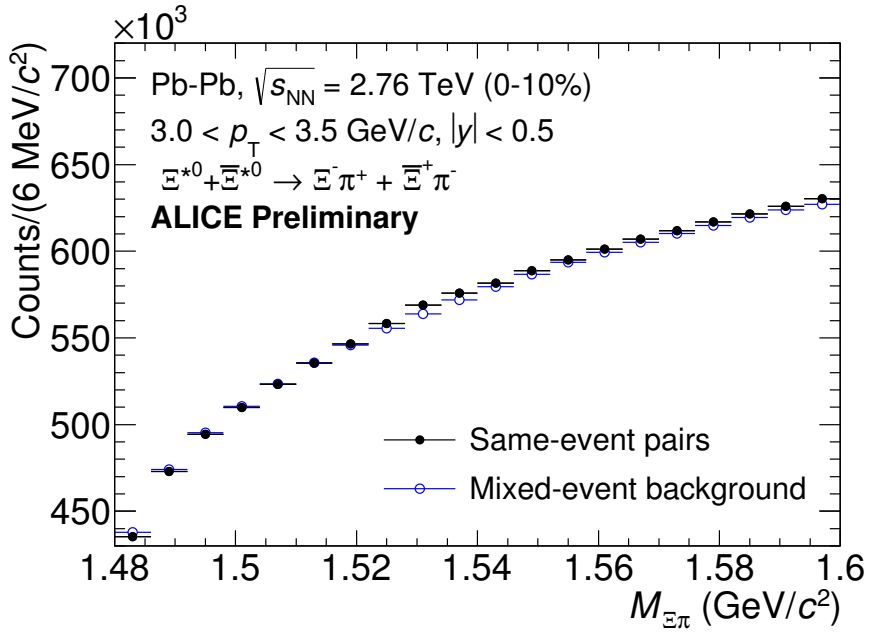


Figure 33: The $\Xi^\pm\pi^\pm$ invariant mass distribution (Same-event pairs) in $3.0 < p_T < 3.5$ GeV/c and for the centrality class 0-10%. The background shape, using pairs from different events (Mixed-event background), is normalised to the counts in $1.49 < M_{\Xi\pi} < 1.51$ GeV/c² and $1.56 < M_{\Xi\pi} < 1.58$ GeV/c².

1030 the residual background and a Voigtian function (a convolution of a Breit-Wigner and a
 1031 Gaussian function accounting for the detector resolution) for the signal was used. The
 1032 mathematical form of fit function used in analysis is:

$$f(M_{\Xi\pi}) = \frac{Y}{2\pi} \frac{\Gamma_0}{(M_{\Xi\pi} - M_0)^2 + \frac{\Gamma_0^2}{4}} \frac{e^{-(M_{\Xi\pi} - M_0)/2\sigma^2}}{\sigma\sqrt{2\pi}} + bg(M_{\Xi\pi}) \quad (7)$$

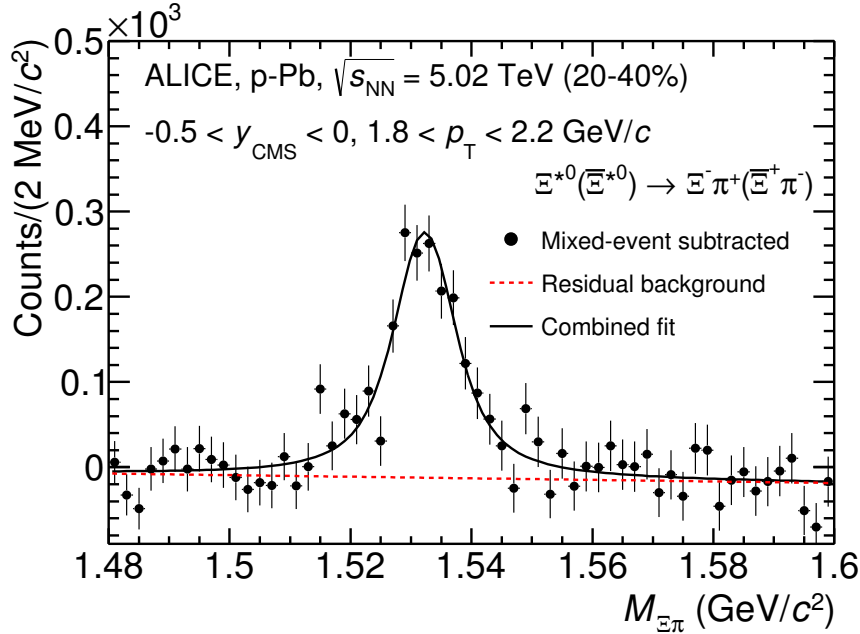


Figure 34: The invariant mass distribution after subtraction of the mixed-event background in p–Pb collisions. The solid curve represents the combined fit, while the dashed line describes the residual background.

1033 The mass parameter of the Voigtian fit (M_0) is left free within the fit range ($1.48 \text{ GeV}/c^2$
 1034 and $1.59 \text{ GeV}/c^2$). The overall invariant mass width of the Voigtian function is governed
 1035 by 2 parameters: σ and Γ_0 . The σ describes the broadening of the peak due to finite
 1036 detector resolution while Γ describes the intrinsic width of the resonance itself. The Γ_0 is
 1037 fixed to the PDG value of $9.1 \text{ MeV}/c$ for the $\Xi(1530)^0$. Because of lack of statistics, the
 1038 σ can be over estimated. Therefore the σ parameter is fixed to value derived from σ in
 1039 MB events which has largest statistics. The σ as function of p_T distribution in MB events
 1040 is shown in Figure. 36 and we also report invariant mass of $\Xi(1530)^0$ as function of p_T in
 1041 Figure. 37. The $\Xi(1530)^0$ raw yields have been extracted from the fit for the 4 multiplicity

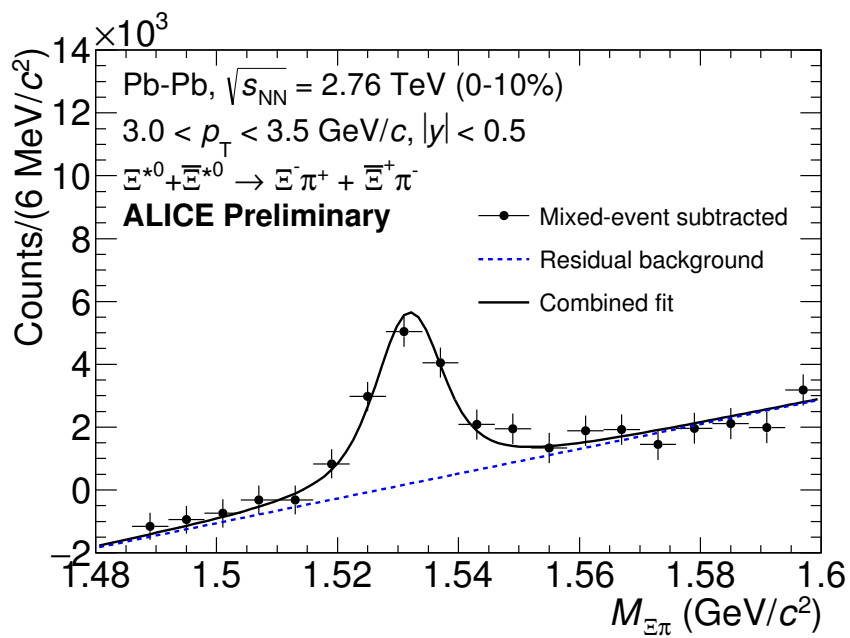


Figure 35: The invariant mass distribution after subtraction of the mixed-event background in Pb–Pb collisions. The solid curve represents the combined fit, while the dashed line describes the residual background.

¹⁰⁴² bins (+ NSD events) in p–Pb and 4 centrality bins in Pb–Pb collisions and the yields as
¹⁰⁴³ function of p_T are shown in Figure 38.

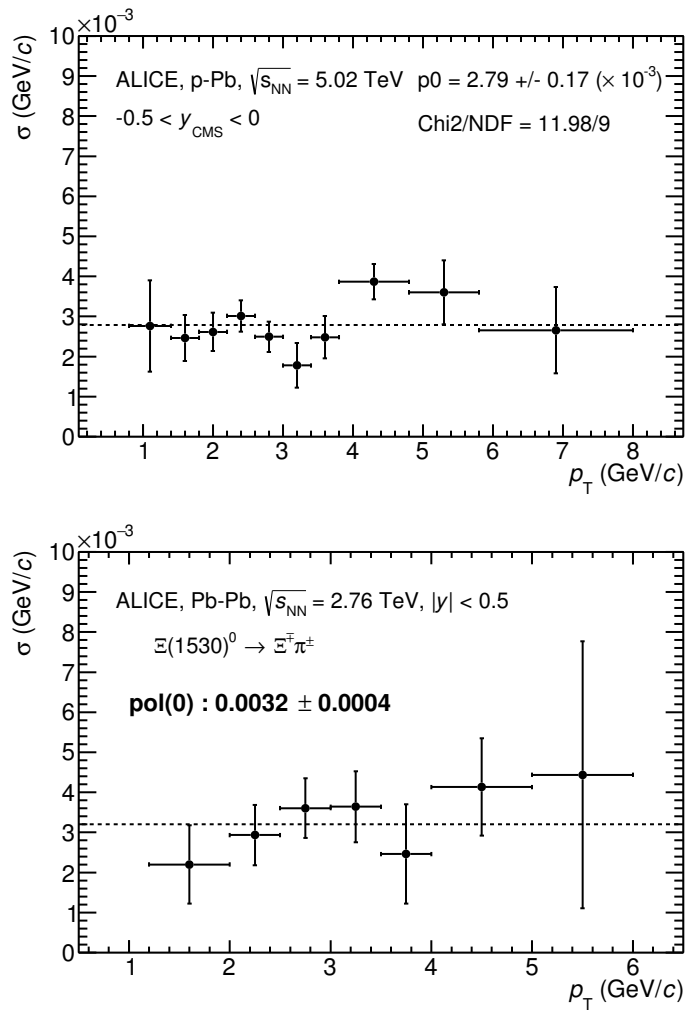


Figure 36: σ fit parameters as a function of p_T in MB in p–Pb collisions (top) and in Pb–Pb collisions (bottom).

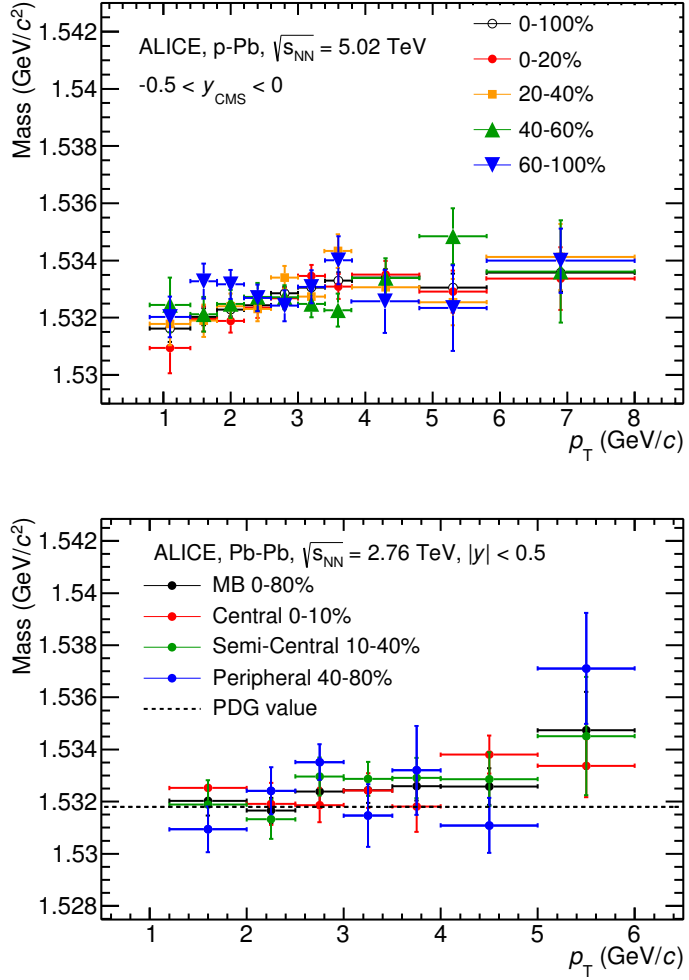


Figure 37: $\Xi(1530)^0$ -mass obtained from fit of the Voigtian peak as a function of p_T in each multiplicity classes in p-Pb collisions (top) and the different centrality classes in Pb-Pb (bottom).

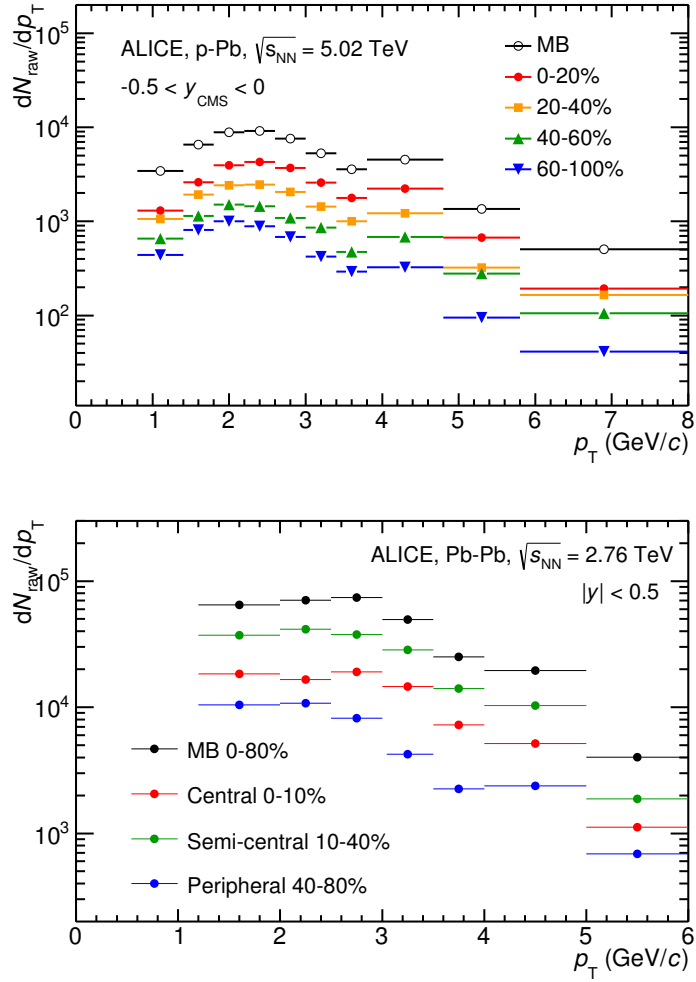


Figure 38: $\Xi(1530)^0$ -raw spectra obtained from fit of the Voigtian peak and a polynomial residual background for different multiplicities in p-Pb collisions (top) and Pb-Pb collisions (bottom). Only the statistical error is reported.

1044 **5.2 Efficiency correction**

1045 The raw yields were corrected for the geometrical acceptance and the reconstruction effi-
 1046 ciency ($A \times \epsilon$) of the detector (Figure. 39). By using the DPMJET 3.05 event generator [39]
 1047 and the GEANT 3.21 package [40], a sample of about 100 million p–Pb events was sim-
 1048 ulated and reconstructed in order to compute the corrections. The distributions of $A \times \epsilon$
 1049 were obtained from the ratio between the number of reconstructed Ξ^{*0} and the number of
 1050 generated particle in the same p_T and rapidity interval. Since the correction factors for
 1051 different multiplicity classes are in agreement with those from MB events within statistical
 1052 uncertainty, the latter were used for all multiplicity classes.

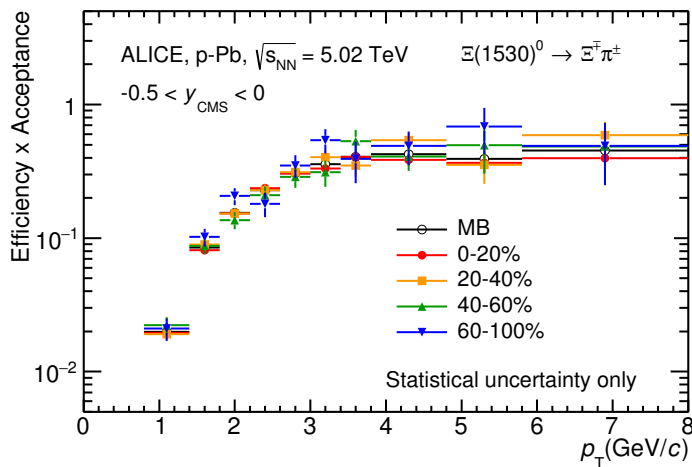


Figure 39: $\Xi(1530)^0$ -raw spectra obtained from fit of the Voigtian peak and a polynomial residual background for different multiplicities. Only the statistical error is reported.

1053 Because the generated $\Xi(1530)^0$ spectra have different shapes than the measured $\Xi(1530)^0$
 1054 spectra, it is necessary to weight the generated and reconstructed $\Xi(1530)^0$ spectra in these
 1055 simulations. Fig. 40 shows the generated and reconstructed $\Xi(1530)^0$ spectra plotted with
 1056 the (corrected) measured $\Xi(1530)^0$ spectrum for MB events and the Levy fit of that mea-
 1057 sured spectrum. The generated and measured $\Xi(1530)^0$ spectra have different behaviours
 1058 for the range $0.5 < p_T < 1$ GeV/ c . The generated $\Xi(1530)^0$ spectrum decreases with
 1059 increasing p_T over this range, while the fit of the measured $\Xi(1530)^0$ spectrum reaches a
 1060 local maximum in this range. The correction ϵ is observed to change rapidly over this
 1061 p_T range. It is therefore necessary to weight the generated spectrum so that it has the
 1062 shape of the measured $\Xi(1530)^0$ spectrum (and to apply corresponding weights to the re-
 1063 constructed $\Xi(1530)^0$ spectrum). An iterative procedure is performed to determine the
 1064 correct weighting (and therefore the correct ϵ).

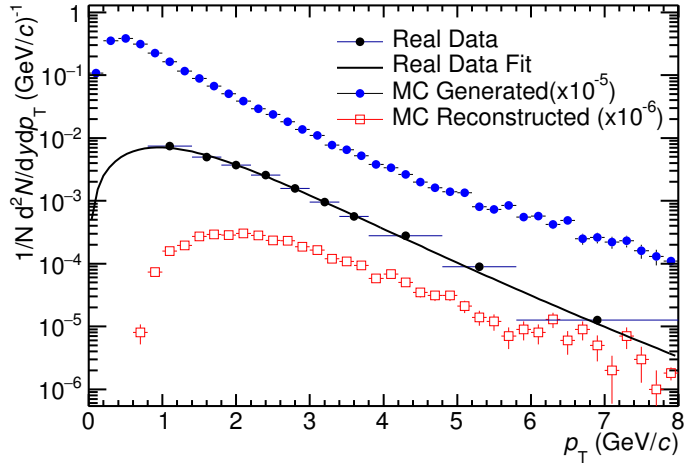


Figure 40: Real corrected $\Xi(1530)^0$ spectrum (black) for the minimum bias with Levy fit (black curve). Also shown are the unweighted generated (blue) and reconstructed (red) $\Xi(1530)^0$ spectra.

- 1065 1. The unweighted ϵ is calculated.
- 1066 2. This ϵ is used to correct the measured xis spectrum.
- 1067 3. The corrected $\Xi(1530)^0$ spectrum is fit.
- 1068 4. This fit is used to weight the simulated xis spectra. A p_T dependent weight is applied
1069 to the generated xis spectrum so that it follows the fit. The same weight is applied
1070 to the reconstructed xis spectrum.
- 1071 5. The (weighted) ϵ is calculated.
- 1072 6. Steps 2-5 are repeated (with the weighted ϵ from step 5 used as the input for step 2)
1073 until the ϵ values are observed to change by $< 0.1\%$ (relative) between iterations. It
1074 is observed that four iterations are sufficient for this procedure to converge.

1075 Finally, the re-weighted efficiency is obtained and the distribution as function of p_T is
1076 shown in Figure 41.

1077 In order to obtain the correction factor dedicated in Pb-Pb collisions, MC events are
1078 generated using Heavy Ion Jet Interaction Generator (HIJING). The generated events are
1079 passed through a GEANT3 model of the ALICE experiment with a realistic description of
1080 the detector response. Because we have observed centrality dependent efficiency, the cen-
1081 trality dependent efficiencies have been applied to get corrected raw yield. The reweighting

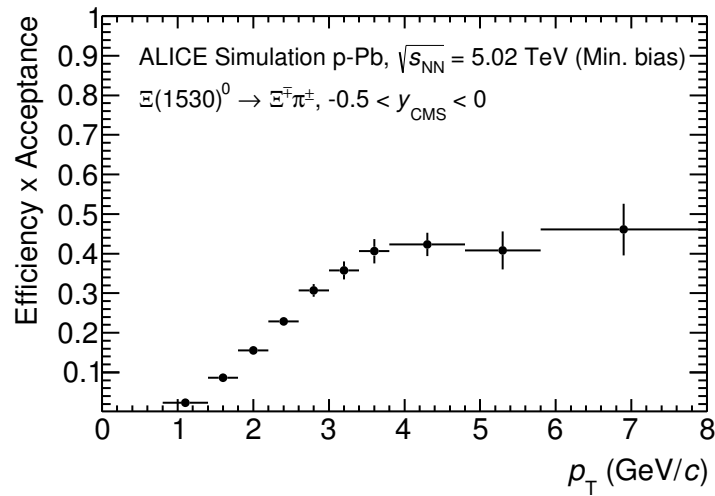


Figure 41: Efficiency as a function of p_T in minimum bias events in p–Pb collisions.

1082 approach which was used to correct the efficiency in p–Pb is also applied to the efficiency
 1083 obtained in Pb–Pb.

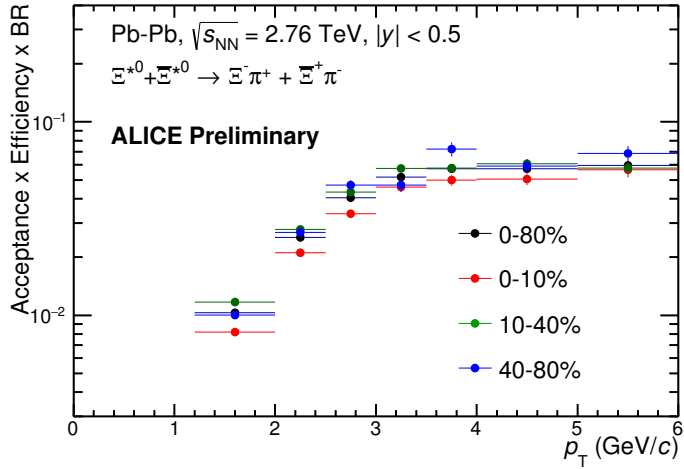


Figure 42: Efficiency as a function of p_T in different centrality classes in Pb–Pb collisions

1084 5.3 Corrected p_T -spectra

1085 The p_T spectrum is by the number of produced particles of a given type in the desired
 1086 interval of phase-space divided by the number of inelastic collisions. The spectrum is
 1087 calculated as:

$$\frac{1}{N} \times \frac{d^2N}{dydp_T} = \frac{1}{N_{E,PhysSel}} \times \frac{N_{raw}}{dp_T dy} \epsilon \frac{N_{total}^{MC}}{N_{post-PVcut}^{MC}}, \quad (8)$$

1088 where N_E represent the number inelastic collisions, the $\frac{dN}{dydp_T}$ is the yield per range of
 1089 rapidity y , per range in p_T . On the right hand side $N_{E,PhysSel}$ is the number of events
 1090 counted by the physics selection trigger. N_{raw} is the raw extracted number of particle in the
 1091 rapidity and p_T bin of width $\Delta y = 0.5$ in p–Pb ($\Delta y = 1.0$ in Pb–Pb) and Δp_T , respectively.
 1092 ϵ is the reconstruction efficiency estimated from Monte Carlo simulations. $\frac{N_{total}^{MC}}{N_{post-PVcut}^{MC}}$ is the
 1093 ratio of the total number of particle from MC divided by the number of particle from MC
 1094 after the Primary-Vertex cut is imposed. It takes into account the fraction of particle lost
 1095 after imposing the PV cut. We notice that for minimum-bias results in p–Pb, we adopted
 1096 a normalisation such that to provide result from non-single diffractive(NSD) cross-section.
 1097 The normalisation factor is 0.964 [5]. The obtained spectrum at MB and the spectrums
 1098 from different multiplicity classes in p–Pb are shown in Figure 43 and different centrality
 1099 classes in Pb–Pb are shown in Figure 44.

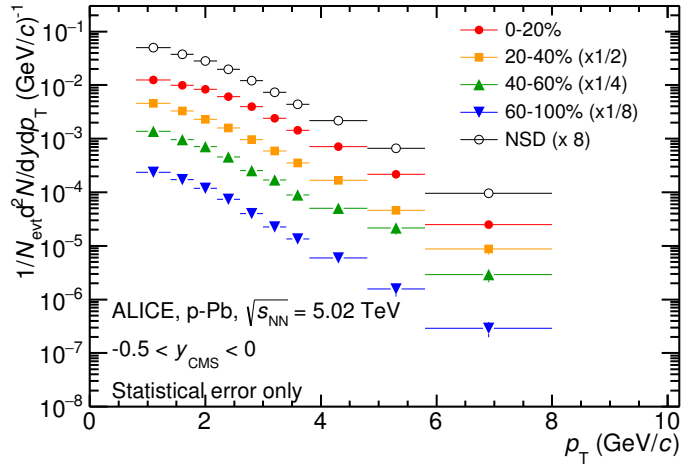


Figure 43: Corrected p_T -spectra of $\Xi(1530)^0$ in NSD and different multiplicity classes in p-Pb collisions.

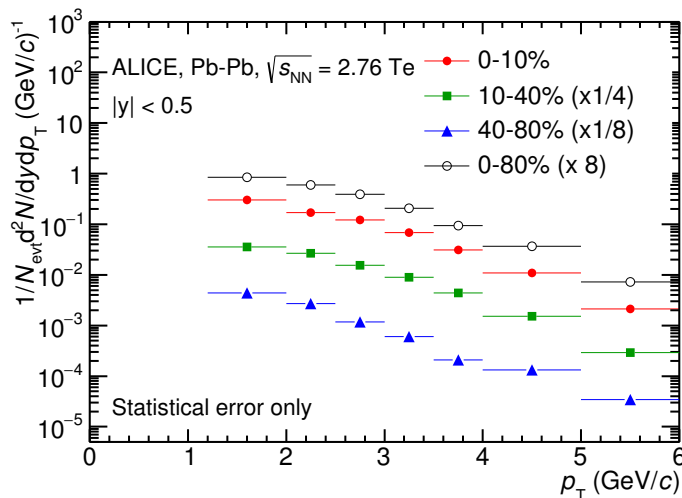


Figure 44: Corrected p_T -spectra of $\Xi(1530)^0$ in different centrality classes in Pb-Pb collisions.

1100 5.4 Systematic uncertainties

1101 The systematic uncertainties are calculated in seven principle groups. The procedure to ob-
1102 tain the systematic uncertainties is performed many times by varying the possible permuta-
1103 tion of the analysis parameter. The general strategy for evaluating systematic uncertainties
1104 is described as following:

- 1105 1. Choose one set of parameters for the analysis as default
- 1106 2. Observe the deviation of yield when one parameter is changed
- 1107 3. The systematic uncertainty is calculated for a given source as the RMS deviation of
1108 the available sources.
- 1109 4. The total systematic uncertainty, taking into account all the different sources, is the
1110 sum in quadrature of each source.

1111 To study the systematic effect we repeat the measurement by varying one parameter at
1112 a time. A Barlow [41] check has been performed for each measurement to verify whether it
1113 is due to a systematic effect or a statistical fluctuation. Let each measurement be indicated
1114 by $(y_i \pm \sigma_i)$ and the central value (default measurement) by $(y_c \pm \sigma_c)$, one can define $\Delta\sigma_i$
1115 (Eq. 9).

$$\Delta\sigma_i = \sqrt{(|\sigma_i^2 - \sigma_c^2|)} \quad (9)$$

1116 Then we calculate $n_i = \Delta y_i / \Delta\sigma_i$, where $\Delta y_i = |y_c - y_i|$. If $n_i \leq 1.0$ then the effects
1117 are due to the statistical fluctuation and if $n_i > 1.0$ we apply consistency check. Since
1118 the alternate and default measurements are not statistically independent, an alternate
1119 measurement which is statistically consistent with the default measurement should not be
1120 used in calculating a systematic uncertainty. The difference between the two measurements
1121 is $\Delta = y_c - y_i$. The difference in quadrature of the uncertainties is calculated by Eq. 9. It
1122 could be possible to check if $\Delta < \sigma$ and exclude such cases from the systematic uncertainties.
1123 However, there can be statistical fluctuations for which $\Delta > \sigma$. If the variations between the
1124 default and alternate measurements are purely statistical, the distribution of Δ/σ should
1125 be a Gaussian with a mean value that is consistent with zero and a deviation σ consistent
1126 with unity. In this analysis, if the mean value is less than 0.1 and σ is less than 1, the
1127 variation passes the consistency check.

1128 Only the measurements which passed the Barlow check ($n_i > 1$) are used to determine
1129 the systematic uncertainty. For measurements $N > 2$, the systematic uncertainty has been
1130 determined as the RMS (eqn. 10) of the available measurements. If $N=2$, the absolute
1131 difference is assigned as systematic uncertainty.

$$\delta y_{syst.} = \sqrt{\frac{1}{N} \sum_i (y_i - \bar{y})^2} \quad (10)$$

1132 Here N is the total number of available measurements including y_c and \bar{y} is the average
1133 of value of the measurements. The measurement did not pass Barlow check, zero systematic
1134 uncertainty has been assigned to the value.

1135 By suing the way as explained above, all the main contributions to the systematic un-
1136 certainty of particle spectra have been studied. In particular those that comes from signal
1137 extraction, topological and kinematical selection cuts, track quality selection and $n\sigma$ TPC
1138 PID variation. the meaning of each source of systematic uncertainty studied is described
1139 in the following:

1140

1141 **Signal extraction**

1142 We have extracted the signal with varying the yield calculating method which contains
1143 the method of signal extraction by integrating the Voigtian fit function and bin counting.
1144 We also have varied the normalisation range which is related to the invariant mass region
1145 where the mixed events distribution is scaled to subtract the combinatorial background
1146 and different background estimator such as Like-Sign distribution and polynomial fit was
1147 taken account into the systematic source of signal extraction. The systematic uncertainty
1148 from signal extraction is sum in quadrature of three sources.

1149

1150 **Topological selection**

1151 To evaluate the stability of the chosen set of values for the topological cuts, loose and tight
1152 cuts have beed defined in order to vary by $\pm 10\%$ respectively. The parameters are changed
1153 once at a time. Total systematic uncertainty from topological selection is calculated by
1154 summation in quadrature of nine sources.

1155

1156 **TPC $N_{cluster}$ selection**

1157 The selection performed for the daughter tracks of the cascade is that $N_{cluster}$ is larger
1158 than 70 and the value has been varied to 60 and 80 in order to estimate the systematic
1159 uncertainty due to this selection.

1160

1161 **TPC dE/dx selection**

1162 In order to evaluate any potential effect due to the TPC dE/dx selection (U_{PID}), the N_σ
1163 selection was varied with $N = 2.5$ and 3.5 .

1164

1165 **p_T shape correction**

1166 As described in Section 5.2, due to the different shape of the measured and generated
1167 $\Xi(1530)^0$ spectra, we have applied reweighing procedure to the generated spectra to have
1168 same shape and this correction is added into contributor of systematic uncertainty as
1169 p_T shape correction.

1170

1171 **Mass window range selection**

1172 In order to select Ξ^\pm which is daughter particle of $\Xi(1530)^0$, we apply the mass window

1173 ± 7 MeV/ c^2 around $\Xi(1530)^0$ mass on $\Lambda\pi$ invariant mass distribution. The boundaries
1174 has been varied to ± 6 MeV/ c^2 and ± 8 MeV/ c^2 to estimate systematic uncertainty.

1175

1176 **Vertex range selection**

1177 The distribution of vertex-z is shown in Fig.20. The cut on $|Vz|$ was varied from the nominal
1178 ± 10 cm to ± 9 cm, ± 11 cm.

1179

1180 **Material Budget and hadronic cross section**

1181 A possible source of uncertainty comes from the description of the material, active (detecting area)
1182 or dead (structure and cable), that the particles cross during their travel in
1183 the MC with respect to the real material present in the detector. Such description could
1184 affect the reconstruction efficiency in different aspects (e.g. multiple scattering, energy
1185 loss). The value estimated by Ξ analysis [42] has been used in this study which gives 4%
1186 systematic uncertainty. In case of systematic uncertainty from hadronic cross section, we
1187 have inherited the value studied in previous measurement[43] which amount is 1%.

1188

1189 **Tracking efficiency**

1190 Systematic uncertainties from tracking efficiency from ITS + TPC combined track were
1191 assigned as 3% in p–Pb and 4% in Pb–Pb collision system.[43]
1192 (<https://twiki.cern.ch/twiki/bin/view/ALICE/TrackingEfficiencyCharged>)

1193

1194 Finally, total systematic uncertainty is sum in quadrature of sources listed above. Figure
1195 45 and Figure 46 show the total systematic uncertainty in minimum bias event and
1196 different multiplicity classes in p–Pb collisions, respectively. Again, Figure 47 and Figure
1197 48 present the total systematic uncertainty in minimum bias event and different centrality
1198 classes in Pb–Pb collisions.

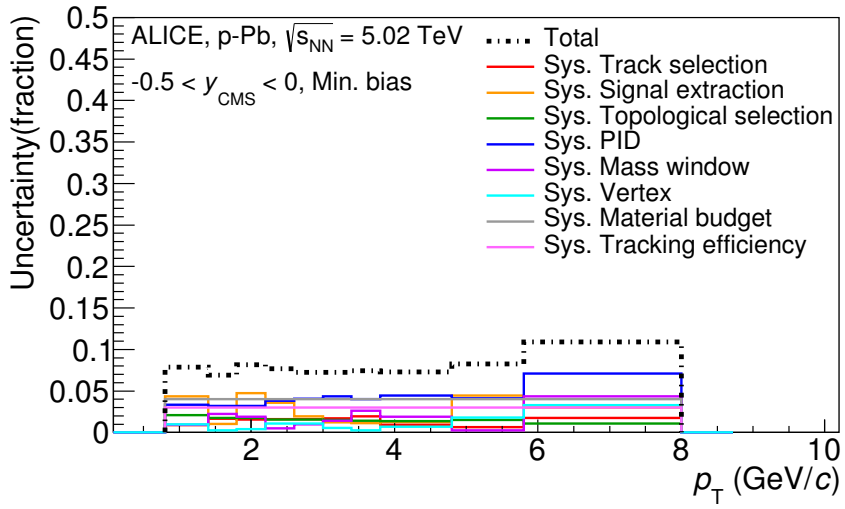


Figure 45: Summary of the contributions to the systematic uncertainty in minimum bias events in p–Pb collisions. The dashed black line is the sum in quadrature of all the contributions.

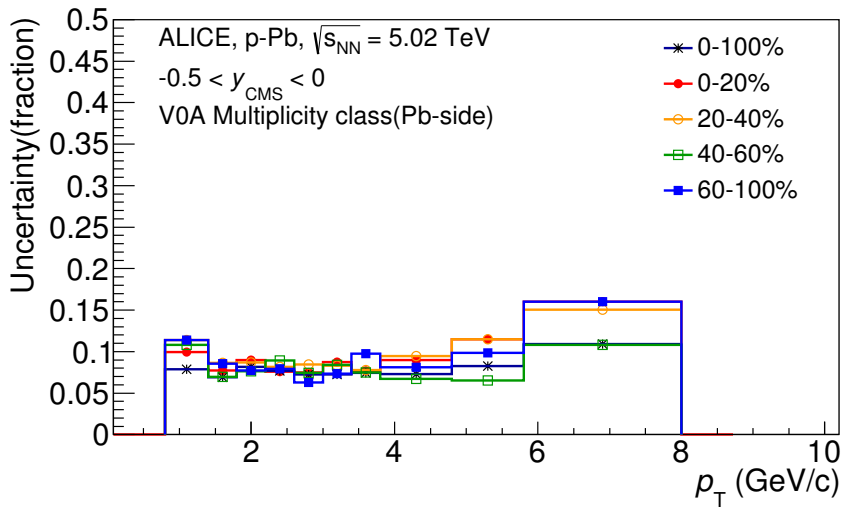


Figure 46: Systematic uncertainties for each multiplicity classes in p–Pb collisions.

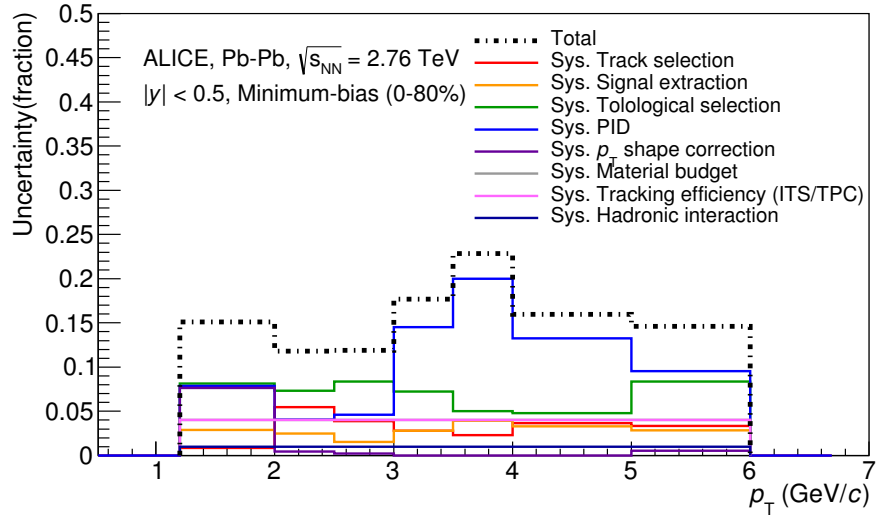


Figure 47: Summary of the contributions to the systematic uncertainty in minimum bias events in Pb–Pb collisions. The dashed black line is the sum in quadrature of all the contributions.

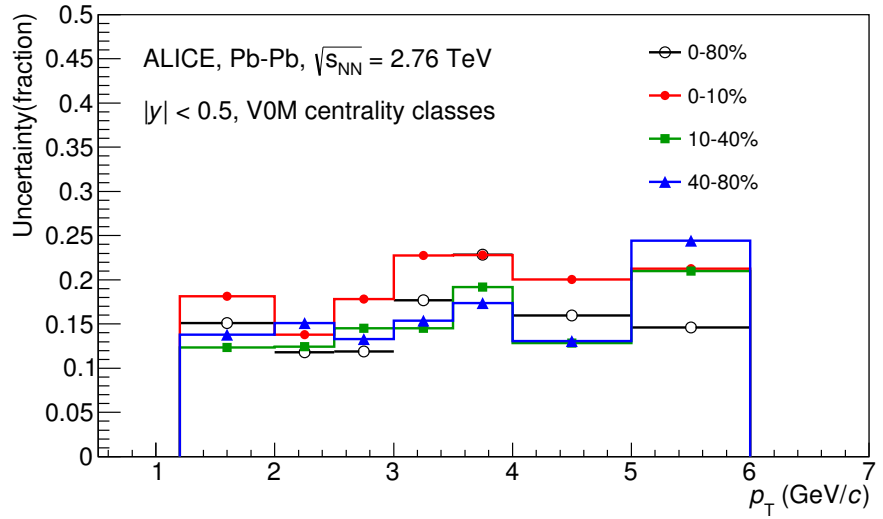


Figure 48: Systematic uncertainties for each multiplicity classes.

Source of uncertainty	p-Pb	Pb-Pb
<i>p</i> _T -dependent		
Tracking efficiency	3%	4%
Tracks selection	1-2%	1-5%
Topological selection	1-2%	5-8%
PID	3-7%	4-20%
Signal extraction	1-5%	1-4%
<i>p</i> _T shape correction	-	0-8%
Mass window (Ξ^\pm)	4%	-
Vertex selection	3%	-
<i>p</i> _T -independent		
Hadronic interaction	-	1%
Material budget	4%	4%
Branching ratio	0.3%	0.3%
Total	8-12%	9-25 %

Table 9: Summary of the systematic uncertainties on the differential yield, $d^2N/(dp_T dy)$. Minimum and maximum values in all p_T intervals and multiplicity classes in p–Pb, centrality classes in Pb–Pb are shown for each source.

₁₁₉₉ **5.5 $\Xi(1530)^0$ transverse momentum spectra**

₁₂₀₀ The raw yield shown in Figure 43 and 44 have been corrected for efficiency as described
₁₂₀₁ in section 5.2. The measured spectra for $(\Xi(1530)^0 + \bar{\Xi}(1530)^0)/2$ are reported in Figure
₁₂₀₂ 49 for p–Pb collisions and Figure 50 for Pb–Pb collisions. The statistical and systematic
₁₂₀₃ uncertainties are reported respectively as the error bars and the boxes on the plot. The
₁₂₀₄ corrected yields for p–Pb collisions are measured with $0.8 < p_T < 8.0$ GeV/c while the
₁₂₀₅ yields for Pb–Pb collisions are obtained with $1.2 < p_T < 6.0$ GeV/c due to difficulty of
₁₂₀₆ signal extraction in low and high p_T region.

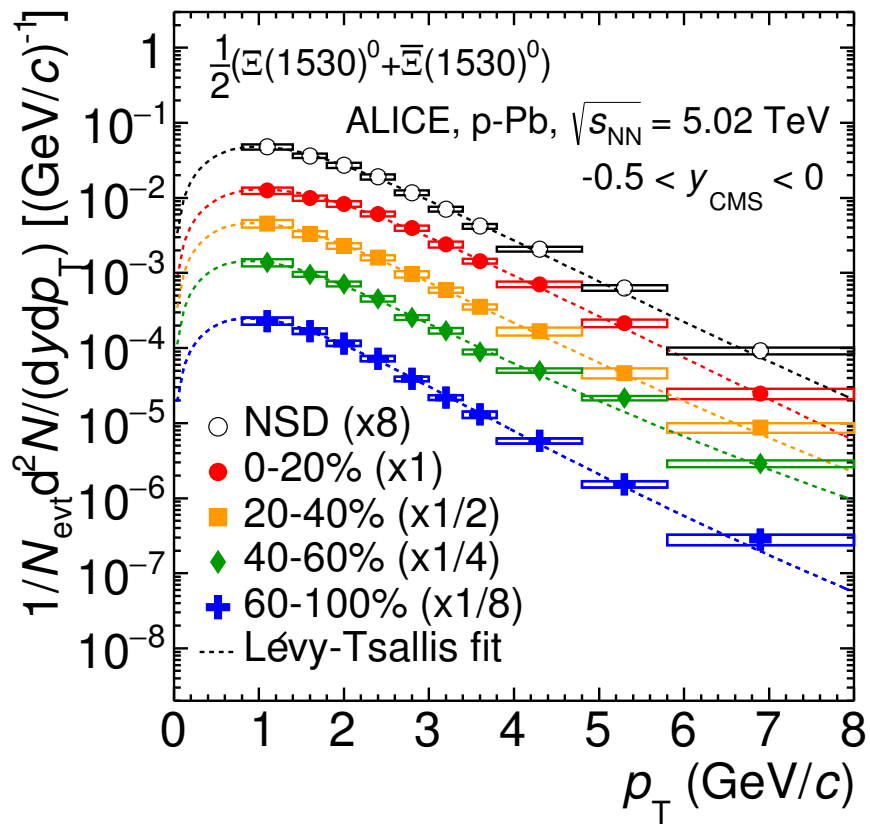


Figure 49: Corrected yields as function of p_T in NSD events and multiplicity dependent event classes in p-Pb collision system. Statistical uncertainties are presented as bar and systematical uncertainties are plotted as boxes.

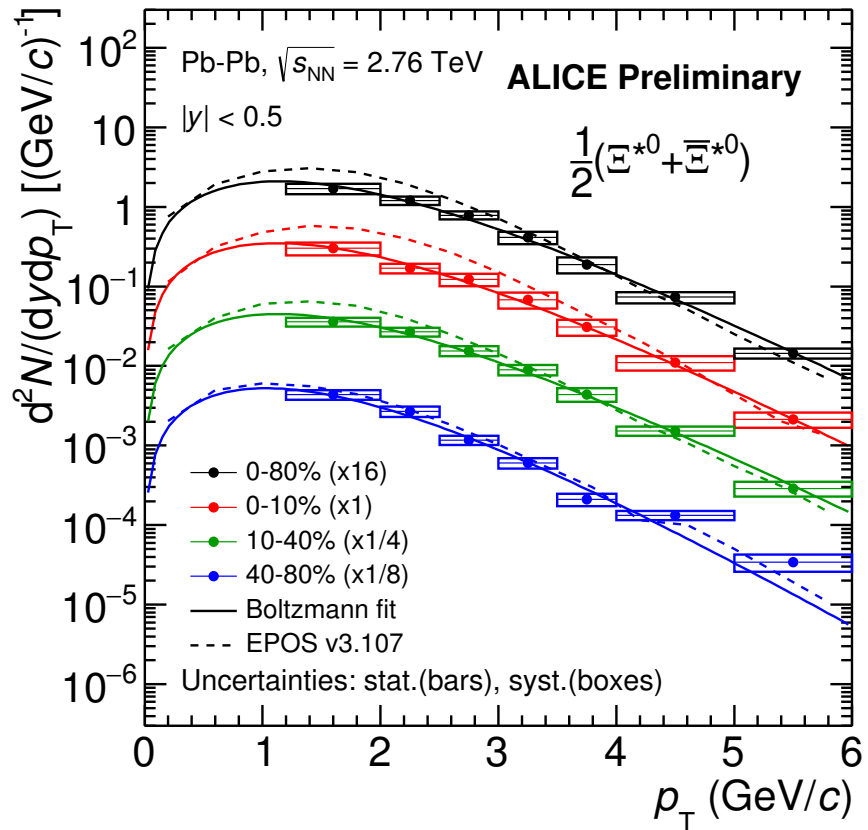


Figure 50: Corrected yields as function of p_T in different centrality classes in Pb-Pb collision system. Statistical uncertainties are presented as bar and systematical uncertainties are plotted as boxes.

1207 6 Further results and discussion

1208 The transverse momentum distributions of double-strange hyperon resonances, $\Xi(1530)^0$
1209 , produced in p–Pb collisions at $\sqrt{s_{\text{NN}}}= 5.02$ TeV and Pb–Pb collisions at $\sqrt{s_{\text{NN}}}= 2.76$
1210 TeV were measured in the mid-rapidity range and they have been already presented in
1211 Chapter 5. From the measurement, the $\langle p_{\text{T}} \rangle$ and integrated particle yield ratios with
1212 system size have been obtained. In the present Chapter these results are compared with
1213 model predictions and discussed in connection with the following topics:

- 1214 • Mean transverse momentum studies
- 1215 • Study of particle production mechanism in hadronic phase
- 1216 • Study of strangeness enhancement

1217 Most of the theoretical aspects related to these topics and, in particular, the description
1218 of the models already have been addressed in Chapter 2.

1219 6.1 Mean transverse momentum

1220 Figure 51 shows the mean transverse momentum $\langle p_{\text{T}} \rangle$ as a function of mean charged-
1221 particle multiplicity density $\langle dN_{\text{ch}}/d\eta_{\text{lab}} \rangle$ at midrapidity. The results for $\Xi(1530)^0$ are
1222 compared with those for other hyperons observed in p–Pb collisions at $\sqrt{s_{\text{NN}}}= 5.02$ TeV [4,
1223 6].

1224 Increasing trends from low to high multiplicities are observed for all hyperons. The
1225 mean transverse momenta increase by 20% as the mean charged-particle multiplicity in-
1226 creases from 7.1 to 35.6. This result is similar to the one obtained for the other hyperons.
1227 Furthermore, a similar increase has been observed also for K^{\pm} , K_S^0 , $K^*(892)^0$ and ϕ [5],
1228 whereas protons are subject to a larger ($\sim 33\%$) increase in the given multiplicity range,
1229 as discussed also in Ref. [4].

1230 In all multiplicity classes, the $\langle p_{\text{T}} \rangle$ follows an approximate mass ordering:

- 1231 • $\langle p_{\text{T}} \rangle_{\Lambda} < \langle p_{\text{T}} \rangle_{\Xi^-} \simeq \langle p_{\text{T}} \rangle_{\Sigma^{*\pm}} < \langle p_{\text{T}} \rangle_{\Xi^{*0}} < \langle p_{\text{T}} \rangle_{\Omega^-}$

1232 The $\langle p_{\text{T}} \rangle$ of $\Sigma^{*\pm}$ looks systematically lower than the $\langle p_{\text{T}} \rangle$ of Ξ^- , despite the larger mass
1233 of $\Sigma^{*\pm}$. The uncertainties, however, are too large to draw any conclusion on possible hints
1234 of violation of the mass hierarchy. This hierarchy of mass-ordering, also including D^0 and
1235 J/ψ in the comparison, is displayed in Figure 52. Note, however, that the D^0 and J/ψ
1236 were measured in different rapidity ranges: $|y_{\text{CMS}}| < 0.5$ [8] ($|y_{\text{CMS}}| < 0.9$ [9]) for D^0 (J/ψ)
1237 in pp and $-0.96 < y_{\text{CMS}} < 0.04$ [8] ($-1.37 < y_{\text{CMS}} < 0.43$ [10]) for D^0 (J/ψ) in p–Pb, and
1238 the results for D^0 and J/ψ in p–Pb collisions are for the 0–100% multiplicity class. This
1239 mass dependence is observed in both p–Pb and pp collisions. It was observed also by the
1240 STAR collaboration [44] in MB pp, MB d–Au and central Au–Au collisions.

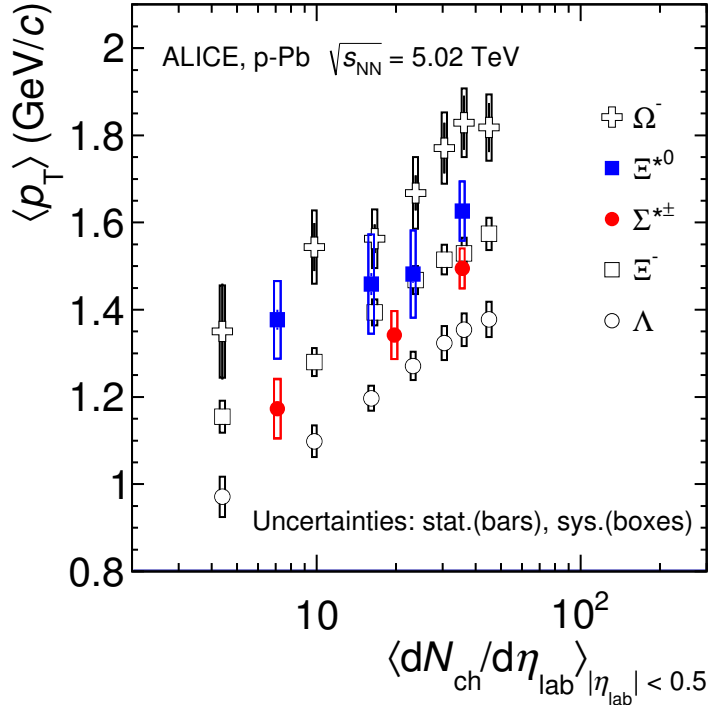


Figure 51: Mean transverse momenta $\langle p_T \rangle$ of Λ , Ξ^- , $\Sigma^{*\pm}$, Ξ^{*0} and Ω^- in p–Pb collisions at $\sqrt{s_{NN}}=5.02$ TeV as a function of mean charged-particle multiplicity density $\langle dN_{ch}/d\eta_{lab} \rangle$, measured in the pseudorapidity range $|\eta_{lab}| < 0.5$. The results for Λ , Ξ^- and Ω^- are taken from [4, 5, 6]. Statistical and systematic uncertainties are represented as bars and boxes, respectively. The Ω^- and Ξ^- points in the 3rd and 4th lowest multiplicity bins are slightly displaced along the abscissa to avoid superposition with the $\Xi(1530)^0$ points.

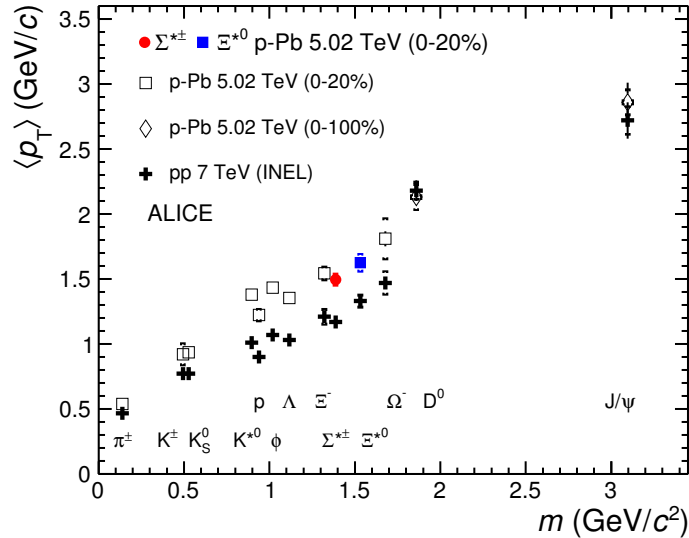


Figure 52: Mass dependence of the mean transverse momenta of identified particles for the 0 – 20% V0A multiplicity class and with $-0.5 < |y_{\text{CMS}}| < 0$ in p–Pb collisions at $\sqrt{s_{\text{NN}}} = 5.02$ TeV [4, 6], and in minimum-bias pp collisions at $\sqrt{s} = 7$ TeV [7] with $|y_{\text{CMS}}| < 0.5$. Additionally, D^0 and J/ψ results are plotted. The D^0 and J/ψ were measured in different rapidity ranges: $|y_{\text{CMS}}| < 0.5$ [8] ($|y_{\text{CMS}}| < 0.9$ [9]) for D^0 (J/ψ) in pp and $-0.96 < |y_{\text{CMS}}| < 0.04$ [8] ($-1.37 < |y_{\text{CMS}}| < 0.43$ [10]) for D^0 (J/ψ) in p–Pb. Note also that the results for D^0 and J/ψ in p–Pb collisions are for the 0–100% multiplicity class.

1241 Furthermore, for the light-flavour hadrons, the mean transverse momenta in p–Pb col-
1242 lisions are observed to be consistently higher than those in pp collisions at 7 TeV. The
1243 situation for the charm hadrons is different, where $\langle p_T \rangle$ appears compatible between both
1244 colliding systems. The discrepancy is likely due to different production mechanisms for
1245 heavy and light flavours and to a harder fragmentation of charm quarks. Specifically, the
1246 fact that $\langle p_T \rangle$ remains similar in pp and in p–Pb is consistent with an $R_{p\text{Pb}}$ ratio com-
1247 patible with unity at all p_T [8] for D^0 , and/or with the effects of shadowing in p–Pb which
1248 reduces the production at low p_T and thus increasing the overall $\langle p_T \rangle$ for J/ψ [10]; the
1249 small p_T hardening expected in pp when going from 5.02 to 7TeV is apparently not enough
1250 to counter-balance the situation.

1251 Because of small decrease of the $\langle p_T \rangle$ for proton and Λ relative to those for K^{*0} and
1252 ϕ , two different trends for mesons and baryons have been suggested [45]. Even including
1253 D^0 and J/ψ , as shown in Figure 52, a different trend for mesons and baryons cannot be
1254 convincingly established.

1255 **6.2 Particle yield ratios**

1256 **6.2.1 Integrated yield ratios of excited to ground-state hadrons**

1257 The integrated yield ratios of excited to ground-state hyperons [46, 4, 7, 6] with the same
1258 strangeness content, for different collision systems and energies, are shown in Figure 53
1259 as a function of system size. The ratio of $\Xi(1530)^0$ to Ξ is flat across the system and
1260 it complements the information derived from other resonance measurement for different
1261 lifetime which are shown in Figure 54.

1262 The short-lived resonances(ρ , K^* and Λ^*) which exhibit suppression from peripheral to
1263 central lead-lead collisions and with respect to thermal model in central lead-lead collisions.
1264 Currently favored explanation of is dominance of elastic re-scattering of decay daughters
1265 over regeneration in the hadronic phase.

1266 The constant behavior of the yield ratios of excited to ground-state hyperons with same
1267 strangeness content ($\Xi(1530)^0$ and Φ) indicates that neither regeneration nor re-scattering
1268 dominates with increasing collision system size because of its longer-lifetime.

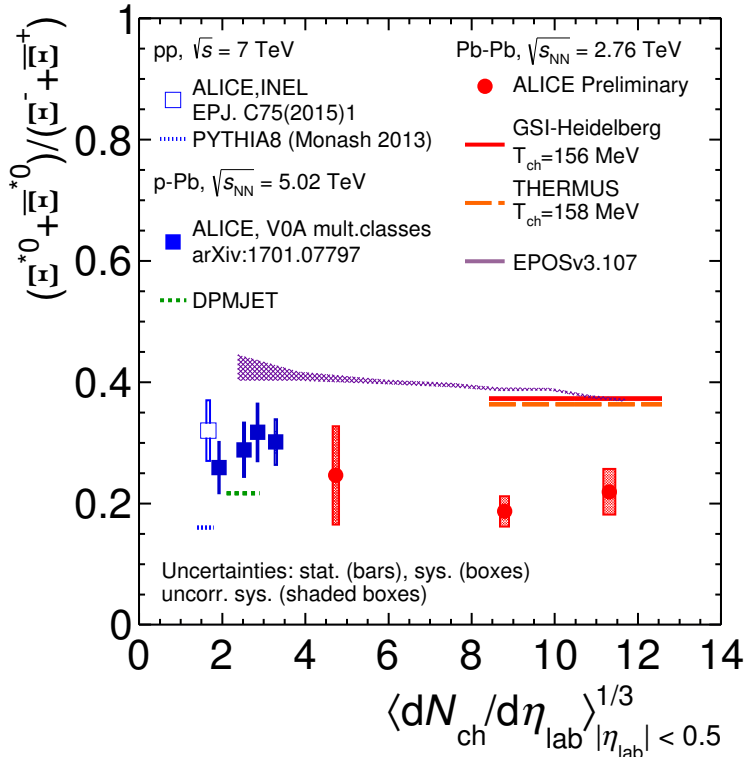


Figure 53: Ratio of $\Xi(1530)^0$ to Ξ^- measured in pp [7], p–Pb [4, 6] and Pb–Pb collisions as a function of $\langle dN_{ch}/d\eta_{lab} \rangle$ measured at midrapidity. Statistical uncertainties (bars) are shown as well as total systematic uncertainties (hollow boxes) and systematic uncertainties uncorrelated across multiplicity (shaded boxes). A few model predictions are also shown as lines at their appropriate abscissa.

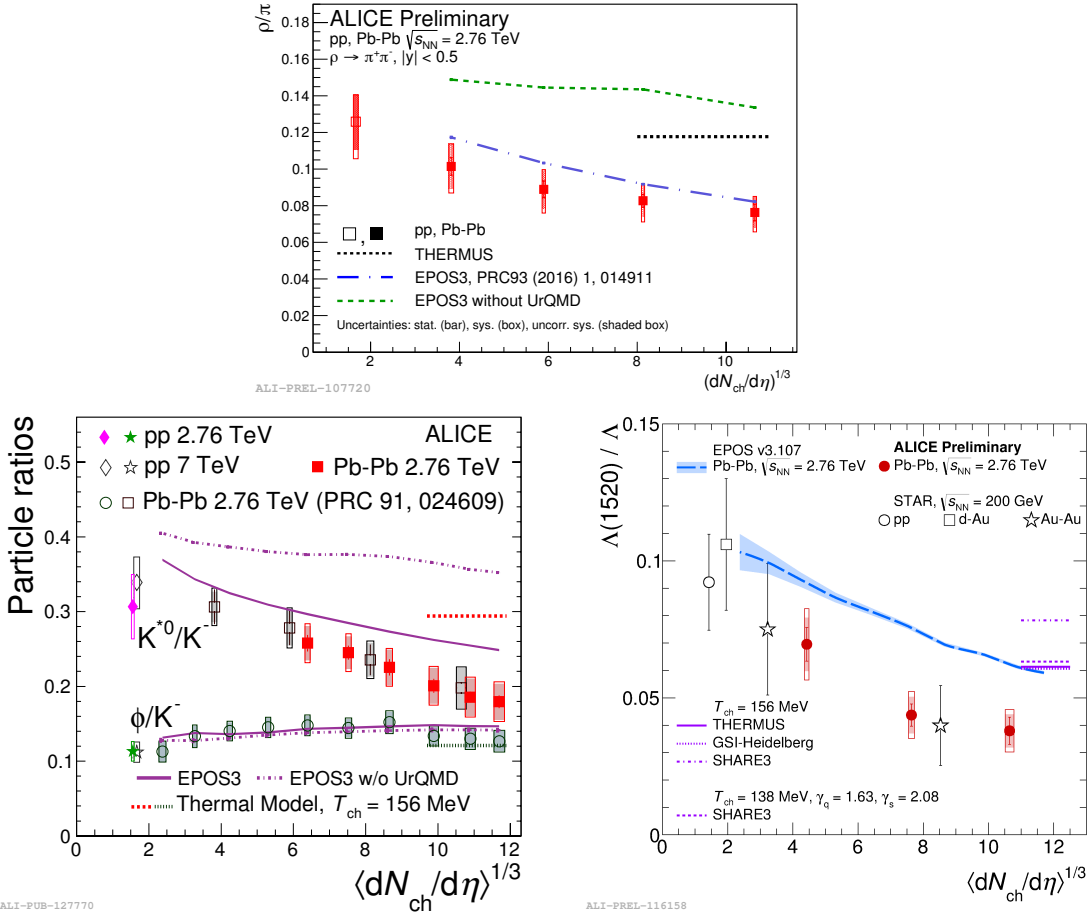


Figure 54: Ratio of ρ/π (Up), K^*/K , ϕ/K (Left bottom) and Λ^*/Λ with system size measured at mid-rapidity. Statistical uncertainties (bars) are shown as well as total systematic uncertainties (hollow boxes) and systematic uncertainties uncorrelated across multiplicity (shaded boxes). A few model predictions are also shown as lines at their appropriate abscissa.

1269 **6.3 Integrated yield ratios to pion**

1270 The integrated yield ratios of excited hyperons to pions are shown in Figure 55 to study
1271 the evolution of relative strangeness production yields with increasing collision system
1272 size. The ratio of $\Xi(1530)^0$ to Ξ is observed to be increase from pp to p–Pb collisions
1273 system and then, decrease from peripheral to central Pb–Pb collision. The QCD-inspired
1274 predictions like PYTHIA for pp [47] and DPMJET for p–Pb [39] clearly underestimate
1275 the observed yield ratios, while the statistical one seems to be comparable with results
1276 from high multiplicity in p–Pb but the ratio in Pb–Pb is below with respect to the model.
1277 The results in pp and p–Pb collisions are consistent with previous observation of ground-
1278 state hyperons to pion ratios. The Figure 56 presents particle yield ratios to pions of
1279 strange and multi-strange hadrons normalized to the values measured in pp collisions. As
1280 shown in the Figure 56, the $\Xi(1530)^0$ to pion ratios follow the trend of $\Xi \pi$ as function of
1281 $\langle dN_{ch}/d\eta_{lab} \rangle$ and indicate that the strangeness enhancement observed in p–Pb collisions
1282 depends predominantly on the strangeness content, rather than on the hyperon mass.

1283 The Figure 57 also shows the hyperon-to-pion ratios and compared with model predic-
1284 tions. The

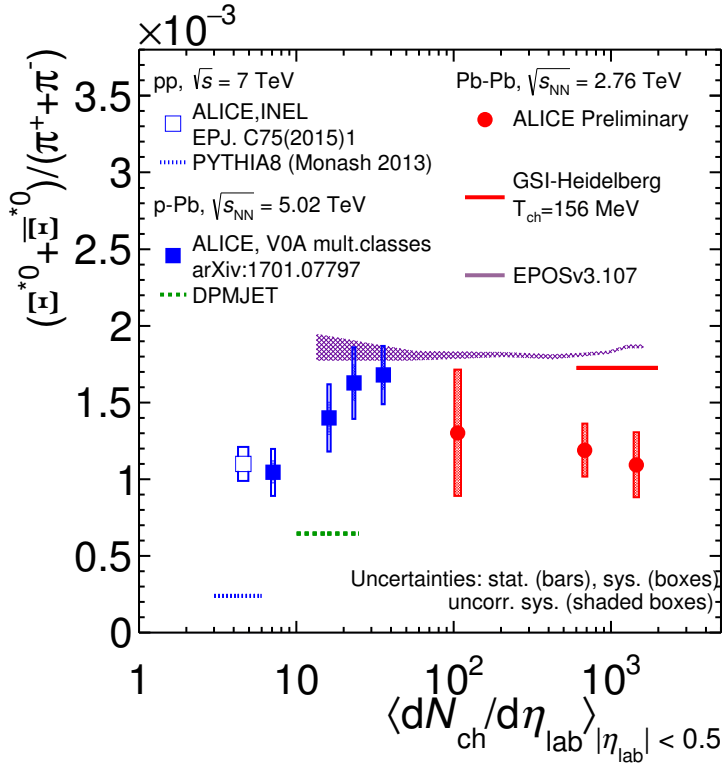


Figure 55: Ratio of $\Xi(1530)^0$ to π^\pm , measured in pp [11] and p–Pb [7] collisions, as a function of the average charged particle density ($\langle dN_{ch}/d\eta_{lab} \rangle$) measured at mid-rapidity. Statistical uncertainties (bars) are shown as well as total systematic uncertainties (hollow boxes) and systematic uncertainties uncorrelated across multiplicity (shaded boxes). A few model predictions are also shown as lines at their appropriate abscissa.

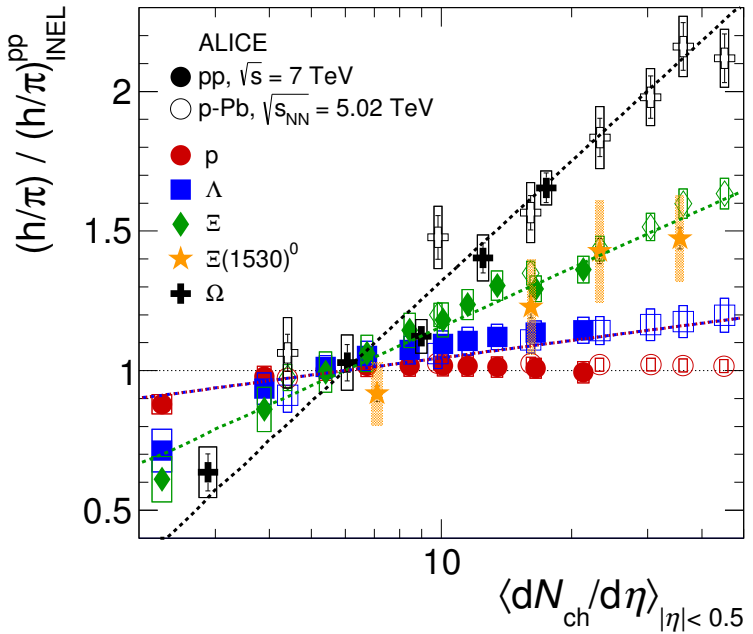


Figure 56: Particle yield ratios to pions of strange and multi-strange hadrons normalized to the values measured in pp collisions, both in pp and in p–Pb collisions. The common systematic uncertainties cancel in the double-ratio. The empty boxes represent the remaining uncorrelated uncertainties. The lines represent a simultaneous fit of the results with the empirical scaling formula in Equation ??.

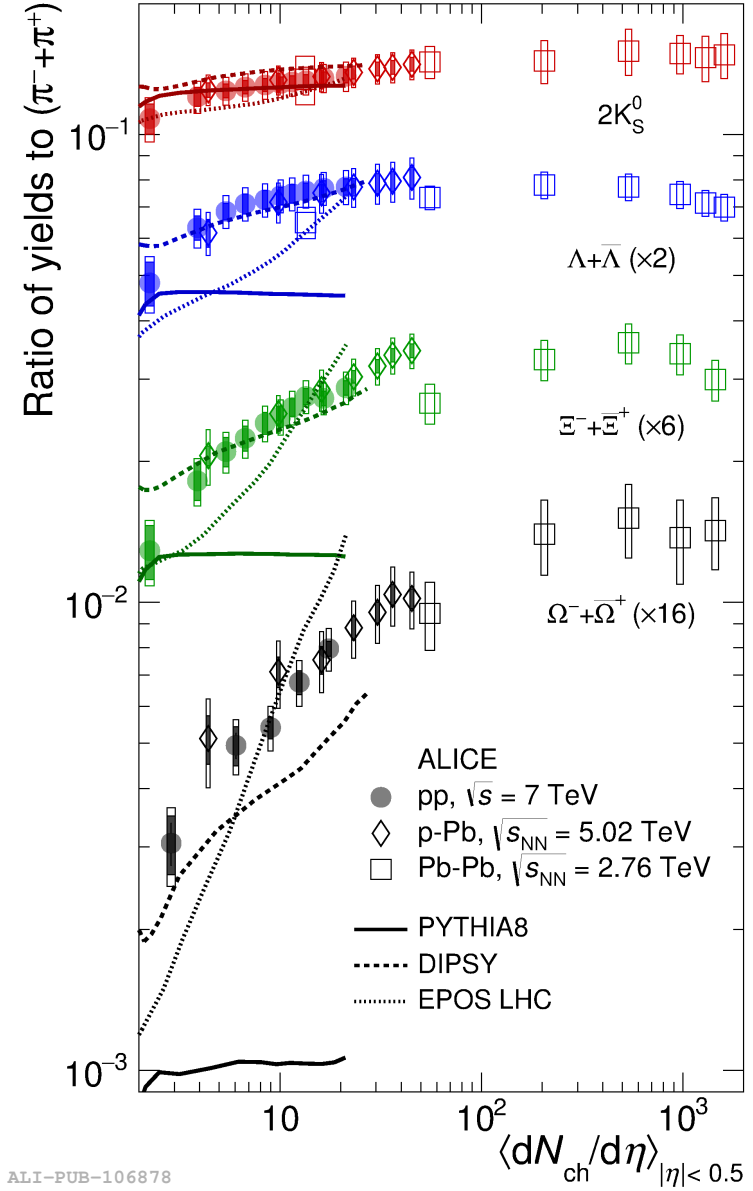


Figure 57: p_T -integrated yield ratios of strange and multi-strange hadrons to $(\pi^+ + \pi^-)$ as a function of $\langle dN_{ch}/d\eta_{lab} \rangle$ measured in the rapidity interval $|\eta| < 0.5$. The empty and dark-shaded boxes show the total systematic uncertainty and the contribution uncorrelated across multiplicity bins, respectively. The values are compared to calculations from MC models and to results obtained in Pb–Pb and p–Pb collisions at the LHC.

1285 **References**

- 1286 [1] **Particle Data Group** Collaboration, K. Olive *et al.*, “Review of Particle Physics,”
1287 *Chin. Phys. C* **38** (2014) 090001.
- 1288 [2]
- 1289 [3] **ALICE** Collaboration, K. e. a. Aamodt, “Alignment of the ALICE Inner Tracking
1290 System with cosmic-ray tracks,” *JINST* **5** (2010) P03003.
- 1291 [4] **ALICE** Collaboration, J. Adam *et al.*, “Multiplicity dependence of pion, kaon,
1292 proton and lambda production in p–Pb collisions at $\sqrt{s_{NN}} = 5.02$ TeV,” *Phys. Lett.*
1293 **B728** (2014) 25–38, [arXiv:1307.6796 \[nucl-ex\]](#).
- 1294 [5] **ALICE** Collaboration, J. Adam *et al.*, “Production of $K^*(892)^0$ and $\phi(1020)$ in
1295 p–Pb collisions at $\sqrt{s_{NN}} = 5.02$ TeV,” *Eur. Phys. J.* **C76** (2016) 245,
1296 [arXiv:1601.7868 \[nucl-ex\]](#).
- 1297 [6] **ALICE** Collaboration, J. Adam *et al.*, “Multi-strange baryon production in p–Pb
1298 collisions at $\sqrt{s_{NN}} = 5.02$ TeV,” *Phys. Lett.* **B758** (2016) 389–401,
1299 [arXiv:1512.07227 \[nucl-ex\]](#).
- 1300 [7] **ALICE** Collaboration, B. Abelev *et al.*, “Production of $\Sigma(1385)^{\pm}$ and $\Xi(1530)^0$ in
1301 proton-proton collisions at $\sqrt{s} = 7$ TeV,” *Eur. Phys. J.* **C75** (2015) 1,
1302 [arXiv:1406.3206 \[nucl-ex\]](#).
- 1303 [8] **ALICE** Collaboration, J. Adam *et al.*, “ D -meson production in p–Pb collisions at
1304 $\sqrt{s_{NN}} = 5.02$ TeV and in pp collisions at $\sqrt{s} = 7$ TeV,” *Phys. Rev. C* **94** (2016)
1305 054908, [arXiv:1605.07569 \[nucl-ex\]](#).
- 1306 [9] **ALICE** Collaboration, B. Abelev *et al.*, “Inclusive J/ψ production in pp collisions
1307 at $\sqrt{s} = 2.76$ TeV,” *Phys. Lett.* **B718** (2012) 295–306, [arXiv:1203.3641 \[hep-ex\]](#).
- 1308 [10] **ALICE** Collaboration, J. Adam *et al.*, “Rapidity and transverse-momentum
1309 dependence of the inclusive J/ψ nuclear modification factor in p–Pb collisions at
1310 $\sqrt{s_{NN}} = 5.02$ TeV,” *JHEP* **06** (2015) 55, [arXiv:1503.07179 \[nucl-ex\]](#).
- 1311 [11] **ALICE** Collaboration, J. Adam *et al.*, “Measurement of pion, kaon and proton
1312 production in proton-proton collisions at $\sqrt{s} = 7$ TeV,” *Eur. Phys. J.* **C75** (2015)
1313 226, [arXiv:1504.00024 \[nucl-ex\]](#).
- 1314 [12] F. Halzen and A. Martin.
- 1315 [13] M. Gell-Mann and Y. Ne’eman.
- 1316 [14] J. Rafelski and B. Mller.

- 1317 [15] S. Wheaton, J. Cleymans, and M. Hauer, “THERMUS: A Thermal model package
 1318 for ROOT,” *Comput. Phys. Commun.* **180** (2009) 84–106, [hep-ph/0407174](#).
- 1319 [16] J. Cleymans, S. Kabana, I. Kraus, H. Oeschler, K. Redlich, and N. Sharma,
 1320 “Antimatter production in proton-proton and heavy-ion collisions at ultrarelativistic
 1321 energies,” *Phys. Rev.* **C84** (2011) 054916, [arXiv:1105.3719 \[hep-ph\]](#).
- 1322 [17] L. Evans and P. Bryant.
- 1323 [18]
- 1324 [19]
- 1325 [20]
- 1326 [21]
- 1327 [22]
- 1328 [23]
- 1329 [24] **ALICE** Collaboration, K. Aamodt *et al.*, “The ALICE experiment at the CERN
 1330 LHC,” *JINST* **3** (2008) S08002.
- 1331 [25] **ALICE** Collaboration, L. B. et al, “Definition of the ALICE coordinate system and
 1332 basic rules for sub-detector components numbering,” *In Internal Note
 1333 ALICE-INT-2003-038* .
- 1334 [26] **ALICE** Collaboration, J. e. a. Alme, “The ALICE TPC, a large 3-dimensional
 1335 tracking device with fast readout for ultra-high multiplicity events,” *In Nuclear
 1336 Instruments and Method in Physics Research* **A622** (2010) 316–367.
- 1337 [27]
- 1338 [28] R. Glauber.
- 1339 [29] A. S. K.C. Chung, C.S. Whang and G. Pech.
- 1340 [30] **ALICE** Collaboration, J. Adam *et al.*, “Centrality dependence of particle
 1341 production in p–Pb collisions at $\sqrt{s_{\text{NN}}} = 5.02 \text{ TeV}$,” *Phys. Rev.* **C91** (2015) 064905,
 1342 [arXiv:1412.6828 \[nucl-ex\]](#).
- 1343 [31] **ALICE** Collaboration, B. Abelev *et al.*, “Centrality determination of Pb–Pb
 1344 collisions at $\sqrt{s_{\text{NN}}} = 2.76 \text{ TeV}$ with ALICE,” *Phys. Rev.* **C88** (2013) ,
 1345 [arXiv:1303.0737 \[nucl-ex\]](#).
- 1346 [32]

- 1347 [33]
- 1348 [34] e. a. Bagnasco. S.
- 1349 [35] R. Brun and F. Rademakers.
- 1350 [36] **ALICE** Collaboration, B. Abelev *et al.*, “Performance of the ALICE Experiment at
1351 the CERN LHC,” *Int. J. Mod. Phys. A***29** (2014) 1430044, [arXiv:1402.4476](#)
1352 [nucl-ex].
- 1353 [37] **ALICE** Collaboration, B. Abelev *et al.*, “Pseudorapidity Density of Charged
1354 Particles in p–Pb Collisions at $\sqrt{s_{\text{NN}}}= 5.02$ TeV,” *Phys. Rev. Lett.* **110** (2013)
1355 032301, [arXiv:1210.3615](#) [nucl-ex].
- 1356 [38] **ALICE** Collaboration, K. Aamodt *et al.*, “Strange particle production in
1357 proton-proton collisions at $\sqrt{s}= 0.9$ TeV with ALICE at the LHC,” *Eur. Phys. J.*
1358 **C71** (2011) 1594, [arXiv:1012.3257](#) [nucl-ex].
- 1359 [39] S. Roesler, R. Engel, , and J. Ranft, “The Monte Carlo Event Generator
1360 DPMJET-III, Advanced Monte Carlo for Radiation Physics, Particle Transport
1361 Simulation and Applications,” *Conference Proceedings, MC2000, Lisbon, Portugal,*
1362 *October 23-26* (2000) 1033–1038, [hep-ph/0012252](#).
- 1363 [40] R. Brun, F. Carminati, and S. Giani, “GEANT detector description and simulation
1364 tool,” *CERN-W5013* (1994) .
- 1365 [41] R. Barlow, “Systematic Errors: Facts and Fictions,” *Presented at Advanced*
1366 *Statistical Techniques in HEP, Durham, March 2002* (2002) 333p,
1367 [hep-ex/0207026v1](#).
- 1368 [42] **ALICE** Collaboration, B. Abelev *et al.*, “Multi-strange baryon production at
1369 mid-rapidity in Pb–Pb collisions at $\sqrt{s_{\text{NN}}}= 2.76$ TeV,” *Phys. Lett. B***728** (2014)
1370 216–227, [arXiv:1307.5543](#) [nucl-ex].
- 1371 [43] **ALICE** Collaboration, B. Abelev *et al.*, “Centrality dependence of π , K and p
1372 production in Pb–Pb collisions at $\sqrt{s_{\text{NN}}}= 2.76$ TeV,” *Phys. Rev. C***88** (2013) ,
1373 [arXiv:1301.4361](#) [nucl-ex].
- 1374 [44] **STAR** Collaboration, B. I. Abelev *et al.*, “Hadronic resonance production in d–Au
1375 collisions at $\sqrt{s_{\text{NN}}}= 200$ GeV measured at the BNL Relativistic Heavy-Ion Collider,”
1376 *Phys. Rev. C***78** (2008) 044906, [arXiv:0801.0450](#) [nucl-ex].
- 1377 [45] A. Velásquez, “Mean p_{T} scaling with m/n_q at the LHC: Absence of (hydro) flow in
1378 small systems?,” *Nucl. Phys. A***943** (2015) 9–17, [arXiv:1506.00584](#) [hep-ph].

- 1379 [46] **ALICE** Collaboration, B. Abelev *et al.*, “Multi-strange baryon production in pp
1380 collisions at $\sqrt{s} = 7$ TeV with ALICE,” *Phys. Lett.* **B712** (2012) 309,
1381 arXiv:1204.0282 [nucl-ex].
- 1382 [47] T. Sjöstrand, S. Mrenna, and P. Skands, “A brief introduction to PYTHIA 8.1,”
1383 *Comput. Phys. Comm.* **178** (2008) 852–867, arXiv:0710.3820 [hep-ph].

1384 **Acknowledgements**